A study of energy-energy correlations in charged tracks from hadronic decays of the Z^o at $\sqrt{s} = 91.2$ GeV

Owen Boyle

Department of Physics and Astronomy
The University of Glasgow
Glasgow, Scotland

Thesis submitted for the degree of Doctor of Philosophy

September 1991

Abstract

The energy-energy correlations in charged tracks from hadronic decays of the Z^o were studied at energies around the Z^o-pole of 91.2 GeV. From a comparison with $\mathcal{O}(\alpha_s^2)$ analytical formulae, the strong coupling constant, α_s, was measured. The results obtained were

$$\text{From the } EEC(\chi): \quad \alpha_s(M_z^2) = 0.132 \pm 0.006 \, ^{+0.012}_{-0.009}$$

$$\text{From the } AEEC(\chi): \quad \alpha_s(M_z^2) = 0.109 \pm 0.007 \, ^{+0.011}_{-0.007}$$

where the first error is experimental and the second is due to scale uncertainty.

The $EEC(\chi)$ was also studied for particle clusters and compared with a parton-level Monte Carlo simulation using an exact $\mathcal{O}(\alpha_s^2)$ matrix element formula. From this study the value of α_s obtained was

$$\text{From clustered } EEC(\chi): \ \alpha_s(M_z^2) = 0.111 \, ^{+0.016}_{-0.013}$$

An observation of the effects of coherence in b-quark fragmentation was made, leading to evidence in support of the principle of Local Parton-Hadron Duality.

An attempt was made to discriminate between samples of quark and gluon jets using the $EEC(\chi)$ function. No clear conclusion was reached due to limited statistics and the energy mismatch between quark jets and gluon jets.

Preface

This thesis describes a study of energy-energy correlations in charged tracks from hadronic decays of the Z^o at energies around the Z^o-pole of 91.2 GeV. Data were collected by the ALEPH detector, an experiment on the LEP e^+e^- collider at CERN. Data studied in this work represent all hadronic events collected during 1989 and 1990 and amount to approximately 186,000 events. The purpose of this work was to determine the strong coupling constant, α_s, at this energy and to investigate some aspects of the fragmentation process, in particular LPHD and differences between quark and gluon fragmentation.

The author's contribution to the experiment was to assist in the installation and maintenance of the laser calibration system in the TPC and to take part in detector performance monitoring during routine shifts.

The analysis presented herein is entirely the work of the author.

No portion of the work referred to in this thesis has been submitted in support of an application for another degree or qualification in this, or any other, institution of learning.

Acknowledgements

I am delighted to take this opportunity to acknowledge the help and support from many quarters which made it possible for me to carry out this work.

The munificence of the Science and Engineering Research Council and the hospitality of the Department of Physics and Astronomy was received gratefully. My thanks go to Professors Ferrier and Saxon and to all administrative staff in the Department for this.

Professor Skillicorn, Mike Scarr, Ian Knowles and Glen Cowan are thanked warmly for their patient explanation of theoretical matters. The help of Stan Thompson and Andy Halley in coping with my initiation into mainframe computing and detector maintenance was also greatly appreciated.

During my spell at CERN, the staff at the SERC office were instrumental in helping me settle in physically, while Ingrid ten Have gave me all the support I needed in adapting to the new working environment. I would also like to thank my numerous colleagues on the ALEPH collaboration, none of whom were ever reluctant to help a new student.

In Glasgow, without the excellent computing facilities supported by Alan Flavell, Dave Martin and staff this analysis would not have been possible. My supervisor, Ken Smith, has been a pillar of support at all times throughout this work and has provided me with stimulating discussion, enlightened direction and pertinent advice in addition to proof-reading repeatedly my various reports and, in particular, this thesis. My thanks are extended also to Ian Knowles and to Ingrid ten Have in this regard.

It was a pleasure to have worked in the company of Butrus Altoon, Simon Lumsdon and John Hearns who, in addition to all of those previously mentioned, unreservedly extended their friendship to me during my stay in Glasgow. I am delighted to thank Antigone Kamberou for providing me unstintingly with understanding, encouragement and moral support and to my parents for patiently supporting my studenthood the second time around.

To Christine

Contents

Chapter 1

The Collider and Detector.

1.1 Introduction.

This chapter describes the experimental apparatus used to collect the data which are studied in this thesis. The main part of this chapter, therefore, concerns the detector, ALEPH. All elements of this detector (the sub-detectors) are discussed in detail, with special emphasis given to those elements which were particularly important in this analysis (namely the TPC and the ITC). In addition, sub-detector elements which were not actually operational or installed during data-taking are briefly described. In order to give an insight into the functioning of the detector, a summary of particle interaction theory and detector techniques is also given. Note that the many items of information presented in this chapter were obtained from only a few sources. For brevity they are cited here only [1, 2, 3, 4].

1.1.1 Interactions of particles.

Before discussing the nature and functioning of the various sub-detector elements of a large and complex system such as ALEPH, it is useful to review the mechanisms by which high-energy particles interact with matter. Although different particles interact in different ways, it is possible to group particles according to the manner in which they interact;

- **Photons.** At energy scales significantly above the rest mass of the electron (0.5 MeV), the cross-sections for the the photo-electric effect and the Compton effect are very small and photon interaction is dominated by pair-production. This is a quantum effect in which the photon interacts in the electric field of a nucleus and is completely absorbed, producing an electron and positron. The electron continues and loses energy by *bremsstrahlung* (described below) and ionisation. Since the cross-section

for bremsstrahlung varies with energy while that for ionisation is approximately constant, bremsstrahlung dominates initially and many high energy photons may be produced (i.e. photons whose energy $> 2m_e$). Such 'hard' photons may subsequently pair-produce and the processes described are repeated. The positron also loses energy by bremsstrahlung and ionisation, but in addition, when its energy has decreased to significantly below m_e, it is captured by an electron and forms a positronium state which quickly decays by annihilation. The decay photons finally interact via the photo-electric and Compton effects.

Since the photons produce electrons and positrons and these in turn produce more photons, a 'shower' develops with the number of particles increasing exponentially with depth in the material. Correspondingly, the average energy of the particles decreases exponentially until all photons are below the threshold for pair-production. At this point, the photo-electric and Compton processes dominate and the photons are absorbed. Similarly, the electrons and positrons which are released in the shower continue to lose energy by ionisation and are eventually captured by atoms. Since the average energy per particle decreases exponentially the shower has a definite range which depends on the initial energy of the primary particle. Also, since all processes which take place are elastic, the total energy of the primary particle is deposited in the medium as ionisation.

Normally, elements with a high atomic number are used in detectors for precipitating such showers as the cross-section for pair-production varies with Z^2.

- **Electrons and positrons.** These particles are particular in that they have a very high charge-to-mass ratio compared to other charged particles and so undergo large vector accelerations in the electric field of the nucleus. The changes of velocity and hence momentum are compensated for by the radiation of photons. This process is known as bremsstrahlung. For a high energy electron, the momentum change can be large and the photon can carry a correspondingly high momentum. Such photons can subsequently cause pair-production as described above. The resulting shower is soon indistinguishable from that produced by a primary photon and so the same detector can be used for electrons and positrons as is used for photons.

- **Charged hadrons.** All charged hadrons (eg. protons, pions, kaons) have a much smaller e/m ratio than electrons and so their rate of bremsstrahlung energy-loss is lower. This means that they tend to have a far greater range in matter. In addition, if their energy is high (as in ALEPH), ionisation is slow in stopping them. These particles are therefore highly penetrating and can only be stopped by substantial amounts of matter

where the probability of an inelastic nuclear collision occurring is large. Such collisions lead to nuclear disintegrations and a subsequent shower of products which may ionise or induce further nuclear reactions. Thus a hadronic shower develops although in this case it should be noted that not all the energy of the primary particle is seen as ionisation and that some 30% is absorbed by inelastic nuclear processes. In physical scale, hadronic showers are much larger than electromagnetic showers and so hadronic calorimeters tend to be large.

- **Neutral hadrons.** Being uncharged, such particles do not ionise or suffer bremsstrahlung and so their only mode of interaction is by nuclear capture as described above. The resulting shower is indistinguishable from that produced by a charged hadron.

- **Muons.** Muons have unique interaction characteristics. Their high mass means they lose energy slowly by bremsstrahlung while their high energy means that their ionisation losses are low. In these respects they resemble charged hadrons. However, being leptons, they do not interact via the strong force and so cannot precipitate nuclear reactions. Consequently, such particles have an extremely long range in matter and can traverse all elements of the ALEPH detector and escape. Indeed, it is this characteristic which is used to identify muons.

1.1.2 Principles of detection techniques.

All detectors work essentially on the principle that moving charged particles ionise atoms in the detector volume. The charged particles may be the primary particle itself or charged secondaries (usually electrons) produced by interactions between the primary and matter in the detector. In any event, the end result is that the primary particle is absorbed completely or escapes and a quantity of ions are left in the detector volume. The presence of these ions is then detected in a variety of ways. For brevity, only the techniques actually employed in the ALEPH detector will be described here.

- **Scintillation detectors.** In certain crystals, the ions produced by charged particle interactions recombine with an electron and emit a quantum of light. The quanta are guided in the optically transparent crystals to photo-multiplier tubes where they strike a photo-sensitive material and release photo-electrons. The photo-electrons are accelerated in the electric field of such tubes and produce a shower of secondary electrons and an electrical impulse when they arrive at the anode. Such systems are usually linear and the final voltage pulse is proportional to the energy of the primary particle. In ALEPH, scintillators are used only in the Very Small Angle Luminosity Monitor which is described in Section 1.3.5.

- **Gas proportional chambers.** Generally, such chambers consist of long thin tubes with axial symmetry and a square or rectangular cross-section. The walls of the chamber are grounded and an anode wire runs along the axis and is charged at a high voltage (a few kV). Electron-ion pairs which are produced in the chamber are separated by the electric field and do not recombine. The electrons accelerate towards the anode wire and interact with other gas atoms ionising them. Thus for each electron liberated by a primary ionising particle, a quantity of secondary electrons is produced. This phenomenon is known as 'gas amplification'. The electrons finally reach the anode wire where they cause a change in voltage which is detected and recorded by the appropriate electronic circuits (described in detail in the relevant sub-detector sections). The final number of electron-ion pairs produced is proportional to the energy of the primary particle and so such detectors can be used as calorimeters. In ALEPH, the Electromagnetic Calorimeter (Section 1.3.3) and the Luminosity Calorimeter (Section 1.3.5) are examples of gas proportional detectors.

- **Streamer or drift tubes.** These are essentially gas chambers where the high voltage has been increased to such a level that the amplification factor is very large and the total amount of ionisation produced is not proportional to the primary energy. Ionisation produced in the vicinity of sense wires, induces a voltage drop on the wires which propagates towards both end-points. In some arrangements, the time delay between the arrival of the two pulses is used to establish the position of the ionisation along the wire. Such detectors are used in the Small Angle Tracker (Section 1.3.5), the Hadron Calorimeter (Section 1.3.4) and the Muon Detector (Section 1.3.7). The purpose of these detectors is to track the flow of charged particles rather than to determine their energy directly.

- **Tracking devices.** Such detectors are used to determine the spatial position of electron-ion pairs left in the wake of the primary particle. The ions are effectively the track of the particle and the process by which they are detected and the track reconstructed is unique to each sub-detector and will be described in the relevant section. The Time Projection Chamber (Section 1.3.2), the Inner Tracking Chamber (Section 1.3.1) and the Vertex Detector (Section 1.3.7) are all examples of tracking devices.

1.2 The LEP storage ring.

The *Large Electron-Positron Collider* (LEP) is a circular storage ring for accumulating, storing, accelerating and colliding counter-rotating beams of electrons and positrons. It is constructed inside a 4 m diameter circular tunnel of 27 km

circumference which runs at an average depth of 100 m under the countryside near CERN in Geneva. The tunnel is accessed by four experimental caverns (which measure 70 m by 21 m by 16 m and contain the detectors) and 18 vertical shafts.

Electrons and positrons are generated in the CERN accelerator complex by two linear accelerators operating at 200 MeV and 600 MeV. Positrons are produced by colliding an electron beam with a fixed target to produce high-energy photons which pair-produce e^+e^- pairs. The electrons and positrons are accumulated at 600 MeV in the Electron-Positron Accumulator (EPA) until a useful particle density has been achieved. They are then injected into the CERN Proton Synchrotron (CPS) and accelerated to 3.5 GeV. The CPS then passes the particles into the Super Proton Syncrotron (SPS) where they are brought up to 20 GeV before being injected into LEP.

The beams are steered around the LEP ring in a high vacuum beam-pipe by dipole bending magnets and are kept in focus by multipole magnets. The arrangement of magnets is repeated in standard *cells* each of length 79.11 m and consisting of;

- a defocusing quadrupole,
- a vertical orbit corrector,
- six bending dipoles,
- a focusing sextupole,
- a focusing quadrupole,
- a horizontal orbit corrector,
- another six bending dipoles and
- a defocusing sextupole.

There are 31 of these standard cells arranged in 8 arcs around the ring making a total of 4,464 steering and focusing magnets. On either side of each experimental cavern (the interaction points) there is sited a superconducting quadrupole which reduces the beam cross-sectional area and so increases the probability of an e^+e^- collision.

As the particles orbit the ring, they lose energy at a rate which varies as the fourth power of the particle energy. This *synchrotron radiation* has to be replaced just to maintain the same orbit. Energy is provided by the acceleration system which consists of 128 RF cavities powered by sixteen 1 MW klystrons. The operating frequency is 352 MHz and the peak RF voltage available is 400 MV. At the present time (the LEP phase 1), this RF power is capable

of accelerating the beams to 46 GeV rapidly. The actual rate of synchrotron energy loss at this point is 1.6 MW. In LEP phase 2, the addition of some 200 highly efficient superconducting cavities and an additional power of 12 MW will enable the beam energy to reach 100 GeV. Such an energy will enable the LEP experiments to study W^+W^- pair-production.

The particle beams in LEP are not continuous but are composed of discrete 'bunches' consisting of around 2.5×10^{11} particles. Each bunch is only a few centimetres long with a transverse diameter of around 100 μm. Four bunches are used, equally spaced around the ring, which lead to a current per beam of around 2 mA. The luminosity to date has been of the order of 5×10^{30} cm^{-2}s^{-1} which is about one-third of the design luminosity. The main limitation has been vertical smearing in the beam profile caused by spurious magnetic fields in the RF cavities. Some of the causes of these fields have been identified and their suppression is being pursued. The possibility of increasing the number of bunches to 36 which would increase the luminosity by a factor of 9 is also being explored.

1.3 The ALEPH detector.

The ALEPH detector is a symmetric, hermetic detector designed to detect and measure the energy, momentum and initial direction of particles produced in e^+e^- interactions at the LEP storage ring. ALEPH is designed to cope with events occurring at a rate of 1 Hz and at energies up to 200 GeV. In this work, LEP has been operating at energies near the Z^o mass (around 91 GeV) and so the main processes studied have been the decays of the Z^o boson. When the higher energies become available, other processes will dominate with perhaps the pair-production of W^+W^- bosons being the most interesting (in the absence of anything unexpected). At the time of writing, some 186,000 Z^o decays to hadrons have been observed at energies around the Z^o pole.

The detector is built around an axis of cylindrical symmetry which is collinear with the e^+e^- beam. It consists of several sub-detectors which are designed to track the particles (VDET, ITC, TPC), measure their energy (HCAL, ECAL) and monitor the luminosity of the LEP storage ring (LCAL, SATR, SALM). A general arrangement of the detector is shown in Figure 1.1.

Before discussing the characteristics and construction of each sub-detector, it will be useful to describe the coordinate system employed in ALEPH. The axis of symmetry of the detector and the direction of the electron beam is taken as the positive z-direction. The x-direction is then towards the centre of the LEP ring and the y-direction is vertical (the x- and z-axes being in a horizontal plane). In terms of polar coordinates, r is the radial distance from the origin in the xy plane, θ is the angle of inclination with respect to the positive z-direction

and ϕ is the azimuthal angle around the z-axis with respect to the zy plane. This coordinate system is shown in Figure 1.2.

1.3.1 The Inner Tracking Chamber.

The *Inner Tracking Chamber* (ITC) is a cylindrical drift chamber which tracks charged particles by detecting the ionisation they produce in the vicinity of an array of sense wires. It can provide up to 8 space coordinates with a precision of 100 μm in $r\phi$ and 3 cm in z. It is 2 m long and extends over the radial range 160 mm $< r <$ 260 mm. It consists of 960 sense wires, strung parallel to the z-axis, arranged in 8 concentric layers. The 4 inner layers are of 96 wires and the 4 outer layers are of 144. Each sense wire is at a positive potential of nominally 2.5 kV and is surrounded by a hexagonal grid of 5 field wires (which are grounded) and 1 calibration wire. Sense wires are composed of gold-plated tungsten and are 30 μm in diameter while the field and calibration wires are of gold-plated aluminium at 147 μm. A detail of the ITC wiring layout is shown in Figure 1.3.

The entire volume of the ITC is filled with a gas mixture of argon and ethane at atmospheric pressure. It is refreshed at a flow-rate of 50 l/h. The gas gain factor has been determined over a wide range of conditions and has been found to vary between 19,000 at 2.1 kV and 52,000 at 2.3 kV. Chamber operation is mostly around 2.2 kV where the exact gas gain is known.

The high-voltage system is based on the design which was used in the TASSO detector at DESY and is supplied via 60 sectors with each sector serving 16 wires on a 10 μA trip.

Each sense wire is connected at each end to a pre-amplifier. Pulses reaching the pre-amps are fed to an AZ board where they are further amplified, discriminated and passed to the *time expansion circuit.* This circuit works by driving a constant current onto a capacitor when the 'start' signal is received from one end of the sense wire. The current is switched off when the 'stop' signal arrives from the other end. The capacitor is discharged by another constant current at a rate which depends on the radial position of the wire. The ratio of these two currents is the *time expansion factor* and is different for each layer of wires. A signal is generated when the voltage on the capacitor reaches zero. The time at which this signal is generated is proportional to the charge on the capacitor and hence to the z-position of the ionisation which produced the pulse on the wire. In this way, the two pulses from each end of the sense wire are converted into a single signal.

The AZ board then sends two signals to the trigger processors. The first signal is the 'hit wire' latch which is sent to the *$r\phi$ processor.* This processor uses the data from each sense wire (hit or not) to address a RAM. The RAM is loaded with a 'hit wire mask' and will return a logic 1 from locations which correspond

to possible wire hits. In this way, patterns of hits which do not correspond to tracks emanating from near the origin are discarded. At the time of writing, this is the only signal which is used and so the ITC can only provide track projections in the $r\phi$ plane. In the future, it is planned to install the *space point processor* which will receive the second signal from the time expansion circuit. This processor works on the principle that if a track emanates from the origin, it will cross each layer at a different point in z. The delay between start and stop pulses arriving at the time expansion circuit will thus increase. However, the time expansion factor is calculated to compensate for this and the result is that such tracks will produce *coincident* signals after time expansion. Tracks which do not start from the origin will generally not be coincident.

Output from the trigger processors is available in 2–3 μs and provides the only tracking information for the Level 1 trigger. On receipt of a Level 2 'yes', the ITC event-builder is filled within typically 1.7 ms. The ITC EB reformats the data for JULIA and within typically 12 ms has fed it to the main ALEPH event-builder.

1.3.2 The Time Projection Chamber.

The *Time Projection Chamber* (TPC) is a large cylindrical drift chamber, centred on the interaction point, which measures the momentum, emission angle and ionisation density (dE/dx) of charged particles produced in the decay of the Z°. It is 4.7 m long by 3.6 m in diameter and is separated into two volumes by a high-voltage membrane which extends radially from the origin. The general arrangement of the TPC is shown in Figure 1.4. The TPC fully encloses the ITC.

The entire TPC volume is permeated by a 1.5 Tesla magnetic field. Charged particles from the interaction region follow helical paths in this magnetic field and ionise gas atoms in the TPC. The central membrane is held at a potential of -27 kV and the end-plates are grounded so that an electric field of 11 kVm^{-1} is maintained in the z-direction. Electrons liberated from ionised gas atoms drift towards the end-plates under the influence of the electric field. Each end-plate is divided into 18 sectors and it is these sectors which detect the arrival of the drift electrons and measure their number density for the dE/dx calculation.

The end-plate consists of a grid of cathode pads, 6 mm x 30 mm, aligned with their long axis radial. Above the pads are 3 layers of wires which are perpendicular to the radius. A detail of the pad arrangement is shown in Figure 1.5. The 3 wire layers consist of a gating grid 14 mm from the pads, a cathode grid at 8 mm and a sense and field grid at 4 mm. The mechanical details of the wire grids are given in Table 1.1 and their arrangement is shown in Figure 1.6.

The gating grid is normally kept at a positive potential and so absorbs any free electrons which may be present in the TPC as space charge. Immediately

Table 1.1: Mechanical details of sector grid wires in the TPC.

Grid	spacing	diameter	composition
Gating	2 mm	76 μm	Copper
Cathode	1 mm	76 μm	Copper
Sense	4 mm	20 μm	Gold-plated tungsten
Field	4 mm	127 μm	Gold-plated copper

following a bunch crossing, when an event may have taken place, the gating grid is grounded and drift electrons may pass. This effect is shown in Figure 1.7. In the volume of the TPC and up to the cathode grid, the electric field intensity is such that electrons achieve a constant drift velocity (typically 5.2 cm/μs) but do not cause secondary ionisation. Once they have passed the cathode grid however, they enter the field of the sense wires which is much greater and they accelerate rapidly towards the sense wires. This produces 'avalanching' in the volume close to the sense wires and induces a voltage pulse on them and on the pad immediately adjacent. Since the process is proportional, the sense wires can be read out for position and intensity of ionisation. The pads are read out for position alone.

The pattern of pad hits represents the projection in the $r\phi$ plane of the curved, 3-dimensional track of a charged particle. Since the drift velocity is known, the time delay between the bunch crossing in LEP and the pad hit yields the z-coordinate of the track-point. In this way, up to 21 3-dimensional coordinates can be determined for a track in the TPC.

The 41,004 pad readouts in the TPC are pre-amplified then passed in groups of 16 to fast ADCs and then onto a farm of 660 *time projection digitisers* (TPDs) which shape, digitise and adjust the gain of the signals. The TPDs are read out by 36 *time projection processors* (TPPs) whose tasks are mainly data-formatting and calibration. The TPDs in each each end-cap are supervised and readout by 2 end-cap event-builders (EBs), while one further event-builder handles common tasks. Finally, all data are passed to the main ALEPH event-builder for reconstruction.

The TPC is fitted with a laser ionisation system for calibration purposes. Two Nd–YAG lasers emitting UV light of wavelength 266 nm are set up, with one to serve each side of the TPC. The lasers are fired at a rate of between 1–3 Hz and produce pulses of 5 ns duration with an energy typically of 4 mJ. The beam is guided along a 10 m optical path to the end-plate where it is split into 3 parallel components which run along the outside of the inner field cage, parallel to the z-axis and separated by 120° in ϕ. The beams strike a

succession of 4 partially reflecting mirrors and a final pentaprism which break each beam up into 5 separate beams at a range of angles between 18° and 90° in θ. Each laser 'shot' thus produces 15 tracks in the TPC. The TPC is triggered on the initiation of the laser shot and so the drift velocity can be determined from the time delay between the shot and the arrival of the pad signals. Also, since the laser light is unaffected by the magnetic field, the tracks should be reconstructed as straight lines. By studying the spatial positions of the reconstructed laser tracks, electric and magnetic field inhomogeneities and mechanical misalignments can be detected and corrected for by altering calibration constants in the TPC pad readout software.

The TPC gas is a mixture of argon and methane in the ratio 91:9. The gas is continually replenished at a rate of 300 l/h and the oxygen and water content are controlled by filters to be < 3 ppm and < 5 ppm, respectively.

The TPC's ability to measure the position in space of a track coordinate depends on the path of the track, with the greatest accuracy for tracks which have a high θ-angle and are radial. Low-θ tracks and those which have a high tangential component are measured with less accuracy. The $r\phi$ coordinate can be determined to 160–400 μm and the z coordinate to 0.7 mm for a track at $\theta = 90°$ and 2.3 mm for $\theta = 20°$. This leads to a momentum resolution of $\Delta p/p^2 = 1.2 \times 10^{-3}(\mathrm{GeV/c})^{-1}$. This corresponds to an error of $\pm$ 0.12 GeV/c in a 10 GeV/c track.

In addition to momentum measurement, dE/dx can be measured to better than 4.5%. This accuracy allows the TPC to distinguish between electrons and pions and between pions and kaons to better than 2 standard deviations for the momentum range 2–20 GeV/c.

1.3.3 The Electromagnetic Calorimeter.

The *Electromagnetic Calorimeter* (ECAL) detects and determines the energy of photons and electrons produced in ALEPH. It is a largely hermetic, cylindrical sub-detector which surrounds the TPC and is entirely contained within the magnet coil and its magnetic field. It covers the entire range in ϕ and down to within 10° of the beam line in θ. It is composed of 3 sections, the barrel and 2 end-caps. Each section consists of 12 modules. The general arrangement of the ECAL is shown in Figure 1.8. Each module is independent and all operate in an identical manner.

Each module of the ECAL consists of 45 layers of lead sheeting interspersed with layers of wire chambers. Photons and electrons interact with the heavy lead nuclei by pair-production and bremsstrahlung respectively and a shower is produced which leads to ionisation in the wire chambers. The amount of ionisation is proportional to the energy of the primary particle.

For readout, the 45 layers are grouped into 3 'storeys'. The first storey,

nearest the beam, is 4 radiation lengths deep and consists of 10 lead layers, each 2 mm thick. The second storey is 9 radiation lengths deep and consists of 23 layers of 2 mm lead. The outer storey, also 9 radiation lengths deep, consists of 12 layers of 4 mm lead.

The wire-chambers are constructed from rectangular aluminium extrusion channels on 5 mm spacing and run radially in the case of the end-cap petals and axially in the barrel modules. Each channel contains a 25 μm, gold-plated tungsten anode wire. On the closed side of the extrusion (the inboard) is the lead and it is from this direction that the shower particles come. On the other side (the outboard) is mounted a PCB which is sectioned into cathode pads. Ionisation in the wire chambers produces voltage pulses on the wires and on the pads. The pads are read out in storeys and give positional and energy information since they are sensitive to the *amount* of charge deposited on them. All wires in a plane are read out in parallel and so can only indicate the depth to which a shower has penetrated.

The pad shapes and locations are varied from layer to layer in a projective manner so that a particle coming from the origin will pass through pads which are part of the same tower. Each tower supplies 3 signals and in total there are 221,184 pad channels in the ECAL. These are multiplexed by 32 at the front-end amplifiers and again by 8 at the ADCs. Signals from the 1,620 wire channels (45 layers x 36 modules) are also amplified and converted to digital signals. The output from the ADCs is fed to the *readout controllers* (ROCs) for pedestal subtraction, gain correction and formatting before being passed onto the ECAL event-builder. This event-builder is in communication with the ECAL VAX for online monitoring of the ECAL performance. Finally, the processed data is presented to the main ALEPH EB.

The gas mixture used is of Xenon and CO_2 in a 80:20 ratio. Gas gain in each module is continually monitored by a Fe^{55} source in a monitor chamber which is subject to the same gas flow and HV conditions as the module. The Xenon content of the mix is carefully controlled since the gas gain has been found to be extremely dependent on it (with a change in concentration of Xe by 1% leading to a change in gain of 9%). This is made difficult by the fact that gas absorption into Mylar which is used in the wire chambers proceeds at a different rate for the two gases. Gain is also affected by the out-gassing of Freon which was used for cleaning during manufacture and this has to be continually scrubbed.

Calibration of the ECAL has been carried out by exposing some modules to a test beam of photons and electrons. In addition, radioactive gas, cosmic muons and high angle Bhabha electrons have provided a relative calibration for all modules.

The ECAL can determine energies with a fractional error of $18\%\mathrm{GeV}^{\frac{1}{2}}E^{-\frac{1}{2}}$ and position with an error of $6.8\ \mathrm{mm}\mathrm{GeV}^{\frac{1}{2}}E^{-\frac{1}{2}}$ which is equivalent to $\pm$ 0.8 GeV

and ± 2.3 mm for a 10 GeV electron. For a 95% efficiency in accepting electrons, pion contamination has been shown to be 1.1%

1.3.4 The Hadron Calorimeter.

The main task of the *Hadron Calorimeter* (HCAL) is to act as an absorber and converter medium for high energy hadrons. As mentioned in Section 1.1.1, such particles have a great range in matter and so the scale of the HCAL is large. It therefore serves, in addition, as the main structural support for the rest of the detector and, since it is made largely of steel, as the return path for the magnetic flux from the magnet. It is similar in design to the ECAL, being composed of a barrel and two end-caps, and is also modular. The barrel is composed of 12 rectangular modules and each end-cap of 6 petals.

Each module consists of 23 layers of steel each of which is fronted by a plane of streamer tube detectors. All steel layers are 5 cm thick except for the last which is 10 cm thick to provide a final screen for hadrons before the outer muon detector is encountered. The streamer tubes are made from extruded plastic in the form of 8 cells of 1 cm^2 section and run axially in the barrel modules and vertically in the end-caps. Each cell has a centrally strung, 100 μm wire which is directly read out for trigger information. The open ends of the streamer tube extrusions face onto a grid of copper cathode pads which are read out for positional and energy information. These pads are arranged in projective towers as in the ECAL, however, the HCAL grid is much coarser than that of the ECAL and 1 HCAL tower covers an angular range (roughly $3.7^o \times 3.7^o$) which corresponds to 14 ECAL towers. In addition to the pads, strips parallel to the wires which pick up an induced signal are read out for digital positional information.

The gas used is a mixture of argon, CO_2 and n-Pentane in the ratio 21:42:37. This gas was found to produce quickly dense ion clouds in a region close to the wire when a shower particle passed through.

The HCAL is able to determine hadron energies with a fractional error of 0.84 $GeV^{\frac{1}{2}}E^{-\frac{1}{2}}$. This corresponds to an error of ± 2.6 GeV at 10 GeV. Muons with momentum > 5 GeV/c will traverse the HCAL completely. It can discriminate between hadrons and muons such that the probability of mis-identifying a kaon or a pion as a muon is 1.6% and 0.7% respectively.

1.3.5 The Luminosity Monitors.

While most of the sub-detectors of the ALEPH detector are used to study particles produced in the decay of the Z^o, there are some whose purpose is to determine the *luminosity* of LEP. Luminosity is simply a measure of the rate at which 'reaction opportunities' are created and is independent of the process

concerned. The luminosity (L), the cross-section (σ_x) and the reaction rate (R_x) for any process, x, are related simply by;

$$\sigma_x = \frac{R_x}{L} \tag{1.1}$$

The cross-section for Bhabha scattering is known to 3rd order in QED. If the Bhabha reaction rate is measured accurately, then the luminosity can be calculated. For any other process then, the reaction rate can be measured and, knowing the luminosity, the cross-section can be calculated. Having measured the hadronic width of the Z^o, it was accurate knowledge of the luminosity which enabled the ALEPH collaboration to determine precisely the number of light neutrino species and thus deduce that there are only three families of fundamental particles [5].

- **LCAL.** The *Luminosity Calorimeter* is designed to measure the energy of Bhabha electrons in the angular range 55 mrad $< \theta <$ 155 mrad. It is in the form of four semi-cylindrical modules, of inner radius 10 cm, outer radius 55 cm and length 45 cm. On either side of the vertex, a pair of modules is fitted between the beam-pipe and the ECAL end-cap. The position of the LCAL can be seen in Figure 1.1

  In principle of operation and readout, the LCAL is identical to the ECAL. The construction is different however, and the LCAL has 38 layers of lead and wire-chambers read out in 3 storeys. Starting from the vertex, the three storeys are; 9 layers of 2.8 mm lead, 20 layers of 2.8 mm and 9 layers of 5.6 mm. Each layer has 112 wires in vertical alignment which are connected in parallel for readout. Each module is sectioned into 384 projective towers (1 tower corresponds to 3 pad storeys).

  In performance, the LCAL can determine energy to within a fractional error of 0.20 $\mathrm{GeV}^{\frac{1}{2}} E^{-\frac{1}{2}}$ and position to $\pm$ 2.5mm in x and y.

- **SATR.** The *Small Angle Tracker* is designed to track low angle Bhabha electrons in the angular range 40 mrad $< \theta <$ 90 mrad. Like the LCAL, it is composed of 4 semi-cylindrical modules arranged in pairs and positioned on the inside of the LCAL. In this way, Bhabha electrons traverse the SATR before striking the LCAL. Each module is composed of 9 half-planes stacked along the z-direction. Each half-plane, in turn, consists of 4 sectors each of which has 14 drift tubes aligned circumferentially. The general arrangement of one half of the SATR and LCAL is shown in Figure 1.9.

  As described in Section 1.1.2, drift tubes are used to determine the position of ionisation produced by the passage of charged particles and are not operated in a proportional mode. Hence, the gas gain is not important

(so long as it is large). The gas used is a mixture of argon and CO_2 in the ratio 90:10. Isopropyl alcohol is added at a nominal level of 1%. The tubes are formed from square section brass with a side of 9.5 mm. The anode wires are gold-plated tungsten, 25 μm thick. Voltages pulses from the wires are pre-amplified and fed to time-to-digital converters (TDCs) before being passed to the event-builder.

The SATR has an angular resolution of 0.05 mrad in θ and a position resolution per drift tube of 320 μm.

- **SALM.** The *Very Small Angle Luminosity Monitor* is designed to detect and measure the energy of low angle Bhabha electrons at θ of around 5 mrad. The SALM consists of 2 pairs of rectangular detectors (3 cm x 4 cm in cross-section and 14 cm deep) fitted onto the side of the beam-pipe on either side of the interaction region and 7.7 m from it. The SALM is therefore 6.5 cm from the beam at its closest.

  Each SALM module is a scintillation detector and is composed of 10 layers of tungsten interspersed with scintillator strips. The first layer of tungsten is 15.2 mm thick (to protect the SALM from synchrotron radiation close to the beam line) and the subsequent 9 are 7.2 mm thick. The scintillator layers are optically coupled in pairs to photo-multiplier tubes which are readout via ADCs to the event-builder.

  The SALM's main feature is its ability to operate at a rate of around 5 Hz. This allows it to be used to provide a fast measurement of the relative luminosity of LEP and to measure the synchrotron radiation and off-axis particle fluxes. In this way, it serves as a 'luminosity meter' and 'noise meter' for ALEPH.

1.3.6 The Superconducting Magnet.

The TPC's performance at tracking charged particles can only be taken advantage of to measure particle momenta if the entire volume of the TPC is immersed in a uniform magnetic field with a high field strength. Such a field is provided by the ALEPH superconducting magnet coil.

The coil consists of a main winding 5.3 m in diameter and 6.35 m long and two 40 cm long compensating coils at each end. The wire used is a niobium-titanium alloy operated at 4.3 K, at which temperature it is superconducting. At a nominal field strength of 1.5 Tesla, the current in the coil is 5000 A and the stored energy 136 MJ. The field occupies a volume of some 123 m^3 and is uniform throughout to within 0.2% with corresponding sagitta distortions in the TPC of < 0.2 mm.

1.3.7 Sub-detectors planned for commissioning.

Many planned sub-detectors were not commissioned by the time the data used in this thesis were taken. For completeness they are described briefly here.

- **Muon Detector.** The muon detector consists of two layers of streamer tubes positioned outwith the HCAL and covering some 85% of the ALEPH outer surface. The two layers are approximately 5 m from the interaction region and are 50 cm apart. Being outside the final 10 cm thick steel layer of the HCAL, the probability of any particle other than a muon reaching them is low. The streamer tubes are essentially the same as those used in the HCAL, although the readout is different. One side of the streamer tube is faced with a plane of 4 mm aluminium strips on a 10 mm pitch which run parallel to the wires. These are the x-strips. The other side has 10 mm wide y-strips on a 12 mm pitch which are perpendicular to the wires. Induced voltage pulses on these strips are read out and from the corresponding x and y locations of the strips, the position of the muon track in each plane is determined. Accuracy is around 40 mrad in θ and ϕ.

- **Vertex Detector.** The vertex detector (VDET) is designed to track charged particles very close to the interaction region. It consists of two layers of silicon semiconductor with aluminium tracks etched on a 100 μm pitch. Ionisation by charged particles traversing the semi-conductor produces electron-hole pairs which drift to the aluminium electrodes and induce a voltage pulse. The pulses are pre-amplified and are read out to ADCs . The principle is similar to that of a gas tracking chamber.

  Highly accurate measurements of the particle trajectories in the vertex region will allow detailed study of the τ-lepton and b-mesons. These particles decay very rapidly, while still in the beam-pipe, and are never directly observed. However, if their decay products are tracked accurately, the decay vertex can be reconstructed. In this way, the lifetime of such particles can be determined.

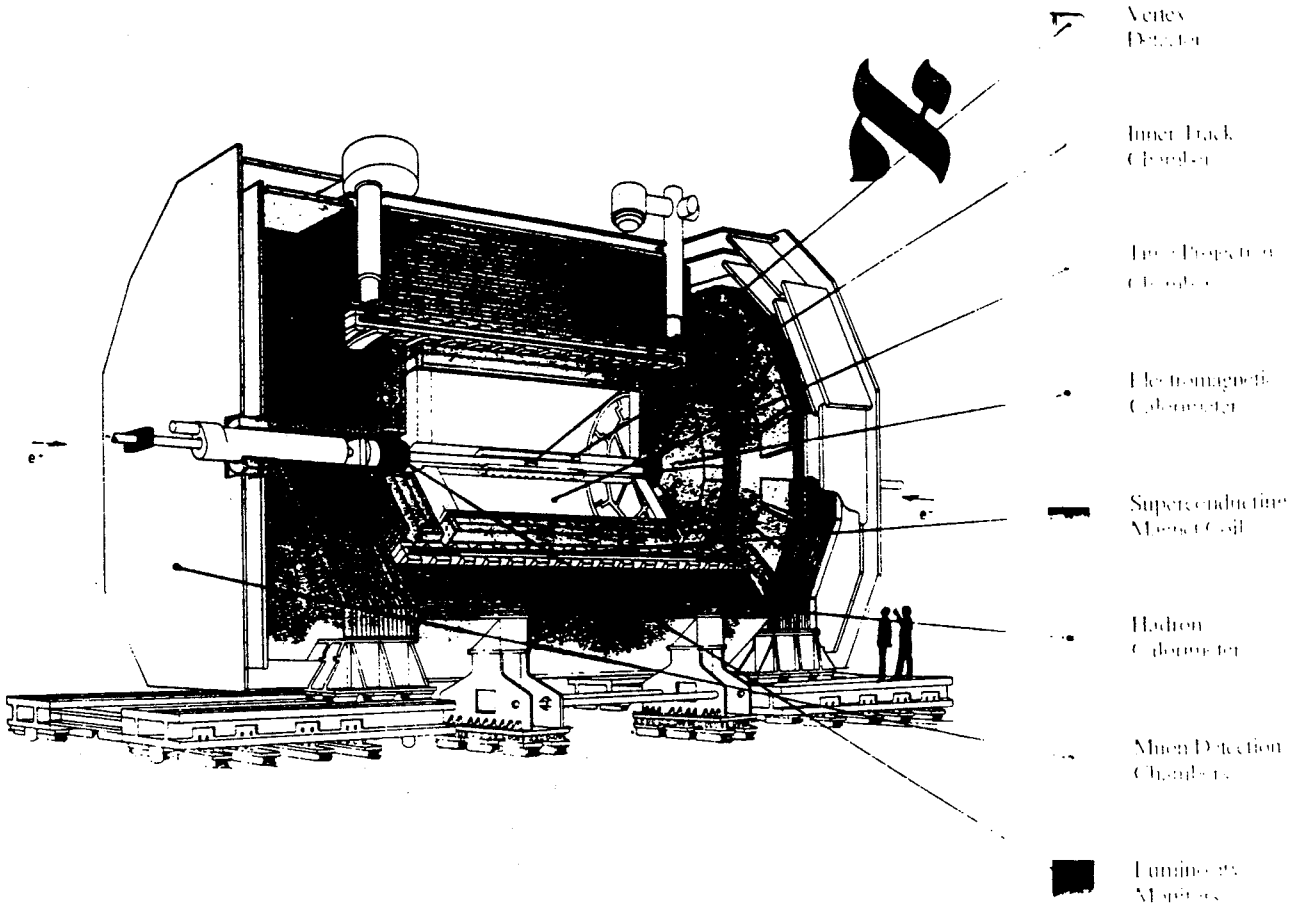

Figure 1.1: General arrangement of the ALEPH detector.

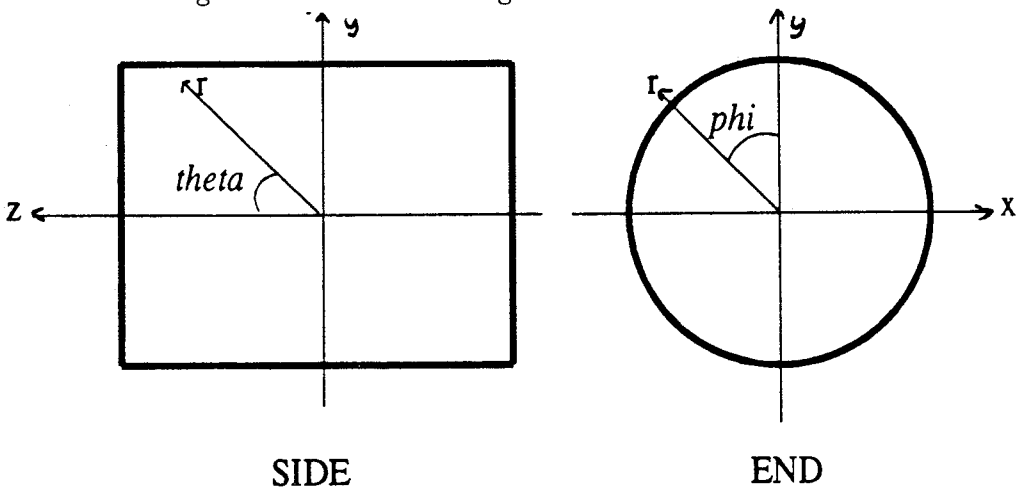

Figure 1.2: ALEPH coordinate system. The positive z-direction is the direction of the electron beam and the x-axis is towards the centre of the LEP ring. The y-axis is vertical.

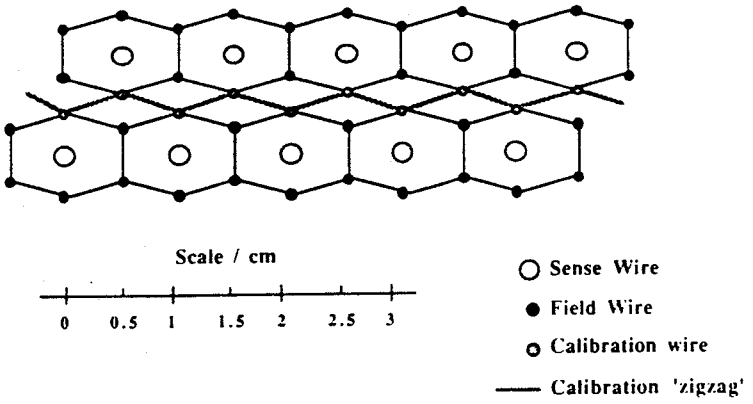

Figure 1.3: ITC wiring arrangement.

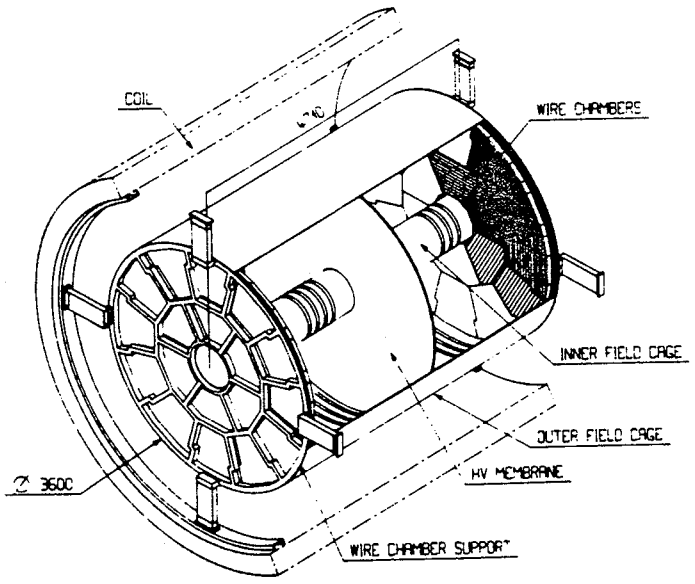

Figure 1.4: General arrangement of the TPC, showing the High Voltage membrane and the wire-chamber end-plates.

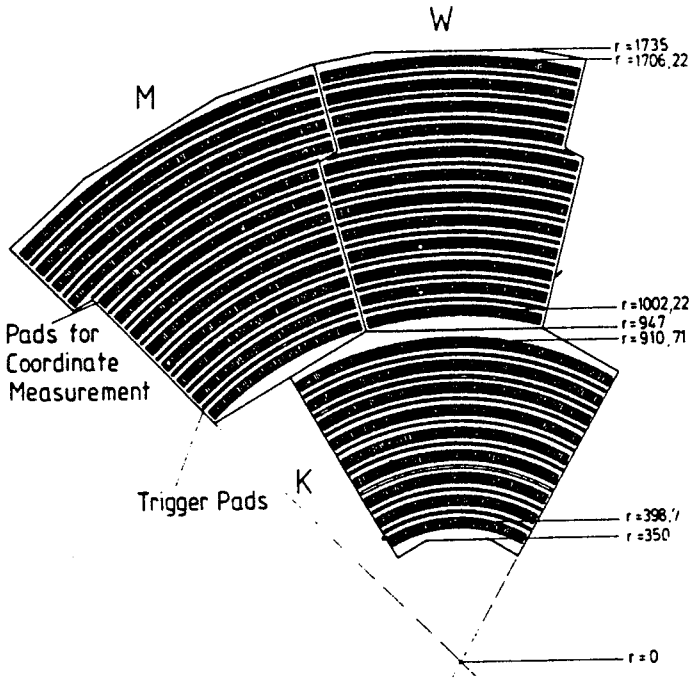

Figure 1.5: Detail of the TPC pad arrangement showing the relative positions of the read out pads (broad) and the trigger pads (narrow concentric strips).

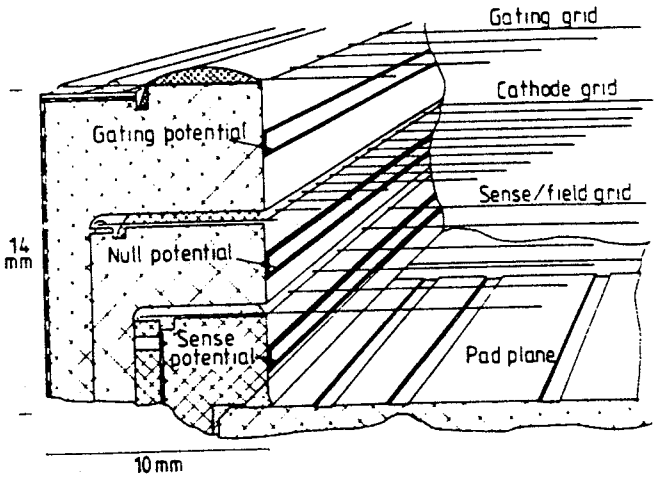

Figure 1.6: Arrangement of the 3 sets of grid wires on the sector end-plates in the TPC.

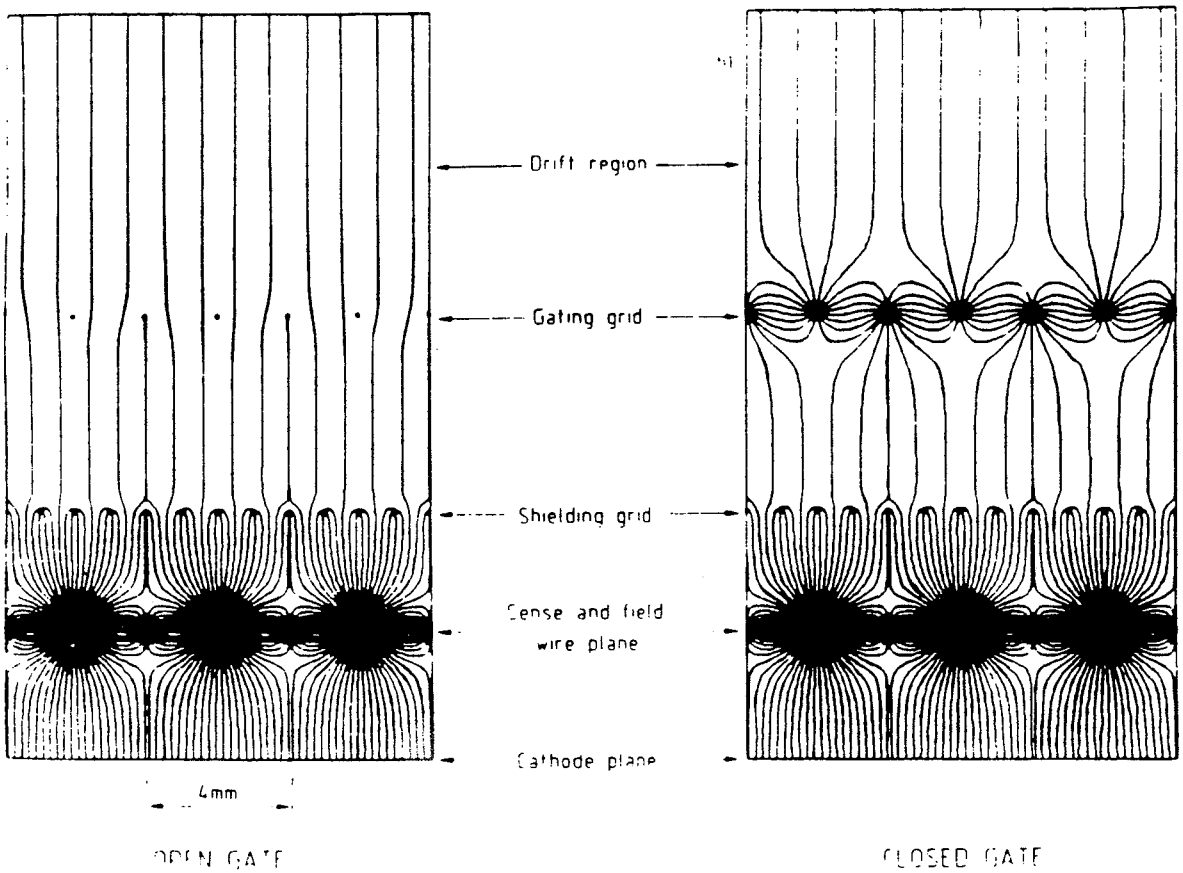

Figure 1.7: Effect of charging the gating grid on the electric field near the TPC end-plate. When the gate is closed, electrons drift to the gate grid-wires and do not reach the sense wires.

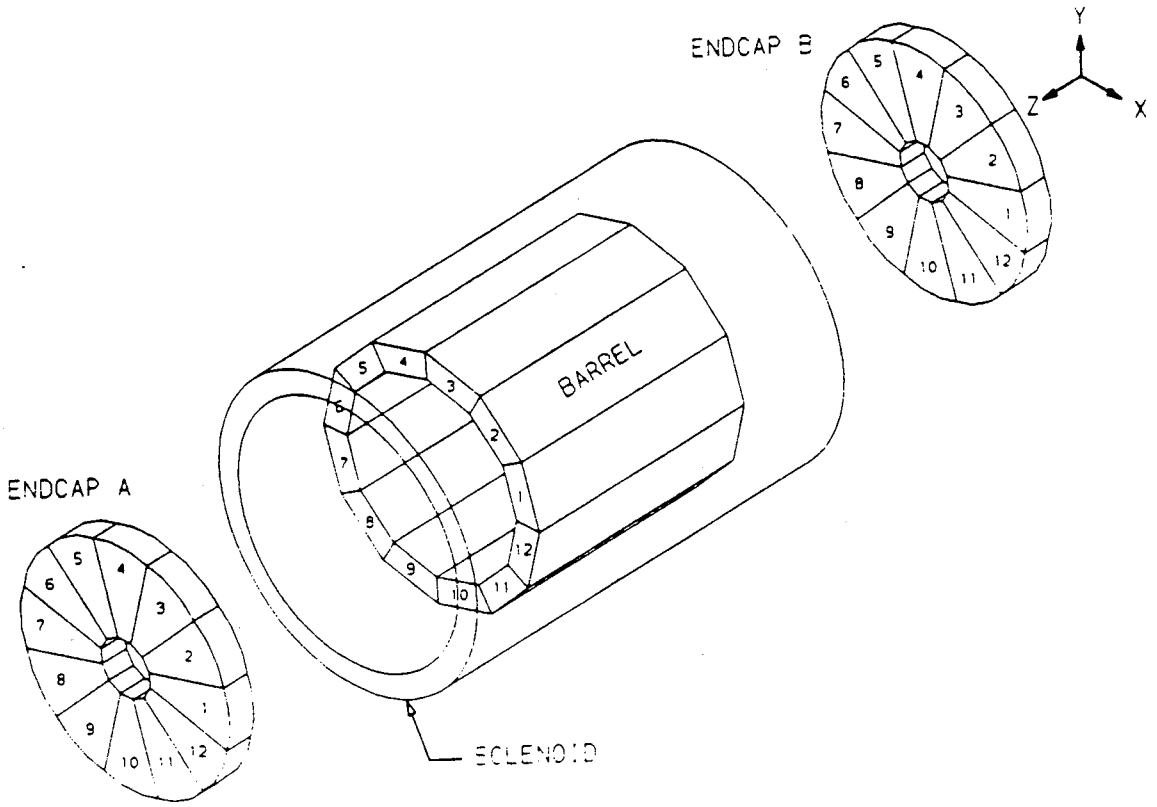

Figure 1.8: General arrangement of the ECAL. End-cap B is identical to end-cap A.

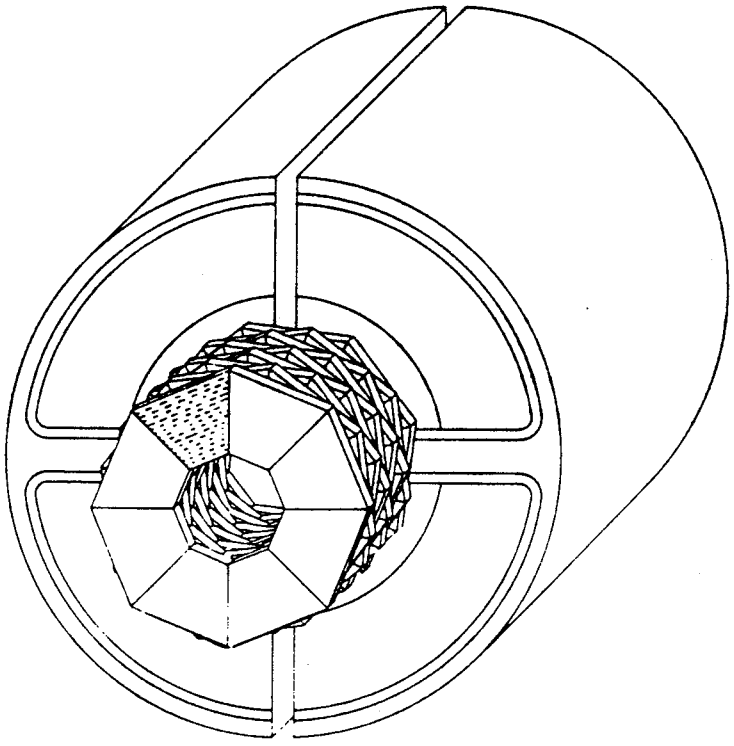

Figure 1.9: SATR and LCAL modules. The LCAL is the larger, cylindrical object and the beam-pipe passes through the co-axial hole in the centre of both sub-detectors.

Chapter 2

Data Acquisition and Software.

2.1 Introduction.

Ideally, the physicist studying an event at the ALEPH experiment would be provided with the identity, the charge, the momentum-energy 4-vector, and vertex of origin of all particles in the event. However, as has been described in Chapter 1, the interactions of particles from the event with the detector produce a collection of different types of electrical signals. These may be digital or may be analogue voltage levels or may be time-encoded such that the time delay between a rising and falling edge contains the information. The task of the data-acquisition system is to digitise and collect these data, apply known corrections, reconstruct the desired parameters of the event and present them in a format which can be analysed using a standardised routine.

2.2 Data Acquisition.

2.2.1 Readout hierarchy.

The sub-detectors in ALEPH are designed to be largely autonomous with respect to readout and data acquisition. This requirement arose from the need to be able independently to test, calibrate and debug the modules during construction and commissioning of ALEPH. To this end, a tree-like hierarchy was adopted with each element in the tree acting as a master of elements nearer the detector and as a slave to elements which are downstream[1] of it. Data connections, therefore, only exist in 'up-down' directions parallel to the data flow.

[1]The data flow is defined as being from the front-end electronics in the detector to the main computer which stores the reconstructed, compressed data.

There are no connections across the flow, between elements at the same level in the hierarchy. This system allows any element (except the first and the last) to be skipped and its job to be performed by the next element downstream if this should be necessary. A diagram of the ALEPH readout is shown in Figure 2.1. In addition, the readout can be 'partitioned'. That is to say, any subset of readout controllers can be operated independently of the rest of the detector. This enables test and debug work to be carried out on any subset (for example, the TPC plus one ECAL end-cap) while the remainder of the detector is read out on a different partition [3].

The task of each element at each level of the hierarchy is as follows:

- **Read Out Controllers.** Once triggered, the ROCs read out the front-end modules, apply calibration procedures if required and format the data.
- **Event Builders.** The EBs receive data from the ROCs and build a sub-event at sub-detector level.
- **Main Event Builder.** The MEB combines the sub-events from the various EBs and forms the complete event.
- **ALEPH event processor.** The AEP (also known as the Level 3 trigger) performs data-reduction on the complete event.
- **Host.** The host computer stores the data on disk and provides all facilities for on-line event display, analysis and detector performance monitoring as well as acting as the link (via shared disks) to the event reconstruction facility.
- **FALCON.** The event reconstruction (described in Section 2.2.3) in the ALEPH experiment is done 'quasi-online' in a dedicated facility which then outputs the reconstructed event to the main CERN computer centre for storage and analysis.

2.2.2 Trigger system.

The task of the trigger system is to filter selectively the signals produced by the detector during operation and so reduce the quantity of data which the data acquisition system must handle. Thus the trigger system must be capable of rejecting, with a high efficiency, signals which come from background processes, while accepting real physics processes. In addition, there must be no rejection of new physics processes which may produce unfamiliar signatures in the detector. Background comes from a variety of sources such as cosmic rays, beam-gas interactions, off-axis beam particles colliding with the beam-pipe and muons from collimator interactions. New physics processes may include such

phenomena as single tracks, mono-jets or isolated energy clusters. To achieve this, the ALEPH trigger system operates at three levels. These are:

- **Level 1** The typical time between bunch crossings is of the order of 23 μs. The Level 1 trigger is designed to read the signals produced immediately after a bunch crossing and to decide whether to proceed with the event within 5 μs, thus ensuring the next bunch crossing is always captured. Its decision is based on information from the ITC, the ECAL and the HCAL. The ITC, from its $r\phi$ processor, reports on the presence of charged tracks emanating from the vertex. The ECAL and HCAL are subdivided into 72 segments which are summed independently. With this information, the Level 1 trigger logic then decides whether a valid trigger has been received. As an example, the logic state required for the single muon trigger is as follows:

  $$\texttt{T(Single muon)} = \texttt{HCT1} \oplus \texttt{HCTWT3} \oplus \texttt{ITC}$$

  where:

`HCT1`	=	Deposition of at least 0.8 Gev in one HCAL segment
`HCTWT3`	=	HCAL wire signals in all stacks
`ITC`	=	ITC track 'coincident' with HCAL deposit

  The Level 1 trigger-rate is designed to be less than 500 Hz (from a bunch crossing frequency of 50 kHz) at worst case background. In practice, it has been of the order of 0.5 Hz. While this has largely been due to the low luminosity achieved during the start-up phase of LEP, the low background noise levels of the LEP machine have also contributed.

- **Level 2** The Level 2 trigger is based on data from the TPC which are analysed by hard-wired processors, programmed to search for charged tracks from the beam intersection region. Signals for these processors are provided by 1152 special 'trigger pads' in the TPC sectors. These pads are in the form of thin annular sections, 6 mm wide (in the r-direction) and extending over 15° in ϕ. If no acceptable charged tracks are found in the TPC then the event is rejected. This decision is available in about 60 μs. In this way, the Level 2 trigger enables ALEPH to be ready to analyse the third bunch crossing after the one which initiated the trigger. The first and second crossings are lost.

- **Level 3** The Level 3 trigger (also known as the 'ALEPH event processor') is a real-time process (or series of processes) which runs on the completed

dataset from the event-builder. At the time of writing, this trigger has been carrying out data compaction but has not been allowed to reject events. In future, once its efficiency has been proven, it will be used to reduce further the total data output by identifying and rejecting background events in real-time.

2.2.3 Event reconstruction - FALCON.

The completed event which is read out by the data acquisition system is stored by the host computer on disk. The disk volumes are, however, accessible by another dedicated computer system which reconstructs the event on-line. This facility is known as FALCON and consists of a boot node microVAX 3600 with a 622 Mbyte disk and 296 Mbyte tape unit which acts as a server for a farm of 12 Vaxstation 3100s. These units are screenless and diskless and serve as batch queues for parallel processing of events. The main disks, which are shared with the host, are three RA90s each of 1.2 Gbyte capacity. Two monitor workstations are also included together with a LAN bridge to provide communications with CERN. All processors in FALCON have a power of 2.7 mips.

FALCON runs a program called JULIA (described in Section 2.3.3) which generates the kinematic data relating to the particles in the event from the detector response information compiled by the host computer. The kinematic data are then formatted according to the requirements of the ALEPH standard.

2.3 Software.

It is a frequently applied technique in studying such events, to generate a sample of simulated events which embody various fundamental physical parameters and then to analyse the events from the simulation in the same way as experimental data. Comparison of the simulation results with the experimental data results then provides a measure of the validity of the physical parameters which were input into the simulation. To simplify the execution of such a task a suite of computer programs has been produced which allows the user to generate simulated events, which have the same data format as reconstructed data events, from a wide range of event generators. In this way, analysis code written for data can be applied to simulations with no modifications.

The most common language used in the analysis of such data is FORTRAN. Consequently, this language was chosen for the suite of programs produced. In addition, to handle the management of the large amounts of data which are produced in ALEPH, the BOS system of memory management was employed [6]. This system was originally developed for the PLUTO collaboration at DESY. In essence, the BOS system declares a fixed set of data arrays, with pre-determined space allocated for all pieces of data which may be required. These arrays are

stored in one common-block which can then be accessed by subroutines designed to unpack whatever data item may be required by the analysis routine.

2.3.1 Event generation - KINGAL.

Physicists studying the many possible processes which take place in ALEPH have at their disposal a large library of *event generators*. These are computer programs which will generate a simulated event according to whatever physical process is to be studied. Thus there exist QCD generators, muon-pair generators, Bhabha generators and so on. In attempting to replicate the physics of the process accurately, each generator has a set of input parameters which are involved in the calculation of the characteristics of the process such as the differential cross-section, momentum spread etc. Some of these parameters, such as particle lifetimes and the mass of the Z^o are well-established while others such as the Higgs mass are unknown and have to be guessed. Usually, all these parameters can be varied by the user to produce simulated events whose characteristics reflect the choice of the parameters. The generators have to simulate processes which in nature may be random and so the technique of Monte Carlo integration is usually employed to extract a value for each quantity required. Because of this, such a program has come to be known as a *Monte Carlo*.

Since the many different generators have been written by a corresponding number of different authors, there is little standardisation in the final format of the simulated data. KINGAL was therefore developed to enable a standard event format to be produced from the many different generators available.

The procedure to generate simulated events using KINGAL is as follows:

- The user provides a 'CARDS' file which contains the values to be used for any parameter which is to be varied. This is done with reference to the manual for the particular generator being used which describes the physics employed therein.
- The generator is defined during a dialogue with KINGAL.
- KINGAL selects the generator program from a library, alters the parameter values in accordance with the CARDS file and runs the generator, producing the required number of events.
- The events are processed on output and the particle identities, origins and 4-vectors are stored using the BOS system in a generator-independent format.

In this way, KINGAL acts as an interface between the BOS system and the various event generators available and provides a standard format output for analysis or later processing. Data at this stage are usually referred to as *Monte*

Carlo truth. Thus, simulated events from QCD, $\tau^+\tau^-$ or $\gamma\gamma$ generators, for example, all have the same output format and can be analysed by the same code.

2.3.2 Detector response - GALEPH.

It would not be reasonable to expect the global event shape parameters from Monte Carlo truth data to match experimental data. This is because, on passing through the detector, the underlying event is perturbed by various systematic effects. For example, particles may be lost due to cracks[2] in the detector, particles close together may be combined by the calorimeters, uncertainty in momentum may lead to directional and origin smearing and non-interacting particles (such as neutrinos) will escape detection entirely.

Thus, to produce a more realistic simulation, the Monte Carlo truth events are processed through GALEPH. This routine contains all the information relating to the detector geometry and produces the detector response signals which would occur if the simulated particles were actually to pass through ALEPH. In keeping with the standardisation system used throughout ALEPH, these data are stored in appropriate BOS banks. Output from this routine is identical in process level to that which is passed by the Level 3 trigger.

2.3.3 Event reconstruction - JULIA.

The final stage in data processing and in Monte Carlo simulation is the same. This is the point where the detector digitisations, coming either from the real detector or from the simulation, GALEPH, are translated back into kinematic data relating to the particles from the event. This is the program which is run on experimental data by FALCON.

JULIA consists of a series of algorithms which perform several tasks designed to extract the required data:

- Track-finding algorithms look for space-points in the TPC which fit well to a helix. From the curvature, the momentum and charge of the particle is established and from the χ^2 of the fit, the error is determined.
- Calorimeter signals are integrated to provide values for energy, and from their location, links are made to TPC tracks.
- Neutral particles are identified by isolated calorimeter objects and the absence of ITC or TPC tracks.

[2]Spaces between detector elements.

Again, all processing of data through JULIA is done under the auspices of the BOS system and the final output format is identical whether the original data source was any one of a number of different Monte Carlo generators or the real detector itself.

2.3.4 Data analysis - ALPHA.

As has been described, the data are finally presented in a standard format for analysis. However, this format is not read easily by simple FORTRAN code and so to facilitate the user's task of analysing the data's physical properties, the program ALPHA has been provided.

ALPHA consists of a framework and a series of functions and subroutines which unpack the data from the BOS banks, calculate various physical parameters relating to the particles or the event and present these as values of certain named variables in a common-block. The user's analysis routine then becomes a subroutine within ALPHA and can use pre-determined variables for particle properties.

For example:

`QE(I)`	=	The energy of the Ith track
`QPX(I)`	=	The momentum in the x-direction of the `I`th track
`QCOSA(I,J)`	=	The cosine of the angle between the `I`th and `J`th tracks

In addition, subroutines can be called which return such global event shape parameters as the sphericity or thrust of the event.

ALPHA saves the user the effort of constructing complicated software algorithms to unpack the BOS banks and provides quick access to simple physical quantities. The user's intellect can then be devoted to the analysis of the physical problem to be studied.

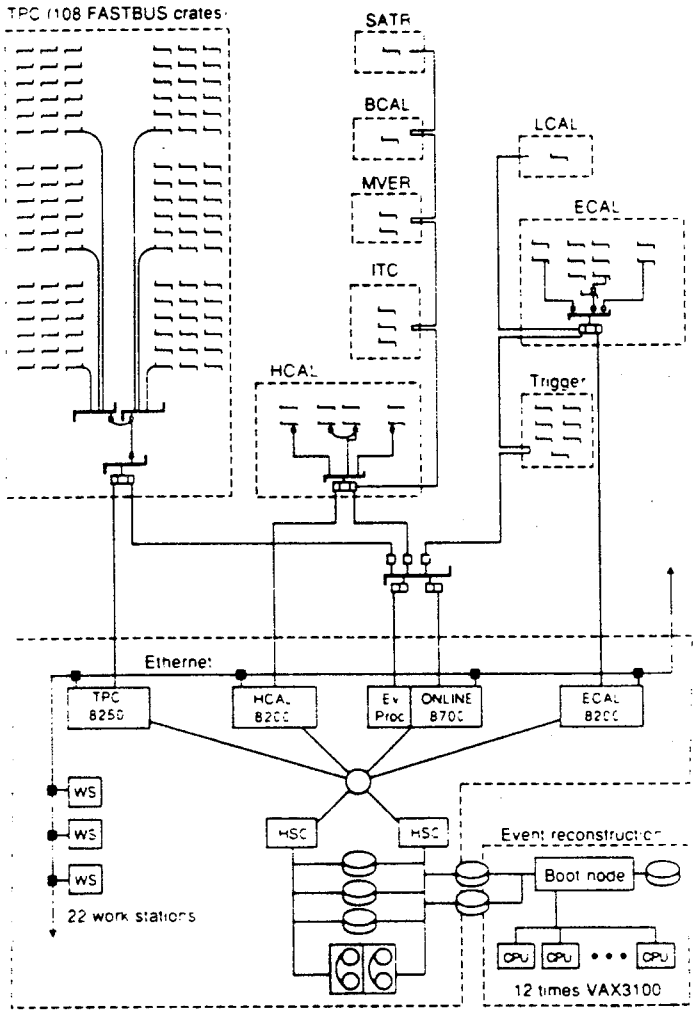

Figure 2.1: Schematic diagram of the ALEPH read out architecture.

Chapter 3

Theory

3.1 The interactions of quarks and gluons

3.1.1 Introduction

Towards the end of the 19th century, essentially two forces were known in nature. The description of the gravitational force had been comprehensively formulated by Sir Isaac Newton [7] some two centuries earlier and James Clerk Maxwell had just unified the description of electric and magnetic phenomena in his theory of electromagnetism [8, Chapter 10]. However, the discovery of radioactivity by Becquerel in 1896 and the subsequent discovery of the nucleus by Rutherford in 1911 indicated that our understanding of the fundamental forces of nature was not complete.

Further experimental developments in cosmic ray physics and in atomic spectroscopy revealed difficulties with the established theory of electromagnetism and in the early 1930s, the theory of quantum electrodynamics (QED) was developed by Dirac [9]. This theory described the interaction of charged particles in terms of a momentum transfer mediated by photons and has evolved to the present day where it stands as a model theory for the description of particles.

Following Pauli's hypothesis of the neutrino to explain the phenomena of β-decay [10], a model of the weak interaction was formulated by Fermi in 1934 [11]. The following year saw the theory of the strong nuclear force first presented in a rigorous form with Yukawa's hypothesis of the pion as the exchange boson in the interaction between neutrons and protons [12]. The subsequent discovery of the pion by Powell in 1946 [13] was an apparent vindication of the theory at that time.

At this stage the strong force was envisaged in terms of an attractive, short range potential between protons, neutrons and pions, collectively known as *hadrons*. It was attractive since it was the binding force in a nucleus, overcoming the Coulomb repulsion among the protons. That it was short range was evident

from the observation that Rutherford scattering was entirely electromagnetic down to a range of 10^{-14} m.

In the course of the 1950's, an abundance of new hadrons began to emerge from the increasingly high energy particle physics experiments which were being carried out at that time. In particular, the kaon was observed to have a high production cross-section (via the strong force) but a long lifetime (indicating weak decay). This anomalous behaviour led to the invention of the 'strangeness' quantum number, S, and the kaon was assigned a strangeness of $+1$. It was noticed that the ordering of the existing hadrons in terms of strangeness, isospin, electric charge and baryon number produced certain symmetrical patterns which hinted at sub-structure. This led Gell-Mann to suggest, in 1964, that the hadrons were composed of various combinations of three fundamental particles, the 'quarks' [14]. In Gell-Mann's picture, the *up* and *down* quarks formed an isospin doublet with $S = 0$ and the *strange* a singlet state with $S = -1$.

Baryons were considered to be composed of three quarks (with their antiparticles composed of three antiquarks) and mesons were identified with quark-antiquark pairs. This picture was very successful in explaining hadron spectra and in particular, predicted the Ω^- three years before its discovery [15].

It was observed, however, that the visible quantum numbers did not fully describe the quarks. For example, the observed properties of the Δ^{++} required that three identical up-quarks exist in a symmetrical state. Since quarks are fermions, the Pauli exclusion principle forbade this. Also, no bound states consisting of qq pairs or $qq\bar{q}$ triples were observed (such particles would have fractional electric charges).

These difficulties were removed if the quarks were endowed with *colour*. This additional quantum number, which had three possible values (conventionally called *r,g* and *b*), allowed the quarks in the Δ^{++} to have an antisymmetric wavefunction, as required by Pauli, by all having different colours. In addition, if the observable particles were required to be invariant under rotation in colour-space, then the observed hadrons had to consist only of quark-antiquark pairs (eg. $r\bar{r}$) or of triples of quarks (or antiquarks) with assignment rgb (or $\bar{r}\bar{g}\bar{b}$). This property was known as 'colour confinement' and is generally expressed as the dogma that observed final states must be colourless [16, p6].

The quark model was further developed in 1974 with the discovery of the J/ψ resonance which was interpreted as a bound state of a fourth, *charm* quark [17]. In 1977, the *bottom* quark was discovered with a mass of around 5 GeV/c^2 [18].

The concept of colour was quickly identified with the 'quark charge' in the strong interaction between quarks and so it became apparent that the strong nuclear force acting between hadrons was really just a manifestation of the more fundamental 'colour force' between their constituent quarks. In common with QED, the force was transmitted by the exchange of bosons known as *gluons*.

The description of the strong force is now known as the theory of Quantum Chromodynamics (QCD) and it is the characteristics of this theory which form the subject of this thesis.

In parallel with those developments described above, equally important discoveries were being made in the understanding of the weak interaction. This interaction takes place between all matter particles (both quarks and leptons) but is much weaker (at low energy scales) than either the electromagnetic or strong interactions. In order to avoid domination by these forces therefore, weak interaction experiments usually involve the study of leptons — particularly the neutral leptons, the neutrinos. The discovery of the *muon* in 1936 [19] demonstrated the existence of an additional charged lepton other than the electron and in 1975 a third charged lepton, the *tau* was discovered [20]. In 1968, an experiment on the AGS accelerator at Brookhaven confirmed that the electron-neutrino and muon-neutrino were distinct particles [21]. The electroweak theory was introduced in 1968 by Glashow, Salam and Weinberg [22] who suggested that the weak interaction was mediated by the exchange of charged *massive* bosons (the $W^+$and W^-). Furthermore, they anticipated that the weak interaction could be unified with the electromagnetic if the coupling of quarks and leptons to the weak bosons was equal to their coupling to the electromagnetic boson (the photon). From the electron charge (which was known) and the strength of the weak interaction (which had been measured from β-decay rates) they estimated the mass of the weak bosons to be around 80 GeV/c^2. Following the observation of neutrino scattering [23], which demonstrated the existence of a *neutral* boson in the weak interaction, they were able to add the Z^o to the picture, at a predicted mass of around 90 GeV. The predictions were confirmed by the discovery of these bosons in 1983 [24].

It became apparent that matter was organised in three 'generations', each consisting of two quarks (an *up*-type and a *down*-type) and two leptons (a charged lepton and a neutrino). These are shown diagramatically in Table 3.1.

Table 3.1: The three generations of matter particles.

Quarks	u	c	t
	d	s	b
Leptons	e	μ	τ
	ν_e	ν_μ	ν_τ

Although apparently tidy, the picture thus described is not complete. All stable matter in the universe can be constructed using the constituents of the first generation only. The existence of the additional two is therefore something

of a mystery. That there are only three light generations was confirmed in 1989 by the experiments at the LEP collider [25]. This was achieved by measurement of the line-shape of the Z^o-resonance which showed that the number of neutrino species into which the Z^o could decay was three. The existing neutrinos have very low masses (consistent with zero) and so any additional generation would have to have a neutrino member whose mass was greater than $M_z/2$. If such a generation were to exist, then by analogy with those existing, it would be conjectured that the masses of the quarks and charged leptons would be exceptionally large and beyond the range of direct experiment, at least for the immediate future. In any case, the third generation is not complete since the *top* quark has yet to be observed directly. However, its participation in a virtual state in some processes has been used to estimate its mass which is believed to be in the range 100–200 GeV/c^2 [26].

3.1.2 Characteristics of the strong force

When first formulated by Yukawa, the strong force was modelled on the already well understood electromagnetic force. QED has been very successful in describing electromagnetic phenomena and has been used to predict accurately Coulomb scattering [25, calculation of Bhabha rate in], corrections to the Lamb shift [16, p158-159] and the anomalous magnetic moment of the electron [27, p200-203]. This success gave rise to the hope that a similar theory could be applied to QCD.

QED is a *gauge* theory and the the essential requirement of such a theory is that the Lagrangian be *invariant* under a local gauge transformation. To see how this might come about in QCD, it is necessary to start by considering the QCD wave-function, $\Psi(x)$ which is a triplet of coloured quark fields (r, g and b). The globally-invariant Lagrangian is

$$\mathcal{L} = \bar{\Psi}(i\gamma^\mu \partial_\mu - m)\Psi \tag{3.1}$$

The appropriate gauge group is SU(3) and the corresponding gauge transformation is

$$\Psi \rightarrow e^{iT_a\alpha_a}\Psi \tag{3.2}$$

Where the T_a are eight 3×3 hermitian matrices which generate the SU(3) transformations and the α_a are arbitrary phase factors. The sum over a is implied.

It is important to note that the T_a form a *non-abelian* group which means that they do not necessarily commute. The commutator is in general

$$[T_a, T_b] = if_{abc}T_c \tag{3.3}$$

where f_{abc} is a real structure constant. In order to make the Lagrangian locally invariant, the covariant derivative must be

$$\partial_\mu \rightarrow D_\mu = \partial_\mu + igT_aG^a_\mu \tag{3.4}$$

where g is the colour charge and the G^a_μ are eight gauge boson fields which must transform as

$$G^a_\mu \rightarrow G^a_\mu - \frac{1}{g}\partial_\mu\alpha_a - f_{abc}\alpha_b G^c_\mu \tag{3.5}$$

where the last term arises because of the non-commutative nature of the group generators. This is important because this last term relates to *gluon-gluon* interaction and so implies that gluons carry the colour charge. This is a major departure from QED in which photons are not electrically charged.

Applying the covariant derivative of Equation 3.4 to the Lagrangian in Equation 3.1 and adding an invariant kinetic energy term yields the final QCD Lagrangian which is

$$\mathcal{L} = \bar{\Psi}(i\gamma^\mu\partial_\mu - m)\Psi - g(\bar{\Psi}\gamma^\mu T_a\Psi)G^a_\mu - \frac{1}{4}G^a_{\mu\nu}G^{\mu\nu}_a \tag{3.6}$$

This Lagrangian is locally invariant. However, the invariance will be lost if a gluon mass term is added. Therefore, in this theory, gluons are considered massless.

In summary then, the main characteristics of the QCD gauge theory are:

- There are a triplet of quark states which exhibit exact SU(3) symmetry and are identified with three colours.
- There are eight gluon states.
- The theory is non-abelian, leading to the requirement that the gluons carry the colour charge and so can interact with each other.
- In order to preserve gauge invariance, gluons are required to be massless

3.1.3 The coupling strength of the QCD interaction

The quark colour charge, g, as expressed above is the bare QCD charge. However, as in QED the vacuum surrounding a point charge is polarised by its presence and so the bare charge is shielded. This is best visualised by considering the lowest order Feynman diagram for $q\bar{q}$ pair creation, as shown in Figure 3.2. In terms of the Feynman diagrams for the process, the shielding is portrayed as the effect of 'loop' diagrams, an example of which is shown in

Figure 3.3. However, the individual terms in a series of such diagrams are not finite.

This phenomenon is common to QED as well as QCD and leads to a need to *renormalise* the coupling constant to reflect the effective charge. This involves replacing the bare charge with an effective charge which produces a convergent term in the higher order contribution. In one such scheme

$$g(\mu) = g_0 + g_0^3 (b \ln \frac{M}{\mu} + c) + \ldots \tag{3.7}$$

where $g(\mu)$ is the effective charge expressed in terms of the bare charge g_0 and the energy scale, μ, at which the effective charge is to be calculated. M is a cut-off, introduced to cope with the problem that the loop integral must be summed over all momenta and which led to the divergent term.

Differentiating $g(\mu)$ in Equation 3.7 with respect to μ reveals the variation of g with μ, namely;

$$\mu \frac{\partial g(\mu)}{\partial \mu} = -g^3(\mu) b + \mathcal{O}\{g^5(\mu)\} + \ldots \tag{3.8}$$

The coefficients b and c in Equation 3.7 depend on the diagrams present in the renormalisation and so are different for QED and QCD since QCD includes gluon interaction diagrams. In fact, $b_{QED} < 0$, indicating that the QED effective charge increases with μ. Thus the electromagnetic coupling between charged particles becomes stronger as they are brought closer together (a higher scale, μ, corresponds to a closer approach). On the other hand, $b_{QCD} > 0$ and so the quark charge, and hence coupling strength, is *reduced* at close range. This property of the QCD field is known as *asymptotic freedom* and is consistent with two important aspects of quark behaviour which are observed. Namely;

- In deep inelastic scattering experiments (at high Q^2), the quarks appear to be free, point-like particles.
- Quarks have never been observed as free particles in nature ($Q^2 = 0$) and appear to be confined within hadrons.

The differential Equation 3.8 for $g(\mu)$ may be solved in terms of a fixed scale, μ_0. Defining

$$\alpha_s(\mu) = \frac{g^2(\mu)}{4\pi} \tag{3.9}$$

and

$$\Lambda^2_{QCD} = \mu_0^2 \exp\left\{-\frac{4\pi}{b_0 \alpha_s(\mu_0)}\right\} \qquad \left(\text{where } b_0 = \frac{(33 - 2n_f)}{3}\right) \tag{3.10}$$

where n_f is the number of active flavours (5 at LEP), then gives an expression for the running coupling constant of QCD, $\alpha_s(\mu)$ in terms of the scale factor, μ and the *fundamental parameter* of QCD, Λ_{QCD}.

$$\alpha_s(\mu) = \frac{12\pi}{(33 - 2n_f)\ln(\mu^2/\Lambda^2_{QCD})} \tag{3.11}$$

Λ_{QCD} is a measure of the energy scale at which strong interactions become appreciable. Significantly above this energy, quarks and gluons (collectively known as *partons*) behave as free particles. Below it, they are bound together in hadrons. If Λ_{QCD} is known, then at any energy scale, μ, the coupling constant can be determined and the cross-section for any QCD process can be calculated to leading order.

3.1.4 Higher order effects in perturbative QCD

The above discussion led to an expression for the coupling constant to lowest order. In order to verify this model, it is necessary to test its predictions of physical parameters with those obtained experimentally. When this is done, it is found that the agreement is not exact. This is a consequence of considering only the lowest order term in Equation 3.8 and is represented, physically, by considering only the lowest order process as shown in Figure 3.2.

To improve the approximation, it is necessary to include the contributions to the amplitude from diagrams such as that in Figure 3.4 which shows real gluon emission. This encounters infrared and collinear divergences arising from the fact that there is no lower limit to the energy which a gluon may have, nor to the angle at which it might be emitted. This is evident in the cross-section for the process $e^+e^- \rightarrow q\bar{q}g$ given by [16, p239].

$$\frac{d\sigma}{dx_q dx_{\bar{q}}} = \text{Constant} \times \frac{x_q^2 + x_{\bar{q}}^2}{(1 - x_q)(1 - x_{\bar{q}})} \tag{3.12}$$

where x_q and $x_{\bar{q}}$ are the energy fraction of the quark and anti-quark. The fraction is related to the emission angle by (for massless quarks)

$$1 - x_q = \frac{2}{Q^2} E_{\bar{q}} E_g (1 - \cos\theta_{\bar{q}g}) \tag{3.13}$$

and so it can be seen that if the gluon momentum goes to zero (hence $x_q \rightarrow 1$) or if $\theta_{\bar{q}g} \rightarrow 0$ then the cross-section becomes infinite. The infrared and collinear divergences can be dealt with, however. The second order corrections

(Figure 3.3) also contain singularities but it can be shown [28] that the terms containing them are of opposite sign to those of lowest order. The consequence is that when the infrared and collinear corrections are added to the second order loop corrections, the divergent terms cancel and the resulting correction is finite.

The conclusion is that it is possible to obtain a finite expression for any given physical parameter which includes the effect of higher order processes. The corrections which originate from these processes become smaller for higher orders and so a series of successive terms converges.

In this work, the $\mathcal{O}(\alpha_s^2)$ expression [29, p377] for α_s is used, namely

$$\alpha_s(\mu, \Lambda) = \frac{1}{b_0 \ln(\mu^2/\Lambda^2)} - \frac{b_1 \ln[(\ln(\mu^2/\Lambda^2)]}{[b_0 \ln(\mu^2/\Lambda^2)]^2} \tag{3.14}$$

with

$$b_o = \frac{33 - 2n_f}{12\pi} \qquad b_1 = \frac{153 - 19n_f}{24\pi^2} \tag{3.15}$$

and where Λ_{QCD} has been abbreviated to Λ for brevity.

3.1.5 Perturbative QCD: calculations and predictions

When the available energy in a process is increased, the strength of the interaction between quarks is reduced. In the limit of infinite energy (corresponding to zero range) the force would vanish and quarks would act as free particles. At energy scales which are large compared to Λ_{QCD}, quarks are approaching asymptotic freedom and perturbative QCD is a valid method of describing their behaviour.

In this region, cross-sections for processes such as gluon-splitting, quark pair-creation and gluon radiation from quarks can (in principle) be calculated. In practice, these calculations have been performed exactly up to second order. The proliferation of diagrams for even third order is so great that a reliable calculation has not yet been carried out. However, there are many computer programs available which can calculate cross-sections for physical processes to various orders and in general, two approaches are taken [30, 31].

- **Matrix Element (ME) method.** This method employs exact second order calculations to determine the relative fraction of two, three and four parton final states. Parton momentum distributions are varied according to user-defined parameters which are tuned to fit the data. The advantage of this method is that Λ_{QCD} enters explicitly into the calculation and so a comparison with experimental results gives a direct measurement of this quantity.

- **Parton Shower (PS) method.** In this method, the primary cross-section is calculated exactly to lowest order (a 2 or 3 parton final state). The quarks thus produced are far from the mass shell. They lose energy by gluon (and occasionally, photon) bremsstrahlung. This is allowed to proceed until some 'evolution variable' has reached a cut-off point below which no further radiation is permitted (this is to limit infrared and collinear gluon emission) [1].

  The parton shower is thus calculated to a much higher order than in the matrix element case by taking only an approximation to each higher order term. This approximation is based on the leading-logarithm in each term and so this method is commonly described as the 'leading-log approximation' (LLA). Since the contribution from each term is not exact, the use of this method to measure either Λ_{QCD} or α_s leads to a large theoretical uncertainty.

Having obtained the best calculation for the parton final states, the next task is to describe how the coloured partons *hadronise* and form colourless hadrons. This process of hadronisation cannot be described by perturbative QCD since at this stage, the parton energy scale is approaching Λ_{QCD} and so they cannot be considered as being free. Consequently, this process is dealt with according to various phenomenological models. Two models which have been employed in this analysis are;

- **Cluster Hadronisation.** In this model, any gluons existing in the parton final state are converted into $q\bar{q}$ pairs on the mass shell. Final state quarks are then clustered with the new quarks to form colourless hadrons which (if unstable) decay to provide the observed particle spectrum. This method essentially models the perturbative QCD process $e^+e^- \rightarrow q\bar{q}$ at an energy equal to the virtual gluon mass and so is calculable with only two parameters (Λ_{QCD} and Q_0, the energy).

- **String Hadronisation.** This model interprets the gluon field between quarks as a colour flux 'string' connecting the quarks. Radiated gluons are interpreted as momentum concentrations (kinks) in the string which has an energy density of the order of 1 Gev/fm. As they diverge in space, the potential energy in the string increases until enough energy is present to produce a $q\bar{q}$ or di-quark pair and so 'break' the string. At the point of hadronisation, there is insufficient energy in any string to produce new quarks and so the quarks are left bound in hadrons.

[1] The choice of evolution variable depends on the particular program being used — for example in HERWIG 4.1 it is the product of energy and emission angle, $E\theta$.

The overall process consisting of the parton shower, hadronisation and subsequent decay is called *fragmentation*. This process is shown schematically in Figure 3.1 which portrays the initial $q\bar{q}$ pair radiating hard gluons (calculable to 2nd order). The partons then radiate in a parton shower until the mass-shell is reached (higher order effects). The mass-shell partons then convert to hadrons (hadronisation). Finally, any short-lived hadrons (containing b and c quarks) decay to the particles which are detected.

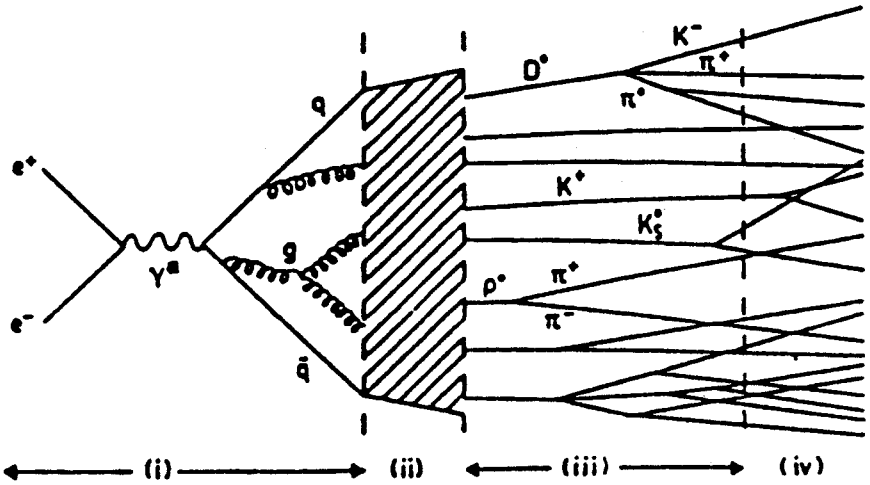

Figure 3.1: Evolution of the initial partonic state to observed final state particles.

3.1.6 QCD and event characteristics

The cross-section for gluon emission from quarks is peaked strongly in the collinear region as has been explained above. In addition, due to the initial quark energy being, in this analysis, much greater than its rest mass, the subsequent hadronisation and decay take place in a boosted reference frame.

This leads to the final observed particles appearing in two collimated 'jets'. It is reasonable to assume that the jet directions are close to the original quark directions. However, events with three or more clear jets are frequently observed. This phenomenon is explained by asserting that the additional jets are due to the fragmentation of hard radiated gluons and immediately suggests a technique for determining α_s since the cross-section for gluon radiation from a quark depends on α_s. There are some difficulties, however.

- Soft or collinear gluons may not be discernible (after fragmentation) from the jet of their parent quark.
- Random effects in hadronisation or systematic effects in detection may artificially split a jet.

- Jets have to be defined by some algorithm and the jet multiplicity in any given event will depend on the resolution parameter used in this algorithm.

Any metric which is intended for use in measuring α_s has therefore to be insensitive to such effects.

In summary then, it can be said that the interaction between quarks can be described by a non-abelian gauge theory in which the force is mediated by eight coloured gluons. Characteristics of this force are that partons are asymptotically free at high energy scales, and that the colour charge is never visible (colour-confinement). The strength of the force can be represented by a coupling constant but this constant must be renormalised to take account of infinities which arise due to shielding of the bare charge by virtual gluons. Renormalisation allows calculations to a limited order to give finite results for the cross-sections for physical processes. This however, leads to the need to introduce a scale factor on which the results depend. Translation from parton final states obtained from such calculations to observed hadrons is achieved by invoking phenomenological fragmentation models which are tuned to represent the data. At the energies employed in this analysis, the resulting particle topology is dominated by collimated jets.

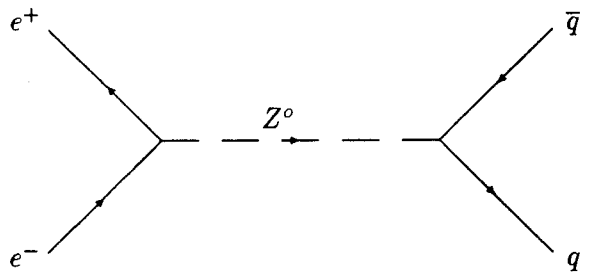

Figure 3.2: Lowest order Feynman diagram for the process $e^+e^- \rightarrow q\bar{q}$.

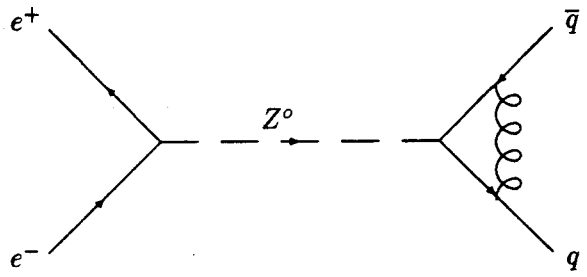

Figure 3.3: Example of a virtual loop correction to the cross-section for $e^+e^- \rightarrow q\bar{q}$.

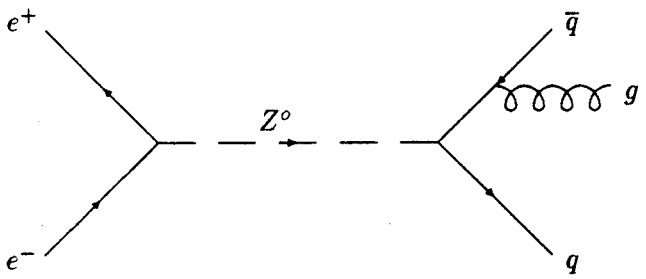

Figure 3.4: Example of real gluon emission, contributing in 1st order to the process $e^+e^- \rightarrow q\bar{q}g$.

3.2 Experimental tests of QCD

In order to measure Λ_{QCD} and therefore α_s, it is necessary to be able to calculate a physical observable which fulfils several criteria.

- Hard gluon radiation leading to a 3-jet event depends on α_s and so the observable must be sensitive to the rate of 3-jet events.
- An accurate approximation must be obtainable by going to a limited order only in perturbation theory. This means that the calculation should be insensitive to higher order terms.
- It must be insensitive to soft or collinear gluon emission.
- It must be insensitive to hadronisation effects or systematic errors in detection.

3.2.1 Observables sensitive to α_s.

There have been several quantities suggested to meet these criteria and so provide a measure of the strength of the QCD interaction. Although this thesis is concerned only with the $EEC(\chi)$ function and its asymmetry, it is useful to review some of the other metrics and discuss their properties. Note that all values for α_s quoted below were taken from [32].

- **Thrust** is defined as the sum of particle momenta along a so-called 'thrust axis' which is chosen to maximise the sum. A two-jet event has a high value of thrust while a hard gluon, by shifting momentum off the thrust axis, will reduce it. The thrust distribution in a large sample of events should therefore reflect the gluon emission cross-section. Thrust, however, is sensitive to broadening of the jet profile which reduces its value. Thus it is somewhat sensitive to fragmentation and higher order effects. The sensitivity of thrust to hadronisation has been estimated at about 3% compared with 1.6% for the $EEC(\chi)$ which has been found in this work. The uncertainty due to the effects of higher order terms is also large (around 16%) and an overall uncertainty in α_s of at best 10% has been anticipated using this method [29, p395]. In practice, ALEPH has measured α_s from thrust to be

$$\alpha_s(M_z^2) = 0.119 \pm 0.014$$

- **Oblateness** is a related quantity to thrust. Firstly, the thrust axis is determined. Then, a major axis is found which maximises the momentum

in a direction orthogonal to the thrust axis. Finally, the minor axis is defined as being orthogonal to both the thrust and major axes. The oblateness of the event is essentially the difference between the energy flow along the major axis and that along the minor axis. Clearly a two-jet event should have little energy flowing along either the minor or major axis and so should have a vanishingly small oblateness. Kinematically, a three-jet event is required to be largely planar so the energy flow along the major axis should be large while that in the minor axis direction should be small. A four-jet event may well have a substantial energy flow along the major axis but in this case, the minor axis could be expected to carry some energy flow as well and so the overall oblateness will be reduced. Consequently, oblateness is a quantity which is maximal for three-jet events and which is small for both two-jet events and events containing higher order effects. ALEPH has found α_s from a study of the oblateness distribution and has obtained

$$\alpha_s(M_z^2) = 0.186 \pm 0.036$$

- The differential two-jet rate is the distribution of the jet-finder resolution parameter ($Y_{lim}{}^2$) which marks the transition between two jets and three jets in a each event. A clear three-jet event will need a large value of Y_{lim} to be classified as two-jet and so the sensitivity to the three-jet rate is revealed in the Y_{lim} distribution. This variable was found to be fairly robust with respect to the effects of fragmentation and higher orders and a value of

$$\alpha_s(M_z^2) = 0.121 \pm 0.008$$

was obtained in ALEPH.

3.2.2 The energy-energy correlation function.

The energy-energy correlation function, $EEC(\chi)$ has been suggested [33] as an observable which meets these criteria. The function and its asymmetry, $AEEC(\chi)$ are defined in this analysis as

$$EEC(\chi) = \frac{1}{N} \sum_{events}^{N} \sum_{i,j} \frac{E_i E_j}{E_{vis}^2} \delta(\cos\chi - \cos\chi_{ij}) \qquad (3.16)$$

[2]In order to form a jet, closely grouped tracks are combined and their *scaled invariant mass-squared* is calculated. Y_{lim} is the maximum scaled invariant mass-squared which a group of tracks may have if that group is to be classified as a single jet.

and

$$AEEC(\chi) = EEC(180^o - \chi) - EEC(\chi) \tag{3.17}$$

where χ_{ij} is the angle between the pair of particles i and j in an event and N is the number of events. E_i is the energy of the ith particle and E_{vis} is the total energy of all particles used in the analysis in each event. The $EEC(\chi)$ graph is plotted in terms of $\cos\chi$ for ease of comparison with the theoretical predictions which have been presented in this form.

From Equation 3.16 it will be noticed that the $EEC(\chi)$ is strongly weighted by particle energy. Two energetic particles will make a large contribution to the bin at $\cos\chi$, where χ is the angle between them. The asymmetry function is simply the difference between the right and left-hand sides of the $EEC(\chi)$ graph. By considering Figure 3.5 it can be seen that a 2-jet event consists of two highly-collimated streams of particles moving in opposite directions. They contribute to two regions only;

- the region corresponding to $\chi = 0^o$ from self-correlations and from correlations within a jet and,
- the region corresponding to $\chi = 180^o$ from correlations between jets (which are back-to-back).

The central region will be depleted since few highly energetic particles are found at large ($\sim 60^o$) angles to the jet axes in such events. On the other hand, as Figure 3.6 shows, while a 3-jet event will contribute to the 0^o region for the same reasons as before, there will be a relative depletion at the 180^o region because no jets are back-to-back. In addition, the central region (corresponding to $\chi = 60^o - 120^o$) will be enhanced by inter-jet correlations.

Consequently, the $EEC(\chi)$ function has a form typical of that shown in Figure 3.7 consisting of two peaks at $\cos\chi = 1$ and -1 and a minimum around $\cos\chi = 0$. The height of the minimum is a measure of the number of 3-jet events in the sample and so is sensitive to α_s. Since the function is energy-weighted, it is insensitive to soft gluon emission. It is also insensitive to collinear gluons since if a track splits into two parallel tracks the same correlations are produced. Finally, it does not rely on a jet-finding algorithm and so has no dependence on any external parameters.

An example of the $AEEC(\chi)$ is shown in Figure 3.8. Symmetrical 3-jet events (where the inter-jet angles are all 120^o) are quite rare. It is more common for the three jets to have different energies and therefore for the set of angles between them to consist of one less than 90^o and two greater than 90^o. This leads to more contributions to the $-1 < \cos\chi < 0$ part of the $EEC(\chi)$ graph than to the $0 < \cos\chi < 1$ region and so an asymmetry arises. Contributions from 2-jet events are highly symmetrical and so cancel in the asymmetry. Consequently, any asymmetry near the $\cos\chi = 1$ region as shown in Figure 3.8 is due to hard gluon emission.

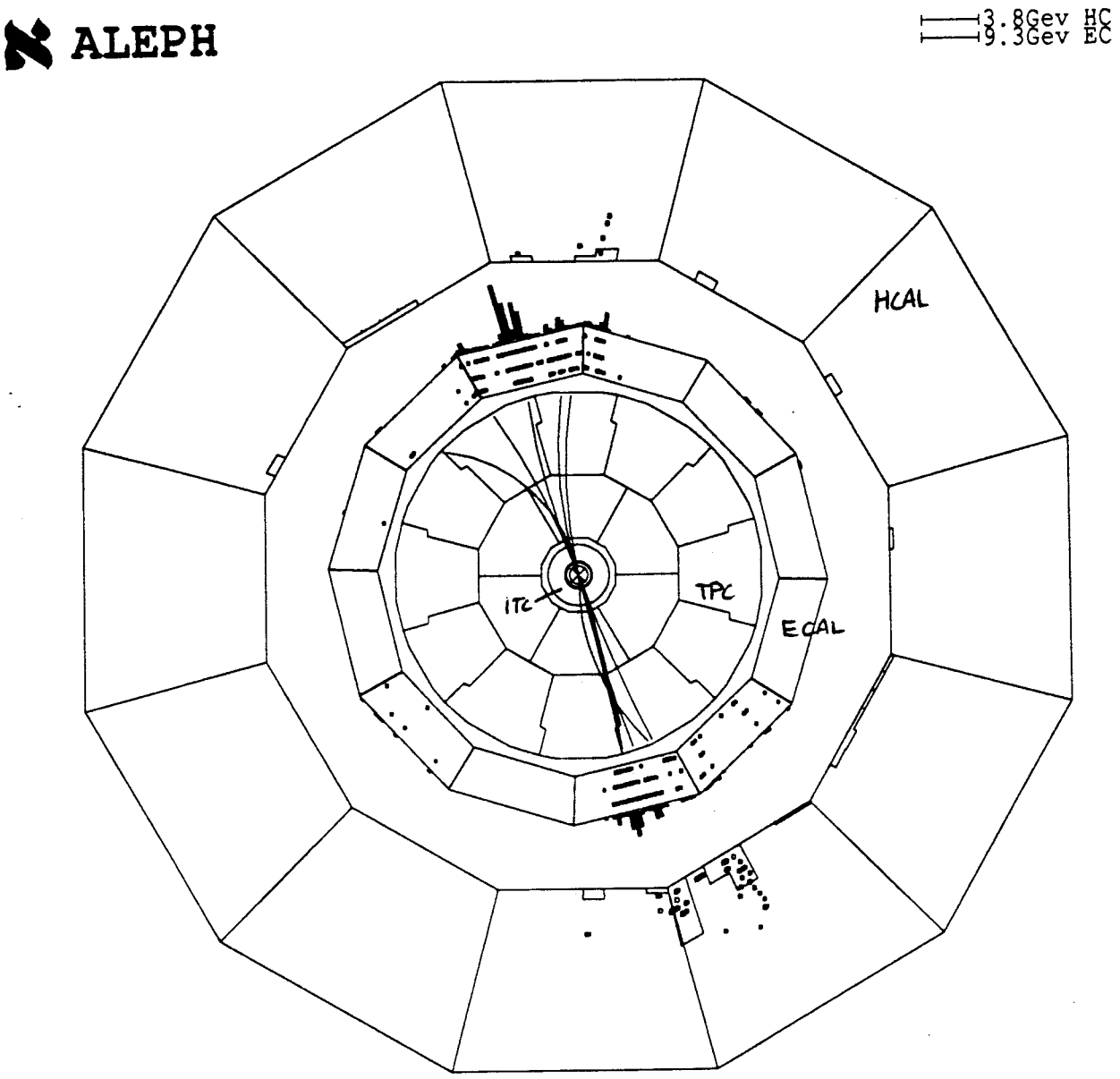

Figure 3.5: Two-jet hadronic event in the ALEPH detector

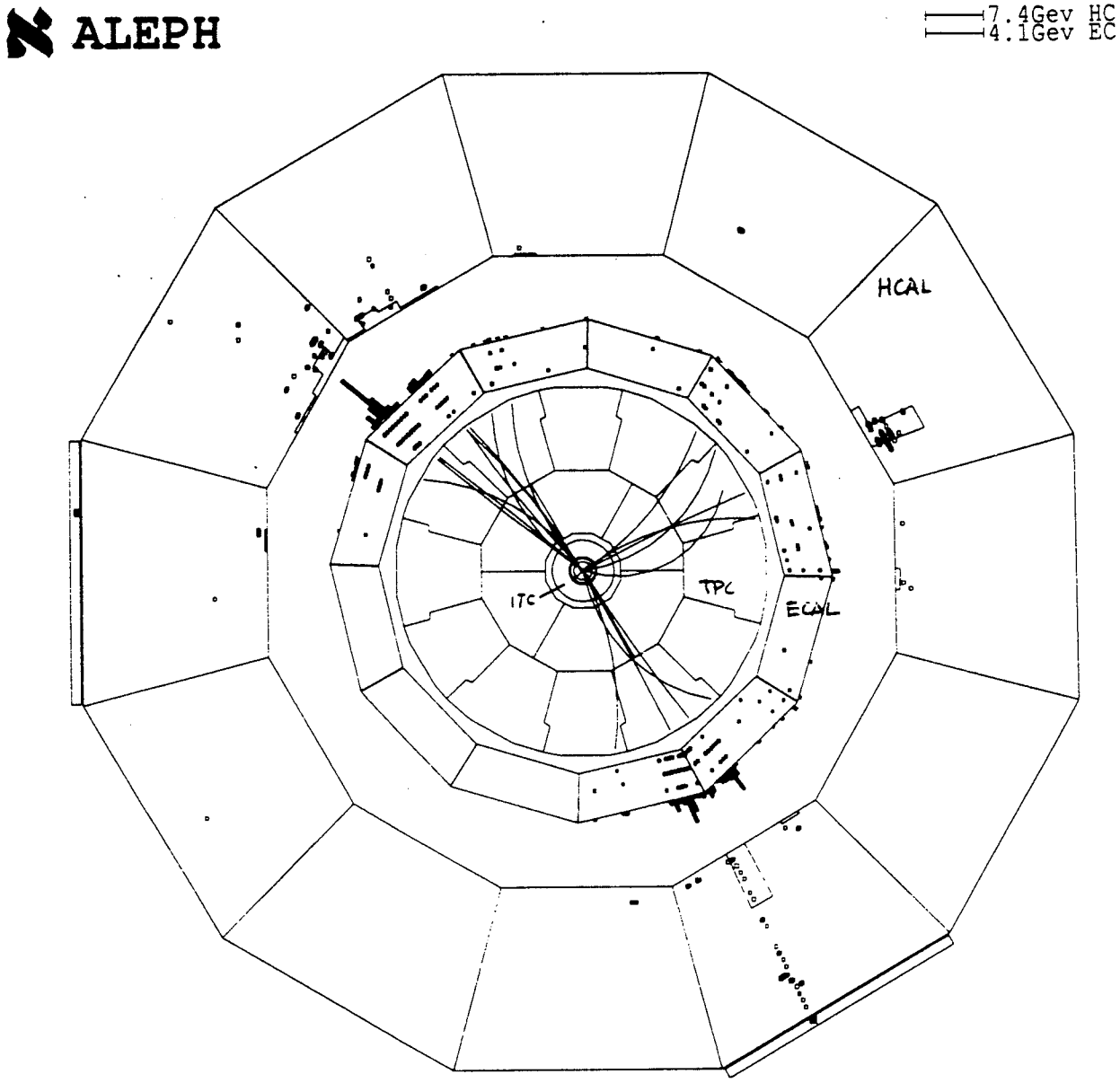

Figure 3.6: Three-jet hadronic event in the ALEPH detector.

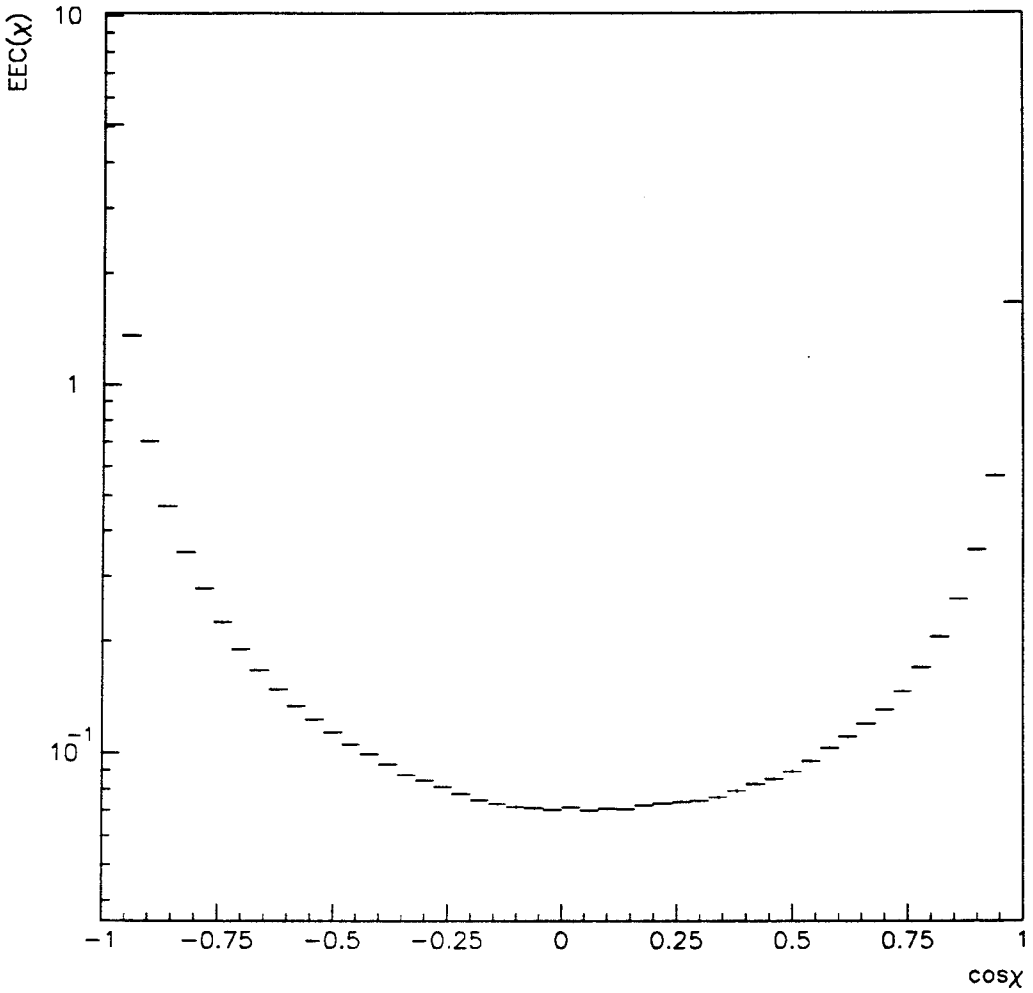

Figure 3.7: $EEC(\chi)$ obtained from the full hadronic data sample in ALEPH.

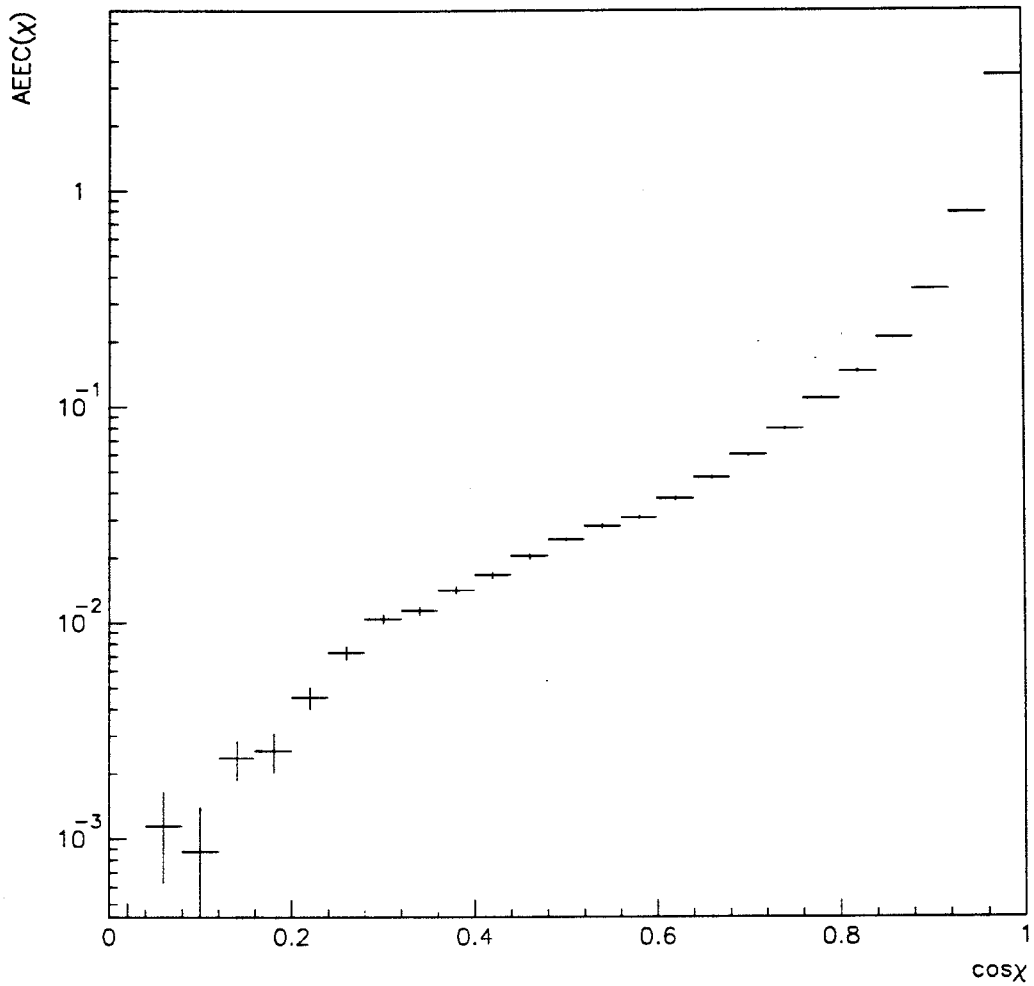

Figure 3.8: Asymmetry in the $EEC(\chi)$ obtained from the full hadronic data sample in ALEPH.

Chapter 4

Experimental analysis.

4.1 Event selection and characteristics of the data.

As has been described in Chapter 1, the ALEPH detector produces electrical signals in response to the interaction of particles with the detector material. As with all complex electronic devices, noise and interference are present and are superimposed on the signals originating from true particle interactions. In addition, radiation from natural sources (terrestrial or cosmic) also causes the detector to produce signals. The detector trigger system acts to eliminate events originating from external sources or from noise by insisting on coincidence with beam crossings in the collider. However, there remain several other types of events of which only one type is of interest in this work. Before describing how events of interest are selected, it is useful to review the different sources of events and describe briefly their characteristics.

1. **Beam-gas interactions.** Although the beam pipe is evacuated and is at a high vacuum, some residual gas remains. If a nucleus of a gas atom is struck by a beam particle, the electron will interact with a nuclear quark and can eject it from the nucleus. The subsequent quark fragmentation and the disintegration of the nucleus produces a flux of particles which can trigger the detector. Such events can occur anywhere in the beam pipe and so the particle tracks seldom extrapolate back through the interaction vertex.

2. **Off-axis particles.** Electromagnetic repulsion among the like-signed particles within a bunch leads to broadening of the bunch during its orbit. While the focussing magnets to a large extent correct this, particles still 'peel off' the bunch in the course of its many circuits of the machine. Such particles, on collision with the beam-pipe wall, will produce an event similar to a beam-gas interaction as described above.

3. **Collimator muons.** In an effort to reduce the flux of off-axis particles, the beam passes between collimators fitted in the beam-pipe a few metres before the detector. Off-axis particles collide with the collimator and initiate reactions whose products are absorbed by concrete shielding between the collimators and the detector. However, if a muon is produced in the collimator interaction, it will generally be able to penetrate the shielding, enter the detector and trigger it. Such events are easily identified by a penetrating track running nearly parallel to the beam-axis.

4. **Bhabha events.** When an e^+e^- pair is observed in the final state, it is impossible to say whether this has come from decay of the Z^o or simply from the electromagnetic interaction of two beam particles. Statistically, the decay process has an angular cross-section which is peaked at right-angles to the beam. The electromagnetic process, however, is peaked strongly at shallow angles close to the beam line. The rate of Bhabha events can be compared with theoretical calculations and used to measure the collider luminosity.

5. **Two-photon events.** In keeping with the uncertainty principle, it is possible for a charged particle to emit a virtual photon which it later re-absorbs. Therefore, all beam particles are surrounded by a 'halo' of virtual photons. Since at the interaction point the opposing electron and positron beams are squeezed and passed through each other, it is common for an e^+e^- pair to approach each other to within the range of the virtual photon halo. In such circumstances it is possible for the virtual photons to interact (by virtual fermion exchange) and produce a real $f\bar{f}$ pair which may fragment and decay. Since the two photons do not have balanced momenta (as do beam particles), the event is usually boosted in one direction and therefore in the laboratory reference frame there is apparently much 'missing momentum'. The cross-section for this process is peaked at low energies and so typically produces a low number of charged tracks. Although of no interest in this work, this phenomenon has importance as a test of a variety of theories and has been studied for this purpose.

6. **Genuine Z^o decays.** The Z^o decays to a pair of fermions which may be leptons or quarks. Each possible decay mode produces a different signature in the detector, as follows:

   - Decays to neutral leptons (neutrinos) are generally unrecorded since the neutrinos are weakly interacting only. One exception occurs when either the positron or electron radiates a photon before annihilation. The event then consists of a single photon and can be used as a signature for $Z^o \rightarrow \nu\bar{\nu}$.

- Decays to e^+e^- pairs produce two back-to-back charged tracks of around 45 GeV in the TPC and two connected energy deposits in the ECAL. This type of event is indistinguishable from a Bhabha event.
- Decays to $\mu^+\mu^-$ are similar in appearance to e^+e^- production except that the more penetrating muons deposit energy in the HCAL and go on to produce hits in the muon chambers.
- Decays to $\tau^+\tau^-$ are followed rapidly by the decay of both taus. Tau-decay is to leptons or hadrons and each tau produces either 1, 3 or (occasionally) 5 charged tracks. The charged track multiplicity in tau events can therefore reach 10, although it rarely exceeds 6. It is possible, therefore, for some $\tau^+\tau^-$ events to resemble low-multiplicity hadronic events.
- The decay of a Z° into a $q\bar{q}$ pair leads ubiquitously to the production of hadron jets. At the energy scale of the ALEPH experiment, the strong coupling constant, α_s is diminished with respect to lower energy experiments and so hard gluon emission is suppressed. Thus, only a few (2, 3 or 4) hard partons typically are produced. The hard partons emit soft gluons in order to reach the mass-shell. Since soft gluon emission is suppressed at large angles, the *parton shower* surrounding a hard primary parton is clustered around its initial direction. Once on the mass-shell, the partons then hadronise into a large number of hadronic final states. Many of these decay rapidly and the observed spectrum of meta-stable[1] charged particles usually numbers around 20. Although hadronisation and decay produces some additional smearing, the final-state particles are often still clustered around the original parton directions and so hadronic events observed in the ALEPH experiment are characterised by a few collimated hadron jets. Multiplicity and event shape are to some extent related to quark flavour but the correlation is weak and sophisticated analysis is required in any attempt to identify flavour.

In order to ensure that all events of interest are detected and recorded, the detector data acquisition system is programmed to trigger on any meaningful events occurring simultaneously with a beam crossing. In order not to reject prematurely real events (and especially, to be receptive to unexpected events indicating new physics), the cuts employed by the trigger system are very relaxed and amount essentially to recording any event containing at least one

[1]This means stable enough to traverse the detector without decaying and includes, *inter alia*, pions, kaons and muons.

charged track or calorimeter object. This means that examples of all the events described above are routinely recorded.

It was necessary, therefore, to employ a series of software cuts to select useful hadronic events. These cuts were applied for two reasons: firstly, it was necessary to reject those events which did not originate from $q\bar{q}$ production. Secondly, all events which were to be used had to be of good quality — that is, all tracks had to be well-determined. The cuts employed in this analysis were as follows:

- **Cuts on charged tracks:**

  1. Track momentum was required to be greater than 200 MeV/c. This was a quality cut. Particles with a momentum lower than this produced a track with a large tangential component and the momentum determination had a high relative error.
  2. Polar angle of the track was required to be greater than 20^o. Tracks at a lower angle than this did not traverse a sufficiently large number of TPC pad rows before leaving the TPC and so the momentum was poorly determined.
  3. Number of TPC space-points used in the reconstruction of the track had to be at least 4. This cut removed spurious tracks resulting from random correlations where the track-fitting algorithm accidentally assigned a track to a group of random points.
  4. Tracks had to originate within a cylinder of radius 3 cm and length 10 cm which was concentric and aligned symmetrically with the detector. This removed spurious tracks produced by secondary reactions in the detector material and so improved event quality. Also, tracks from beam-gas interactions (which could occur anywhere) would seldom project through this region and so were likely to be rejected. This effect is shown in Figure 4.1 where the 'D_0' distribution is shown for simulated $q\bar{q}$ events and for simulated $\gamma\gamma$ events. The $\gamma\gamma$ events have a much wider distribution and were preferentially rejected by this cut.

- **Cuts on events:** Considering only those tracks which passed the above cuts, the following criteria were applied to the event as a whole.

  1. The number of charged tracks had to be at least 5. This cut removed most leptonic Z^o decays, although some high-multiplicity $\tau^+\tau^-$ events did escape this cut. Figure 4.2 shows the distributions in the number of tracks for simulated $q\bar{q}$, $\gamma\gamma$ and $\tau^+\tau^-$ events.

2. The total charged energy was required to exceed 15 GeV. This cut removed many $\gamma\gamma$ events which tended to have a low energy. Figure 4.3 shows the comparison between simulated $\gamma\gamma$ and $q\bar{q}$ events and displays the discrimination which this cut imposed on the sample.
3. The axes of all jets in the event had to have a polar angle of greater than 35^o. This was a quality cut which was intended to ensure that the whole event was well-contained in the detector. The reason for this concern was that if a jet had a sufficiently low polar angle, there would be some tracks which would be at a still lower angle. These tracks might then have been victims of the low-angle track cut described above or may even have escaped detection entirely. This effect is shown graphically in Figure 4.4 which illustrates how the mean charged track multiplicity per jet varies with the polar angle of the jet. Obviously, the mean number of tracks in a sample of jets should be unconnected with the polar angle, but as Figure 4.4 shows, for jet axis angles below about 35^o, the mean multiplicity is depressed indicating that some tracks are lost in such jets.

Table 4.1: Effects of cuts on various samples of simulated events.

Sample type	$q\bar{q}$	$\tau^+\tau^-$	$\gamma\gamma$
No. in sample	149000	45000	20000
< 5 tracks	2805	42051	17610
< 15 GeV	5356	41	2389
No. passed	140839	2903	1
Acceptance	94.5%	—	—
Rejection	—	93.5%	99.995%

The effects of these cuts were studied by passing samples of simulated events through them. After applying the cuts described above to the tracks in each event, the event itself was subjected to the cuts on charged track multiplicity and charged energy successively. Two-photon, $\tau^+\tau^-$ and $q\bar{q}$ samples were used in this test. The results are shown in Table 4.1.

The imposition of these cuts on the data sample can therefore be expected to discriminate powerfully against events originating from non-$q\bar{q}$ processes while selecting $q\bar{q}$ events with a high efficiency. The only significant contamination of the sample comes from $\tau^+\tau^-$ production. Since the rate of Z^o decaying to $\tau^+\tau^-$ is less than 5% of that to $q\bar{q}$ [25], the τ–contamination in the final sample

is estimated to be 0.34%. The energy-energy correlation function for the $\tau^+\tau^-$ sample is shown in Figure 4.5. The contributions are predominantly in the regions near $\cos\chi = 1$ or -1 which reflects the two-jet appearance of $\tau^+\tau^-$ events. In the important central region, the contributions are extremely small and therefore it is concluded that the effect of τ–contamination on measurements of the $EEC(\chi)$ function are entirely negligible.

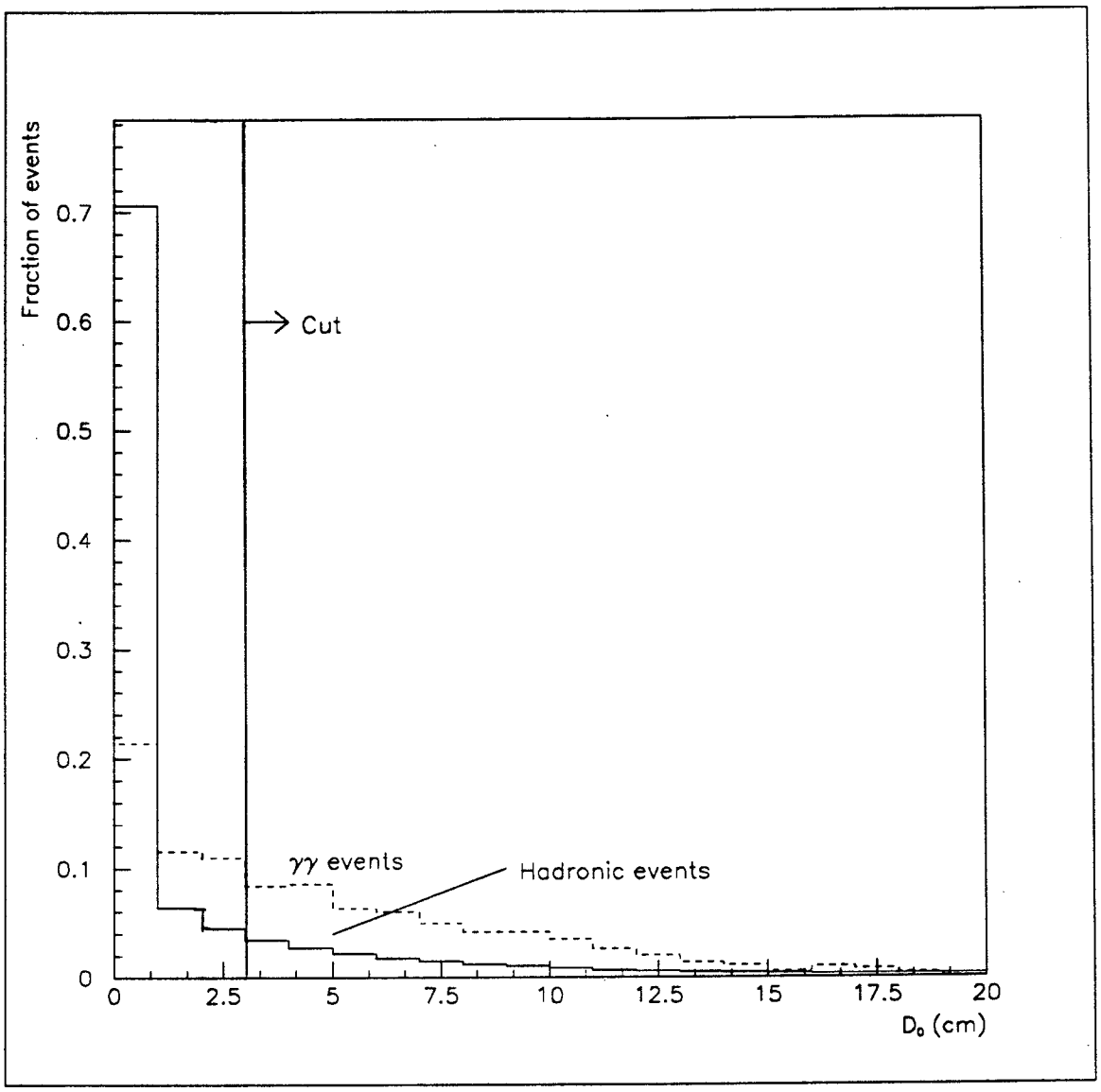

Figure 4.1: D_0 cut for $q\bar{q}$ and $\gamma\gamma$ events.

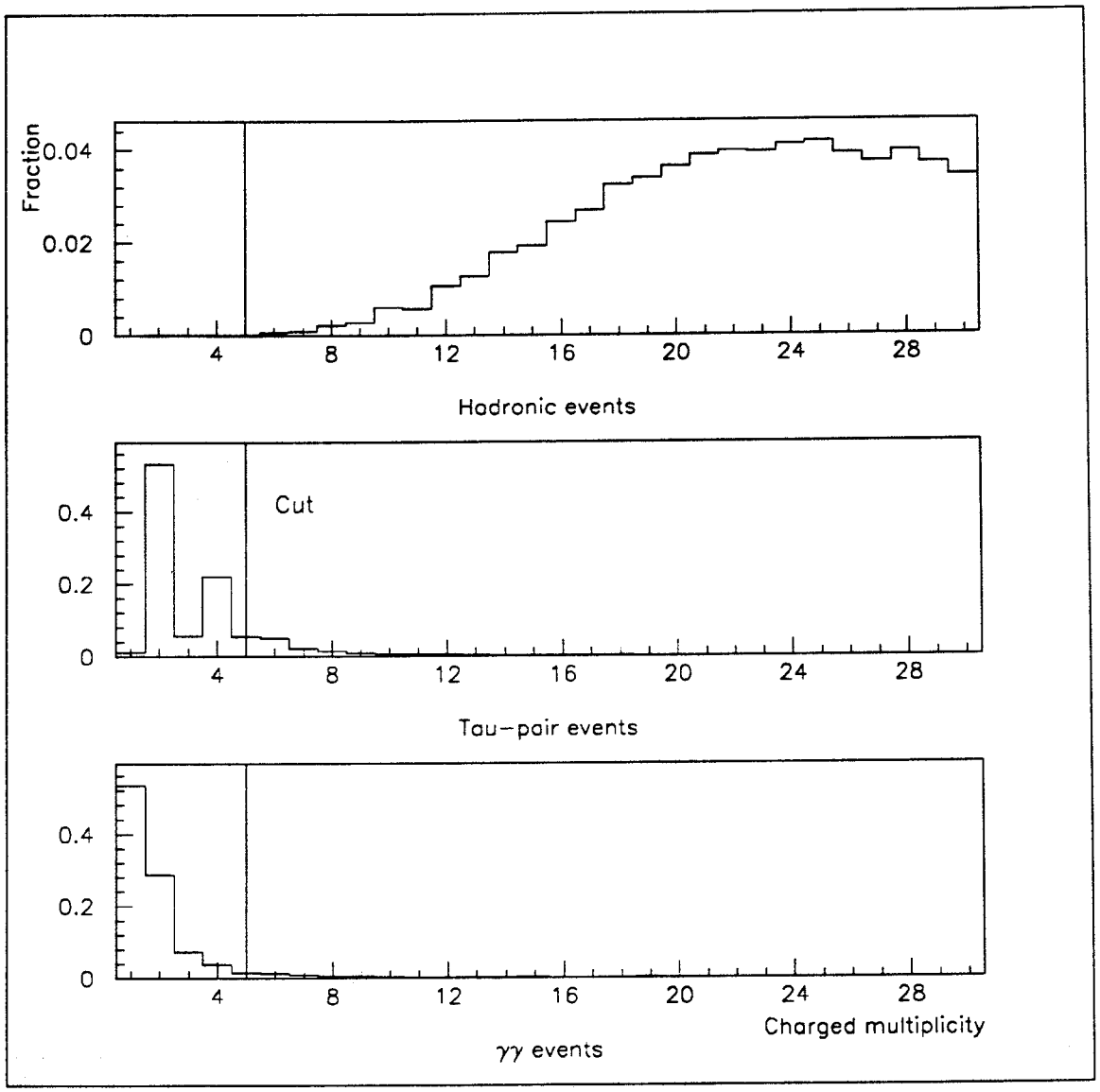

Figure 4.2: Number of tracks per event for $q\bar{q}$, $\tau^+\tau^-$ and $\gamma\gamma$.

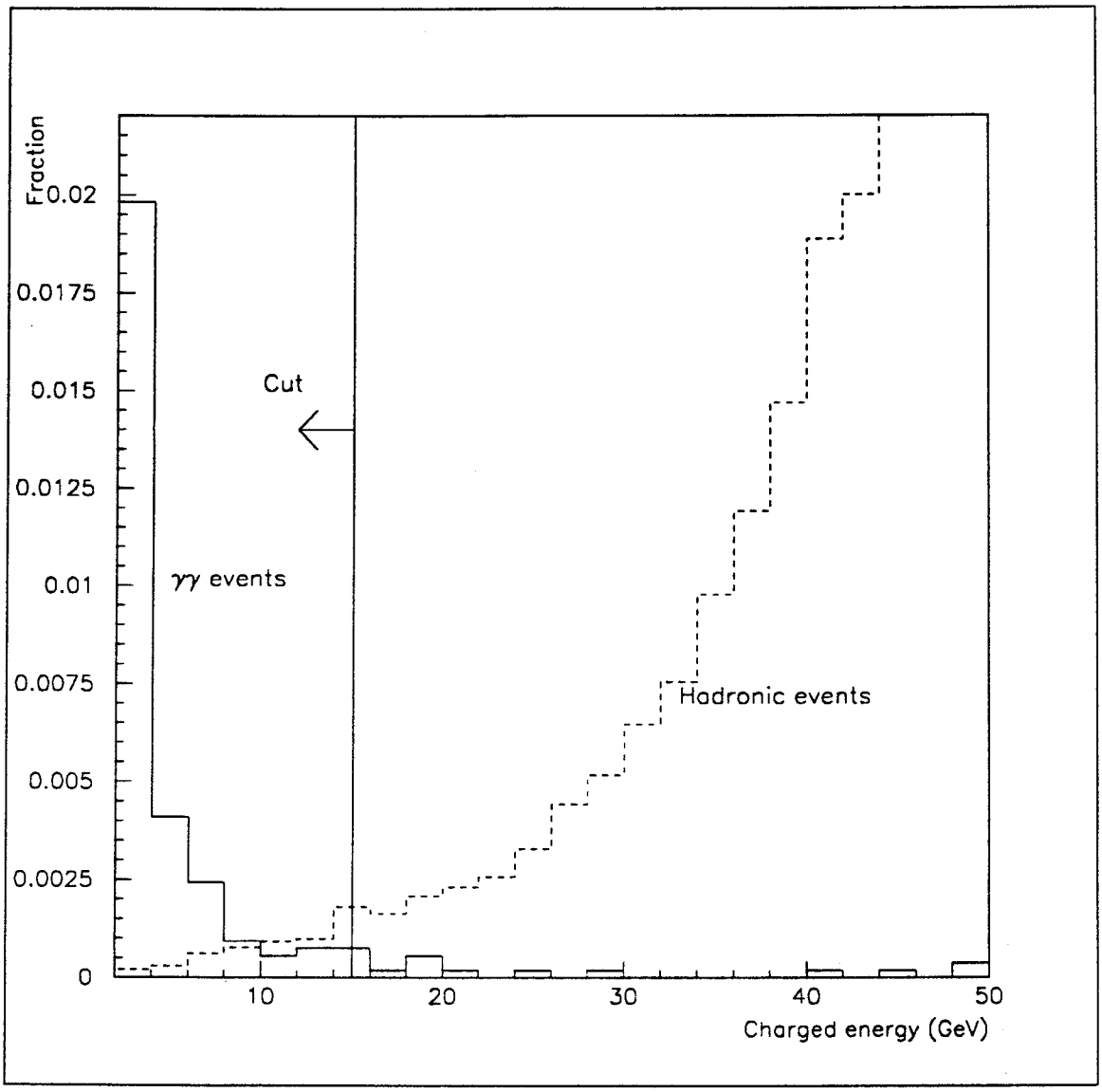

Figure 4.3: Energy distribution per event for $q\bar{q}$ and $\gamma\gamma$.

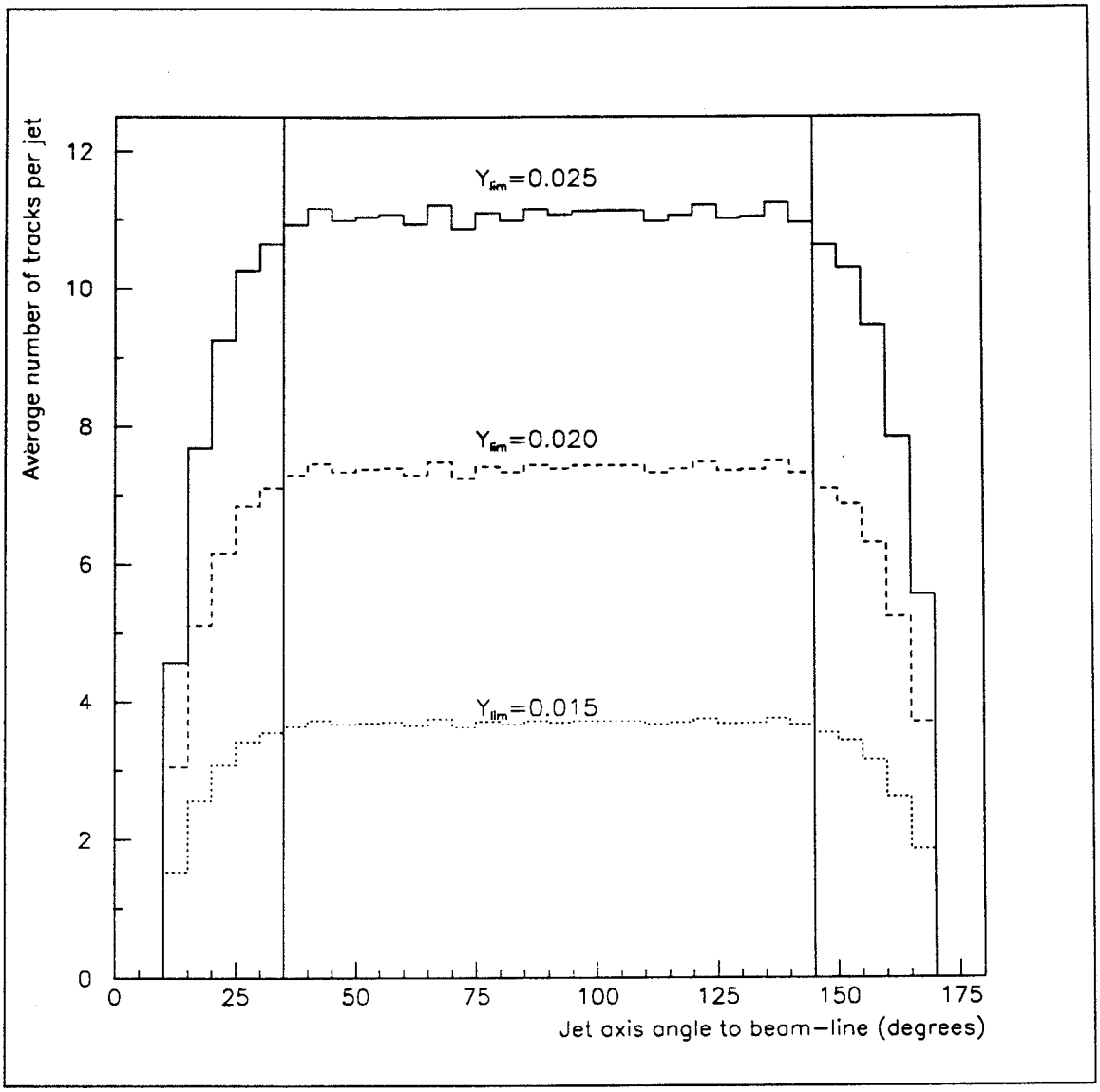

Figure 4.4: Mean number of tracks per jet as a function of jet-axis angle at various values of y_{lim}.

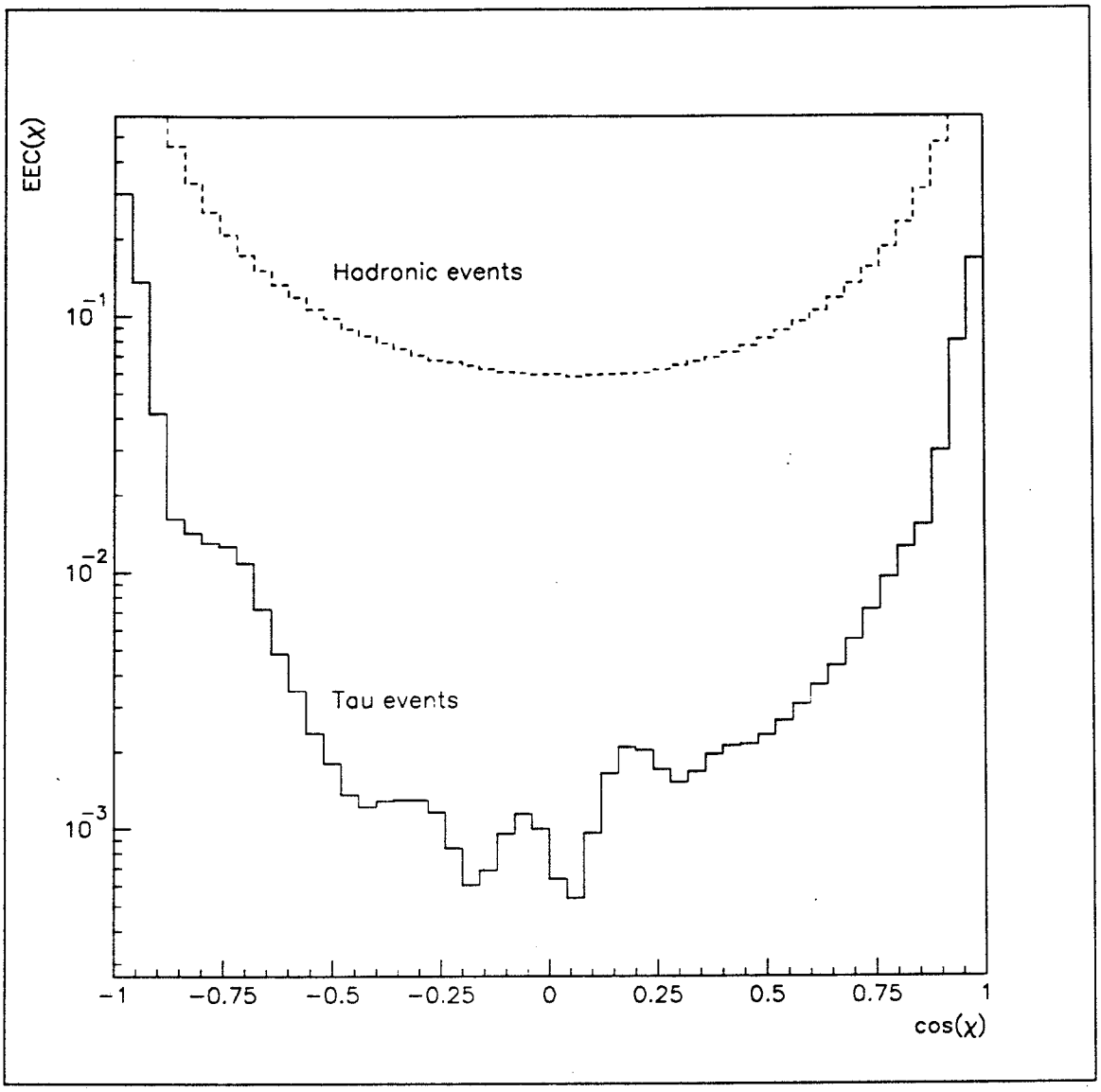

Figure 4.5: $EEC(\chi)$ function for a sample of $\tau^+\tau^-$ events compared to $q\bar{q}$ events.

4.2 α_s from the $EEC(\chi)$ and $AEEC(\chi)$.

The $EEC(\chi)$ function, which has been described in Section 3.2, can be predicted by perturbative QCD to $\mathcal{O}(\alpha_s^2)$ and this has been done by several theoretical groups [29, p401-405] [34, 35, 36]. Comparison of the theoretical predictions with the data enabled a value of α_s to be extracted using the following procedure:

1. The $EEC(\chi)$ function was obtained for the selected data.
2. The function was then corrected for the effects of the detector, initial-state radiation of photons and hadronisation.
3. For each theoretical prescription, the $EEC(\chi)$ function was calculated at a range of values of α_s and a histogram was obtained. The theoretical histogram was then compared with that originating from the corrected data by calculating the χ^2/dof between the two histograms. This was also done for the $AEEC(\chi)$.
4. A parabola was then fitted to the set of points $(\alpha_s, \chi^2/dof)$ thus obtained. The local minimum was then determined to find the best-fit value of α_s.

This process is described in some detail in the following sections.

4.2.1 Correction of the data.

The ALEPH detector is of finite resolution in its momentum measurement. Thus, the precise 4-vector of all particles cannot be obtained. In practice, 'smearing' of the tracks takes place due to the error in the reported 4-vector. In addition, the detector is not 100% hermetic and insensitive regions exist where tracks cannot be measured. Finally, the track reconstruction algorithm, on occasion, creates spurious tracks by fitting a helix to a set of randomly occurring space-points in the TPC. These effects combine to produce a systematic error in any quantity measured and so have to be corrected for.

Another significant source of error is initial state radiation. In this process, one of the initial e^+e^-pair emits a photon prior to the interaction and so loses some momentum. The Z^o is not, therefore, produced at rest in the lab frame but is boosted. If the photon has an energy of even a few GeV then the boost can create fake correlations which affect the $EEC(\chi)$ function.

A third source of error comes from the fact that the theoretical calculations of the $EEC(\chi)$ function are obtained by modelling the parton evolution as the parent quarks emit gluons and so are valid only at the parton level. The detector, on the other hand, observes particles in the final state and at large distances from the interaction region. The partonic state on which the theoretical estimate is based has to undergo several changes which collectively are known as *fragmentation* before arriving at the the state which is seen by the detector.

To correct for these effects, the following procedure was adopted;

1. A large sample (100,000) of $q\bar{q}$ events was generated using the JETSET 7.3 program and the quarks were allowed to radiate gluons in a parton shower until the mass-shell was reached. However, initial state radiation of photons was prohibited. At this point the evolution of the event was stopped and the partons were not permitted to hadronise. The $EEC(\chi)$ graph was obtained for this sample (labelled $\mathrm{MC}^{\mathrm{truth}}$).

2. A different sample (149,000) of $q\bar{q}$ events was generated using the same generator and physical parameters. In this sample, hadronisation (according to the Lund string model [30]) and decay were allowed to proceed. Also, initial-state radiation of photons was allowed to take place with the appropriate cross-section. Furthermore, the events obtained were subjected to the detector simulation routine, GALEPH, which converted the kinematical information in the event record into the simulated signals which would have been obtained had these events actually occurred within ALEPH. The record of these signals subsequently was processed through the event reconstruction program, JULIA, and thus returned to a form identical to that of real events. This sample was labelled $\mathrm{MC}^{\mathrm{reco}}$ and its $EEC(\chi)$ graph was determined.

3. In the two histograms, the corresponding bins were compared and the correction factor, c_i was formed for each bin, i, where;

$$c_i = \frac{\mathrm{MC}_i^{\mathrm{truth}}}{\mathrm{MC}_i^{\mathrm{reco}}} \tag{4.1}$$

4. The correction factor was then multiplied with the corresponding bin in the raw data histogram, to obtain the corrected data histogram. Thus;

$$c_i \times \mathrm{DATA}_i^{\mathrm{raw}} = \mathrm{DATA}_i^{\mathrm{corr}} \tag{4.2}$$

Figure 4.6 shows the set of correction factors obtained for JETSET 7.3. The extent to which this correction is successful can be judged by considering Figure 4.7 which shows how the $EEC(\chi)$ histogram obtained directly from the data (with no correction) compares with that from the fully reconstructed Monte-Carlo sample. Agreement is good, reflecting the general success of the simulation in representing the data. Quantitatively, in the important central region (where 3-jet contributions dominate) the difference between the two varies between 1 and 2%. This difference was used to estimate the residual error in the $EEC(\chi)$ due to hadronisation, initial-state radiation and detector effects combined.

4.2.2 Comparison of data with theoretical predictions.

Four separate theoretical prescriptions were employed to predict the form of the $EEC(\chi)$ function. These are referred to hereafter as KN [29], AB [34], RSE [35] and FK [36]. In the case of AB, RSE and FK, the $EEC(\chi)$ function is defined by

$$EEC(\chi) = \frac{\alpha_s}{\pi} \cdot A(\cos\chi) \cdot \left[1 + \frac{\alpha_s}{\pi} \cdot B(\cos\chi)\right] \tag{4.3}$$

where the coefficients A and B represent the first- and second-order contributions, respectively, to the $EEC(\chi)$. The energy dependence of the $EEC(\chi)$ is contained in the running of α_s. The different groups differ mainly in the method of summing the contributions to the second-order coefficient. In the case of KN, the second-order term is enhanced by an additional term involving the first-order coefficient

$$EEC(\chi) = \frac{\alpha_s}{2\pi} \cdot A(\cos\chi) + \left(\frac{\alpha_s}{\pi}\right)^2 \cdot \left[A(\cos\chi) 2\pi b_0 \ln\left(\frac{\mu^2}{Q^2}\right) + B(\cos\chi)\right] \tag{4.4}$$

This equation is important because it contains an explicit dependence on μ, the QCD scale. Since this is the main area of theoretical uncertainty in QCD, Equation 4.4 is useful in quantifying this error.

The $EEC(\chi)$ graph was calculated using each of the four models at eleven values of α_s in the range 0.06 — 0.16 inclusive. Each graph obtained was compared with that for the corrected data and the χ^2/dof was determined according to the formula

$$\chi^2/dof = \frac{1}{n-1} \cdot \sum_i^n \left(\frac{x_i^{\text{data}} - x_i^{\text{theory}}}{\Delta x_i}\right)^2 \tag{4.5}$$

where x_i is the content of the ith bin in the data or theory histogram and Δx_i is the overall error in that bin which was calculated as described in Section 4.2.3.

The number of bins used in the fit did not extend over the full range of the $EEC(\chi)$ for two main reasons; firstly, the regions of the $EEC(\chi)$ near -1.0 and 1.0 (corresponding to angles 180^o and 0^o) are dominated by 2-jet events — the main contribution from 3-jet events is in the central region. Secondly, the theoretical predictions are most accurate in the central region and run into singularities near $\cos\chi = -1.0$ and 1.0. By restricting the fit to a limited region in the centre of the $EEC(\chi)$ graph, it was ensured that the metric was at its most sensitive to the quantity to be determined and that the predictions were at their most accurate. Consequently, the range chosen for the $EEC(\chi)$ was $-0.5 < \cos\chi < 0.5$.

An identical procedure was followed for the $AEEC(\chi)$ which was determined directly from the $EEC(\chi)$ in both the measured data and the theoretical prediction. Here the range was allowed to extend further into the low angle region ($\cos\chi \sim 1.0$) which, although dominated by the 2-jet contribution, still contains significant contributions from soft gluons. The 2-jet contribution is highly symmetrical and cancels in the $AEEC(\chi)$ hence the soft gluon contribution can be observed. The asymmetry in the $EEC(\chi)$ vanishes near $\cos\chi = 0$ where the curve flattens out and so the $AEEC(\chi)$ graph is dominated by statistical fluctuations. The range adopted for the fit to the $AEEC(\chi)$ was therefore $0.3 < \cos\chi < 0.9$.

4.2.3 Sources of error.

Four sources of experimental error were identified and quantified in this analysis. Each error was calculated for each histogram bin and then combined in quadrature with the others. The four error sources considered were;

1. **Hadronisation.** As described in Section 4.2.1, the effects of hadronisation, initial-state radiation and detector smearing were corrected by Monte-Carlo simulation. However, this correction was not perfect and a residual error remained. This was estimated by considering the difference between the entry in each bin of the uncorrected data histogram and the corresponding entry in the fully simulated histogram. The fractional error in the ith bin of the corrected data histogram was then taken to be;

$$\Delta_i^{\text{had}} = \left| \frac{x_i^{\text{data}} - x_i^{\text{MC}}}{x_i^{\text{data}}} \right| \tag{4.6}$$

   where x_i is the entry in the ith bin of the histogram.

2. **Statistical.** This error accounted for the statistical fluctuations in the number and size of the components making up the entry in each histogram bin and was taken to be;

$$\Delta_i^{\text{stat}} = \sqrt{\sum_j^n w_{ij}^2} \tag{4.7}$$

   where w_{ij} is the jth component of the entry in the ith bin.

3. **Theoretical.** In order to obtain the coefficients in the analytical form of the $EEC(\chi)$, large integrals have to be solved which yield only to numerical techniques. This introduces a source of error which most groups have published. The typical values are around 1% in coefficient A and 4%

in coefficient B (of Equation 4.3). This error was estimated by measuring the fluctuation produced in the bins in the theoretical $EEC(\chi)$ graph at the best fit value of α_s as the coefficients A and B were moved from their central values to their extreme limits.

4. **Systematic.** The $EEC(\chi)$ function, as its name implies, is a quantity derived from the energy of the particles in the event being analysed. This energy was calculated from the momentum of the particle which was, in turn, measured by the TPC. The TPC momentum measurement had a small error associated with it which was dependent on the particle momentum. In addition to this, the energy calculation assumes that the particle is a pion (the most common hadron produced in these events). Thus, if the particle is *not* a pion, the energy calculated will be in error. Assuming that the particle population at this energy is approximately 70% pion, 15% kaon and 15% proton, the mean systematic error due to this assumption of the pion mass was estimated to be $\pm$ 0.18 GeV. Combining this with the error in the momentum measurement, the final systematic error in energy measurement was taken as;

$$\frac{\Delta E}{E} = \sqrt{\left(\frac{0.18}{E}\right)^2 + (1.2 \times 10^{-3} \cdot P)^2} \tag{4.8}$$

where E and P are the energy and momentum of the particle.

The systematic error in each particle energy propagates through the calculation of the $EEC(\chi)$ histogram and since each component of each bin is

$$W_{ab} = \frac{E_a \cdot E_b}{E_{sum}^2} \tag{4.9}$$

the error in any component is

$$\frac{\Delta W}{W} = \sqrt{\left(\frac{\Delta E_a}{E_a}\right)^2 + \left(\frac{\Delta E_b}{E_b}\right)^2 + 4\left(\frac{\Delta E_{sum}}{E_{sum}}\right)^2} \tag{4.10}$$

This error is sensitive to the size of the sample and can be shown by a simple statistical argument to vary as $1/\sqrt{N}$, where N is the number of events in the sample.

The average error from each of these sources in the bins corresponding to the range $-1.0 < \cos\chi < 1.0$ was found to be

Hadronisation	1.6%
Statistical	0.5%
Theoretical	2.1%
Systematic	3.8%
Overall	4.7%

A further source of error due to the uncertainty in the QCD scale is discussed in the next section.

4.2.4 Determination of α_s.

Having thus obtained a value for the χ^2/dof between the theory and the data at different values of α_s, a graph was plotted of χ^2/dof against α_s and a parabola was fitted [37, p122] through the data points. From the coefficients of the resulting quadratic equation, the position of the minimum, (x_{min}, y_{min}) was calculated. The line, $y = y_{min} + 1$ was then drawn and the points of intersection of the line with the parabola were projected onto the x-axis to yield the upper and lower bounds on α_s. The value of α_s was therefore determined to be the average of these two bounds and the error to be half the difference.

Table 4.2: $\alpha_s(M_z^2)$ determined from fitting the $EEC(\chi)$ and $AEEC(\chi)$ to different theoretical predictions. The first error is from the fit and the second is due to the scale uncertainty.

Theory	α_s from $EEC(\chi)$	α_s from $AEEC(\chi)$
KN	$0.132 \pm 0.005 \,^{+0.012}_{-0.009}$	$0.109 \pm 0.006 \,^{+0.011}_{-0.007}$
AB	$0.130 \pm 0.009 \,^{+0.012}_{-0.009}$	$0.113 \pm 0.011 \,^{+0.011}_{-0.007}$
RSE	$0.138 \pm 0.006 \,^{+0.013}_{-0.009}$	$0.097 \pm 0.005 \,^{+0.010}_{-0.006}$
FK	$0.134 \pm 0.005 \,^{+0.012}_{-0.009}$	$0.117 \pm 0.007 \,^{+0.012}_{-0.008}$

Figure 4.8 shows the parabolic fit for the $EEC(\chi)$ to the prediction of KN. This process was repeated for the other theoretical models and for the $AEEC(\chi)$. The error arising from the uncertainty in the QCD scale was determined by varying the scale in Equation 4.4 between $\mu = M_z/2$ and $\mu = 2M_z$. This led to a shift in the value of α_s obtained which was taken as the error due to scale uncertainty. The results obtained are shown in Table 4.2.

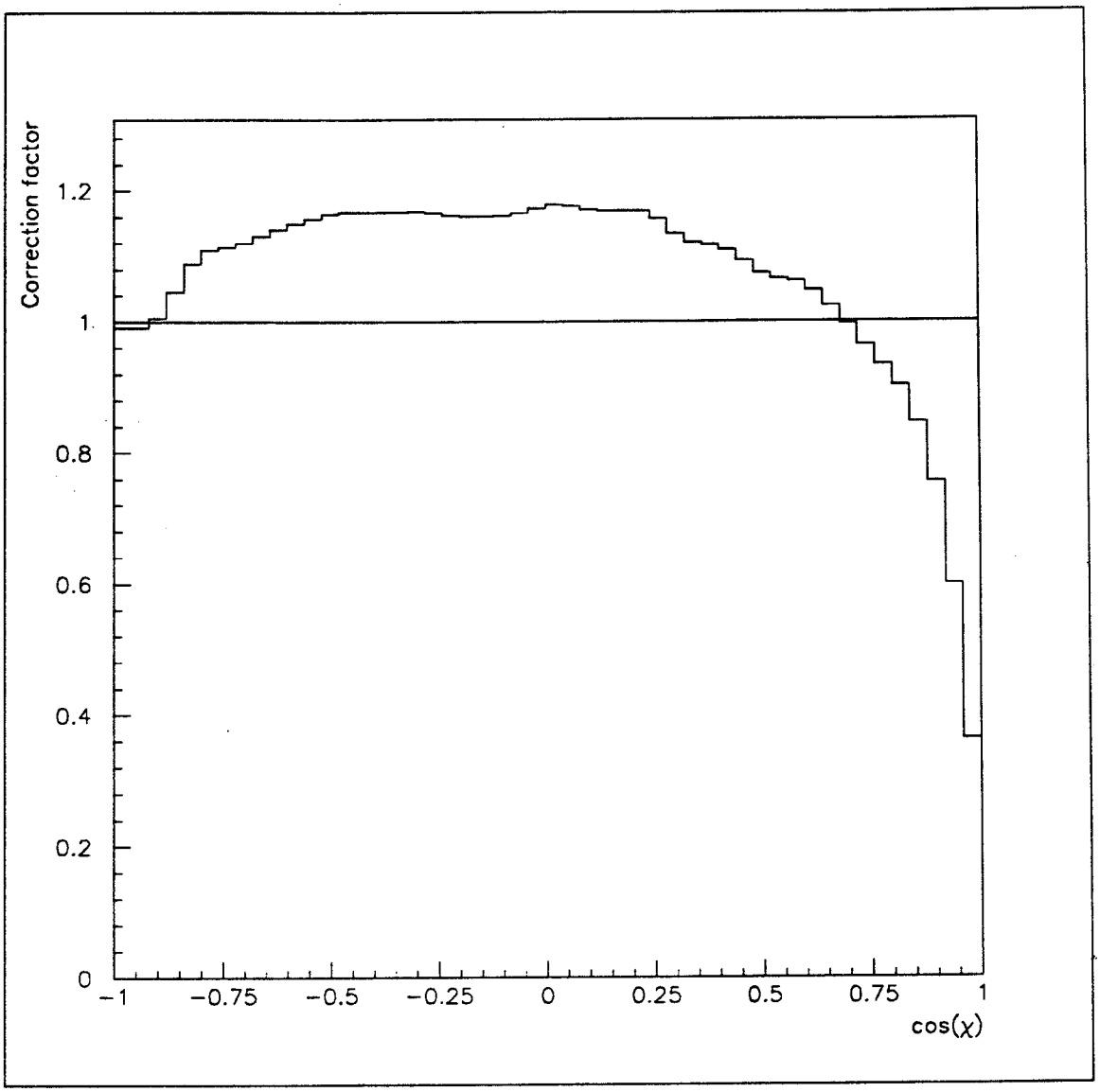

Figure 4.6: Correction factors obtained for the $EEC(\chi)$ function.

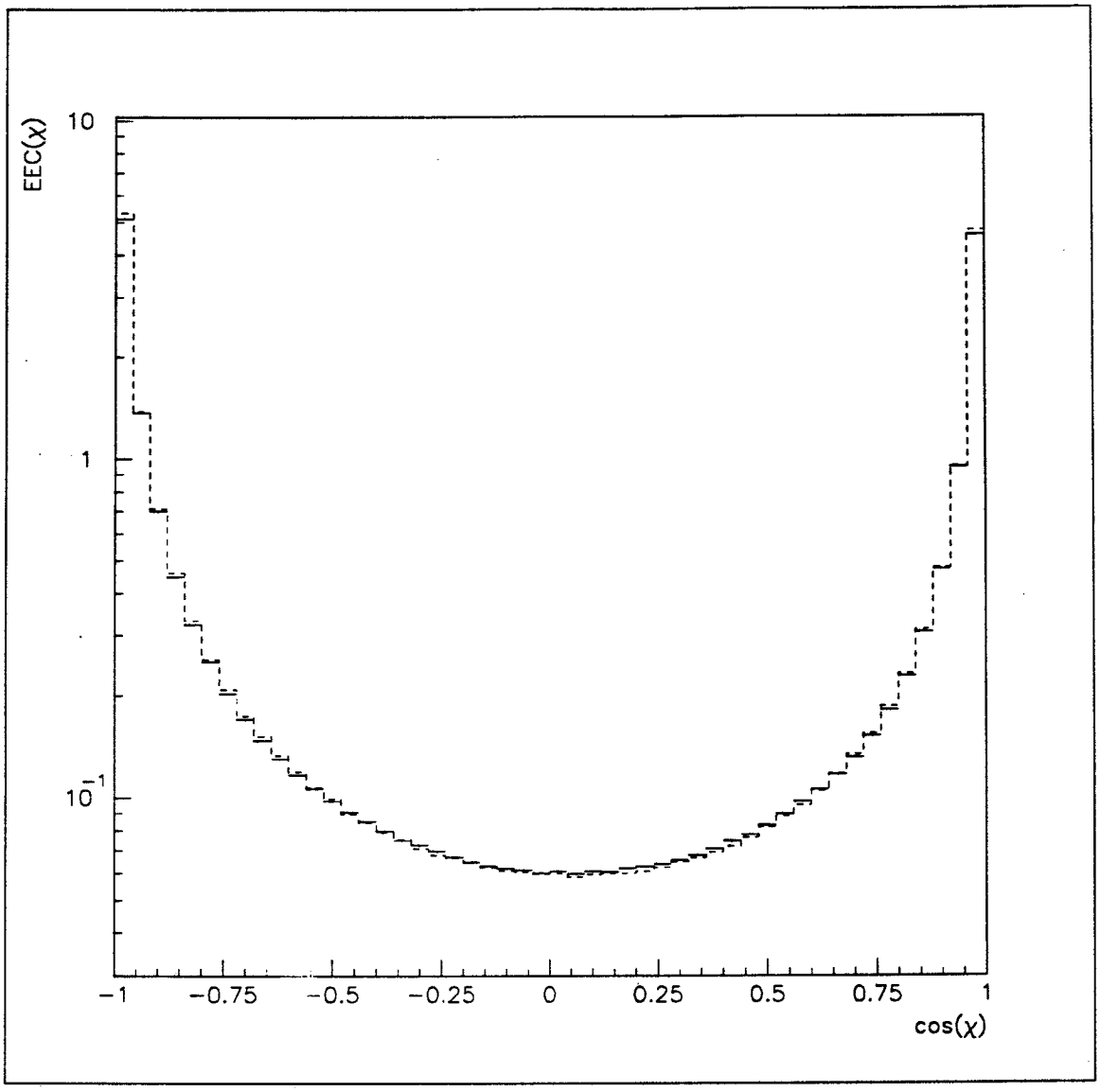

Figure 4.7: Comparison of the $EEC(\chi)$ function between uncorrected data and the fully reconstructed simulation.

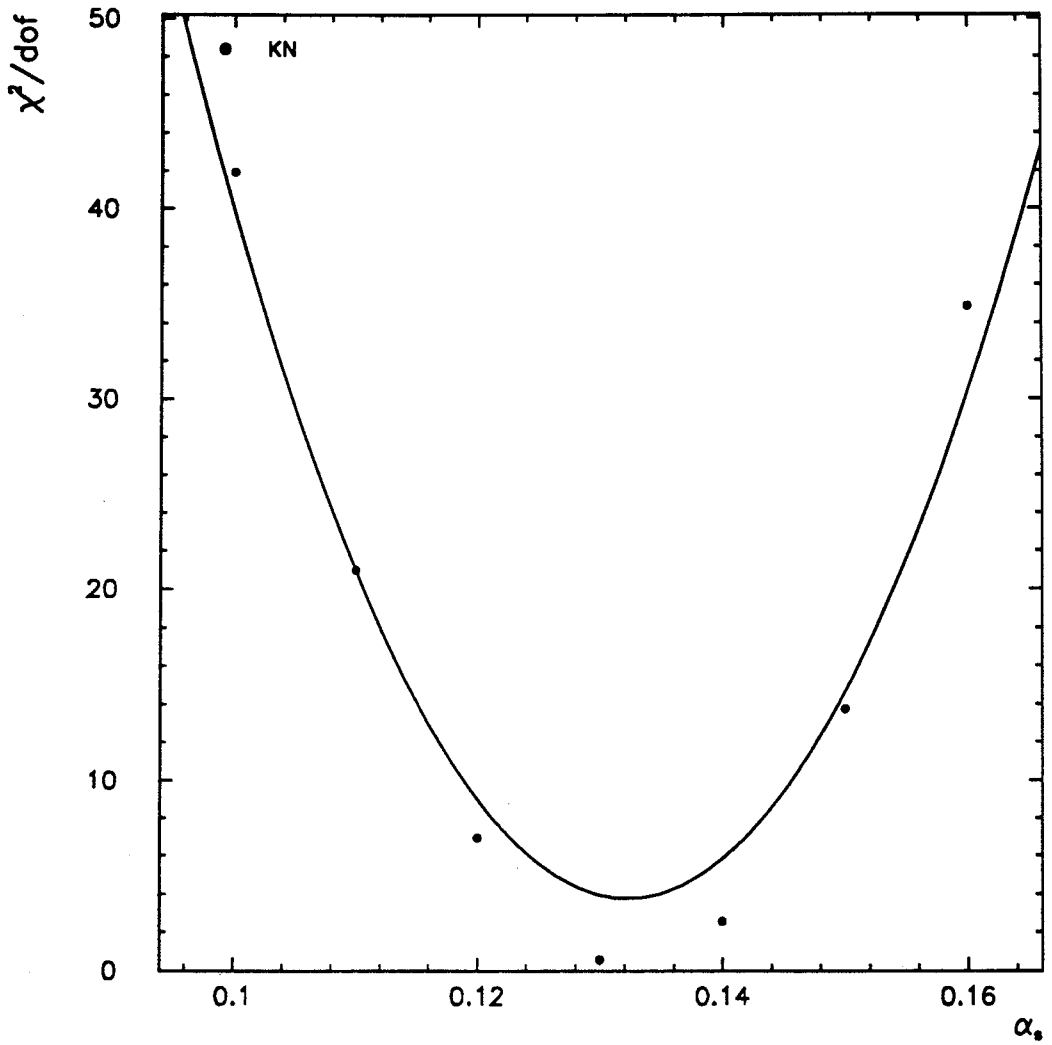

Figure 4.8: Parabolic fit to the data points $(\alpha_s, \chi^2/dof)$ obtained by fitting the KN analytical form for the $EEC(\chi)$ function to the corrected data.

4.3 α_s from the $EEC(\chi)$ function of particle clusters.

It has been mentioned in Section 4.2 that the theoretical prescriptions for calculating the $EEC(\chi)$ function are based on an analysis of the parton system. Due to the changes brought about by the fragmentation process, a difficulty arises when the predictions from these models are compared with data observed at the hadron level.

Although a Monte Carlo simulation can estimate the effect of the fragmentation process on the $EEC(\chi)$ and can allow a correction to be made for it, it would be helpful if some fragmentation-independent technique of comparing theory and experiment were available to provide a cross-check.

In this section are described the results of an analysis of the ALEPH hadronic data by comparing the $EEC(\chi)$ function of *particle clusters* with that of *partons* produced by an $\mathcal{O}(\alpha_s^2)$, matrix-element Monte Carlo generator.

4.3.1 Theoretical considerations.

A decay of the Z^o to a $q\bar{q}$ pair leads invariably to the production of hadron jets. It is asserted that the particles in the jets come from the fragmentation of quarks. If a gluon is produced which is sufficiently energetic to come off at a large angle from the parent quark, then it too should give rise to a distinct hadron jet. Naively then, it can be expected that the jets which are observed in the detector correspond to the most energetic partons prior to fragmentation.

The JETSET 7.3 Monte Carlo event generator is capable of calculating the cross-section for hard gluon emission to $\mathcal{O}(\alpha_s^2)$ using the matrix element formula of ERT [38]. In this formula, the gluon emission cross-section is calculated as a function of the transverse momentum of the gluon with respect to the parent quark direction and of the gluon energy. One problem with this is that for very low values of P_t or energy, the cross-section becomes large. To cope with such singularities in the collinear and infra-red limit, an artificial 'cut-off' in energy is employed in the Monte Carlo below which the emission of soft gluons is suppressed. Thus this Monte Carlo is able to generate events containing 2,3 or 4 hard partons in the initial state.

If the partons are assumed to correlate with jets, then the kinematical properties of the jets should reflect the underlying parton system properties in a way which is fairly independent of the fragmentation process.

The obvious difficulty with this approach is that of classifying the jets. A number of algorithms (commonly known as 'jet-finders') are available which can recognise tracks which are clustered together and combine them into a single jet. In this analysis two such algorithms were used, namely the scaled invariant mass algorithm (the so-called JADE algorithm) [39] and PTCLUS [40] which has recently been developed by ALEPH. They work as follows:

- **JADE.** For each pair of particles in the event, the invariant mass, Y_{ij} is calculated

$$Y_{ij} = \frac{1}{E_{vis}^2} \cdot 2E_iE_j(1 - \cos\theta_{ij}) \tag{4.11}$$

where E_{vis} is the total visible energy in the event, E_i and E_j are the energies of the two particles and θ_{ij} is the angle between them.

If the invariant mass of the pair is below a user-defined cut-off, Y_{lim}, then the two tracks are merged to form a cluster. This process is repeated until all particles have been grouped into clusters such that the invariant masses of all cluster pairs are greater than Y_{lim}.

Since this method starts with those pairs which have the lowest invariant mass, it tends to be sensitive to the presence of many low-momentum tracks and can create spurious jets by combining these. This is a particular disadvantage in high-multiplicity Z^o decays. However, the JADE algorithm has an established pedigree which makes it a useful benchmark against which to check alternative schemes.

- **PTCLUS.** This algorithm attempts to avoid the low-momentum sensitivity of the JADE approach by clustering the particles in two stages. In the first stage, the transverse momentum of each particle, relative to the most energetic track is determined. If the P_t is less than a pre-determined value, P_t^{lim} (in this work, 0.15 GeV/c) the two tracks are merged to form a cluster. If the P_t is greater than P_t^{lim} then the weaker track is used as the nucleus of a new cluster. This process is continued until the P_t of all clusters relative to each other is greater than P_t^{lim}.

  In the next stage those 'proto-clusters' which have been formed are further condensed by the same invariant mass method described in the discussion of the JADE algorithm. In a final step, it is checked that each particle has been assigned to the cluster relative to which it has the lowest P_t. If not, it is reassigned and the cluster merging step is repeated.

It should be pointed out that there is no simple way to merge the 4-momenta of two particles into a single cluster. The most obvious approach in which the momentum vectors and energy are added (the E-scheme) is Lorentz-invariant but produces a massive cluster, the mass of which grows as more and more tracks are merged into it. This leads to kinematic difficulties if the cluster is to be interpreted as a massless parton. The E_0-scheme produces massless clusters but at the price of violating momentum conservation. Other schemes sacrifice energy conservation for massless clusters or re-scale the 4-momentum to recover invariance. In this analysis the E_0-scheme, as defined in Equation 4.12,

was used. The effect of using the other schemes has been studied in [41] and found to contribute only slightly to the systematic error, with the E_0-scheme contributing least.

$$E_{ij} = E_i + E_j \qquad \vec{p}_{ij} = \frac{E_{ij}}{|\vec{p}_i + \vec{p}_j|} \cdot (\vec{p}_i + \vec{p}_j) \tag{4.12}$$

PTCLUS is not very sensitive to its internal parameter, P_t^{lim}, since this is used only to form the proto-clusters. The main user control in both JADE and PTCLUS is exercised through the resolution parameter, Y_{lim}, and the final number of jets found depends on its value. For this reason, the analysis was carried out using a range of values of Y_{lim} so that the variation of the result with Y_{lim} could be determined.

4.3.2 Experimental procedure.

The number of jets found in an event depends on the value of Y_{lim} which has been used in the jet finder. The variation of the proportion of two- and three-jet events as a function of Y_{lim} is shown in Figure 4.9. It can be seen that at a high value of Y_{lim}, most clusters are merged and the majority of events are classed as two-jet. On the other hand, if Y_{lim} is reduced sufficiently, the three-jet rate dominates. At still lower values of Y_{lim}, the three-jet rate declines and is superseded by four-jet events. At very low values of Y_{lim} however, the jet-finder becomes sensitive to the internal structure of a jet which may be due to fragmentation. At such low Y_{lim} fragmentation effects become important and the underlying parton structure of the event becomes obscure.

There is no 'best' value of Y_{lim}. Varying it simply changes the sensitivity of the jet finder to gluon emission. Since in this work the data were compared with matrix element calculations in $\mathcal{O}(\alpha_s^2)$, it was required only that the two-, three- and four-jet rates be considered. Thus Y_{lim} was varied in a region where those rates were large. The Y_{lim} range was 0.01 to 0.08. The higher values of Y_{lim} were included to test the stability of the final result over as wide a range of Y_{lim} as practicable. It should be noted that for most purposes, a Y_{lim} greater than about 0.03 leads to the jet-finder becoming very coarse and the majority of events being classified as two-jet. For this reason, smaller Y_{lim} are usually preferred and the final result quoted from this method is at a Y_{lim} of 0.02.

The analysis procedure was as follows:

1. 5 samples of 300,000 events each were generated by the JETSET 7.3 Monte Carlo using the $\mathcal{O}(\alpha_s^2)$ matrix element formula of ERT [38]. The input parameter in the matrix element calculation is $\Lambda_{\overline{ms}}$. However, the $EEC(\chi)$ function is (to first order) linear in α_s which, as will be recalled from Equation 3.11, varies logarithmically with $\Lambda_{\overline{ms}}$. Therefore the different

values of $\Lambda_{\overline{ms}}$ used in the different Monte Carlo samples were chosen to correspond with a linear change in $\log \Lambda_{\overline{ms}}$. The values of $\log \Lambda_{\overline{ms}}$ and the corresponding values of $\Lambda_{\overline{ms}}$ were

$\log \Lambda_{\overline{ms}}$	3.5	4.5	5.5	6.5	7.5
$\Lambda_{\overline{ms}}$ (MeV)	33	90	245	665	1808

2. For each sample, the $EEC(\chi)$ graph was calculated. The graphs corresponding to the samples at 3.5 and 7.5 are shown in Figure 4.10 to display the range used in the Monte Carlo. The graph obtained from the data with Y_{lim}=0.025 also is shown for comparison.

3. Each event in the selected real data sample was analysed using both jet finders (PTCLUS and JADE) at six different values of Y_{lim} and the $EEC(\chi)$ graph for the resulting clusters was obtained. In this way, 12 graphs were obtained from the sample. Figure 4.11 shows the graphs obtained using the PTCLUS algorithm at three of the values of Y_{lim} used.

4. The data were corrected using the same technique as described in Section 4.2.1. In this case the correction was applied to Monte Carlo truth level. That is to say, a sample of 149,000 fully simulated events (i.e. having gone through detector simulation and event reconstruction) was compared with a similar sample of events consisting of charged particles in the final state which had been generated without initial-state radiation. This correction was intended to reduce the smearing effect of the finite detector resolution and photon radiation in the initial-state.

5. The systematic error in the clustered $EEC(\chi)$ was estimated by the same technique as in Section 4.2. That is, the uncorrected clustered $EEC(\chi)$ histogram from the data was compared with that from the fully reconstructed simulation. After clustering, the residual systematic error was found to be large and of the order of 20%. This error is a compound of difference in jet-rates between the data and Monte Carlo and the difference in the $EEC(\chi)$ and was found to be the dominant source of error in this analysis.

   The theoretical error arose chiefly from the uncertainty in the QCD scale which is used in the $\mathcal{O}(\alpha_s^2)$ calculation of the gluon emission cross-section. To estimate this, a 'rough-fit' value for $\Lambda_{\overline{ms}}$ was obtained using only the statistical error. Two more Monte Carlo samples were generated using this value of $\Lambda_{\overline{ms}}$ but with the scales set at $M_z/2$ and at $2M_z$. The $EEC(\chi)$ graphs were obtained for these two samples and the difference between them was taken as the theoretical error.

The systematic and theoretical errors thus obtained were then combined in quadrature with the statistical error in the data as given by Equation 4.7. The error was calculated individually for each bin. However, the average error from each source over the range of bins fitted was found to be;

Statistical	2.1%
Systematic	21.4%
Theoretical	3.8%
Overall	21.8%

6. Each of the data graphs was compared with each of the Monte Carlo graphs and the χ^2/dof between the two was calculated according to Equation 4.5. The range over which the two histograms were compared was $-0.5 < \cos\chi < 0.5$, as in Section 4.2. This was to avoid the regions of the graph corresponding to 0^o and 180^o which are dominated by 2-jet events.

7. As in Section 4.2, the set of points $(\log\Lambda_{\overline{ms}}, \chi^2/dof)$ was fitted to a parabola and the minimum and error was determined from the resulting coefficients. The fit for the case of PTCLUS at a Y_{lim} of 0.0175 is shown in Figure 4.12.

4.3.3 Results.

The results obtained using this method are shown in Table 4.3. It is evident from Table 4.3 that the value of $\Lambda_{\overline{ms}}$ obtained depends on Y_{lim}. However, the variation of $\Lambda_{\overline{ms}}$ with Y_{lim} becomes weaker as Y_{lim} is increased. This effect is believed to be due to the influence of higher order corrections which become less important at high values of Y_{lim} [42].

Using the two-loop formula of Equation 3.14, the average values of $\Lambda_{\overline{ms}}$ can be used to obtain corresponding values of α_s which are shown in Table 4.4. The values obtained are consistent with those obtained in Section 4.2.

The ALEPH Collaboration has measured α_s from the $EEC(\chi)$ of particle clusters with Y_{lim}=0.02 [42]. This was done by comparing the data with an analytical formula rather than with Monte Carlo as in this work. For comparison, the results from this work were extrapolated to Y_{lim}=0.02;

$$\text{ALEPH} \quad \alpha_s(M_z^2) = 0.118 \pm 0.008$$

$$\text{This work} \quad \alpha_s(M_z^2) = 0.111 \, ^{+0.016}_{-0.013}$$

Table 4.3: Best-fit values of $\Lambda_{\overline{ms}}$ (MeV) obtained using PTCLUS and JADE jet-finders at different values of Y_{lim}.

Y_{lim}	$\Lambda_{\overline{ms}}$ (PTCLUS)	$\Lambda_{\overline{ms}}$ (JADE)	$\Lambda_{\overline{ms}}$ (Mean)
0.0100	$173\ ^{+284}_{-108}$	$178\ ^{+310}_{-113}$	$176\ ^{+297}_{-110}$
0.0175	$127\ ^{+178}_{-74}$	$140\ ^{+208}_{-84}$	$133\ ^{+191}_{-79}$
0.0250	$112\ ^{+155}_{-65}$	$126\ ^{+185}_{-75}$	$119\ ^{+170}_{-70}$
0.0400	$107\ ^{+131}_{-59}$	$121\ ^{+172}_{-71}$	$113\ ^{+147}_{-65}$
0.0600	$101\ ^{+137}_{-58}$	$111\ ^{+162}_{-66}$	$106\ ^{+150}_{-62}$
0.0800	$94\ ^{+146}_{-57}$	$101\ ^{+152}_{-60}$	$98\ ^{+149}_{-58}$

Table 4.4: Values of $\alpha_s(M_z^2)$ at different Y_{lim} corresponding to the average values of $\Lambda_{\overline{ms}}$ found.

Y_{lim}	$\alpha_s(M_z^2)$ from Clustered $EEC(\chi)$.
0.0100	$0.116\ ^{+0.020}_{-0.015}$
0.0175	$0.111\ ^{+0.016}_{-0.013}$
0.0250	$0.109\ ^{+0.016}_{-0.012}$
0.0400	$0.109\ ^{+0.014}_{-0.012}$
0.0600	$0.108\ ^{+0.014}_{-0.012}$
0.0800	$0.107\ ^{+0.015}_{-0.012}$

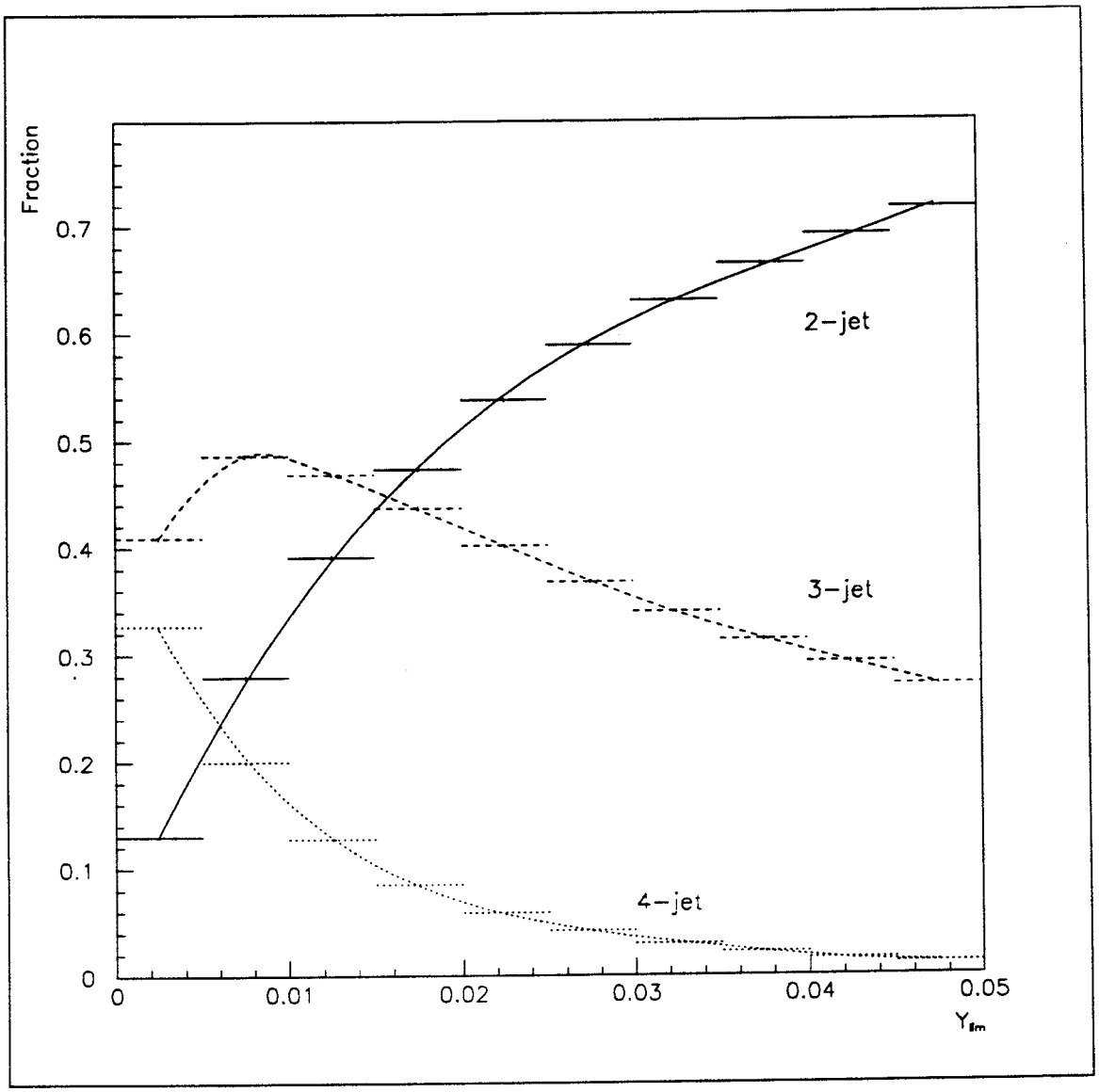

Figure 4.9: Proportions of events with a particular multiplicity of jets shown varying with Y_{lim}. All jet-rates were obtained using a fixed sample of some 186,000 events in the ALEPH detector.

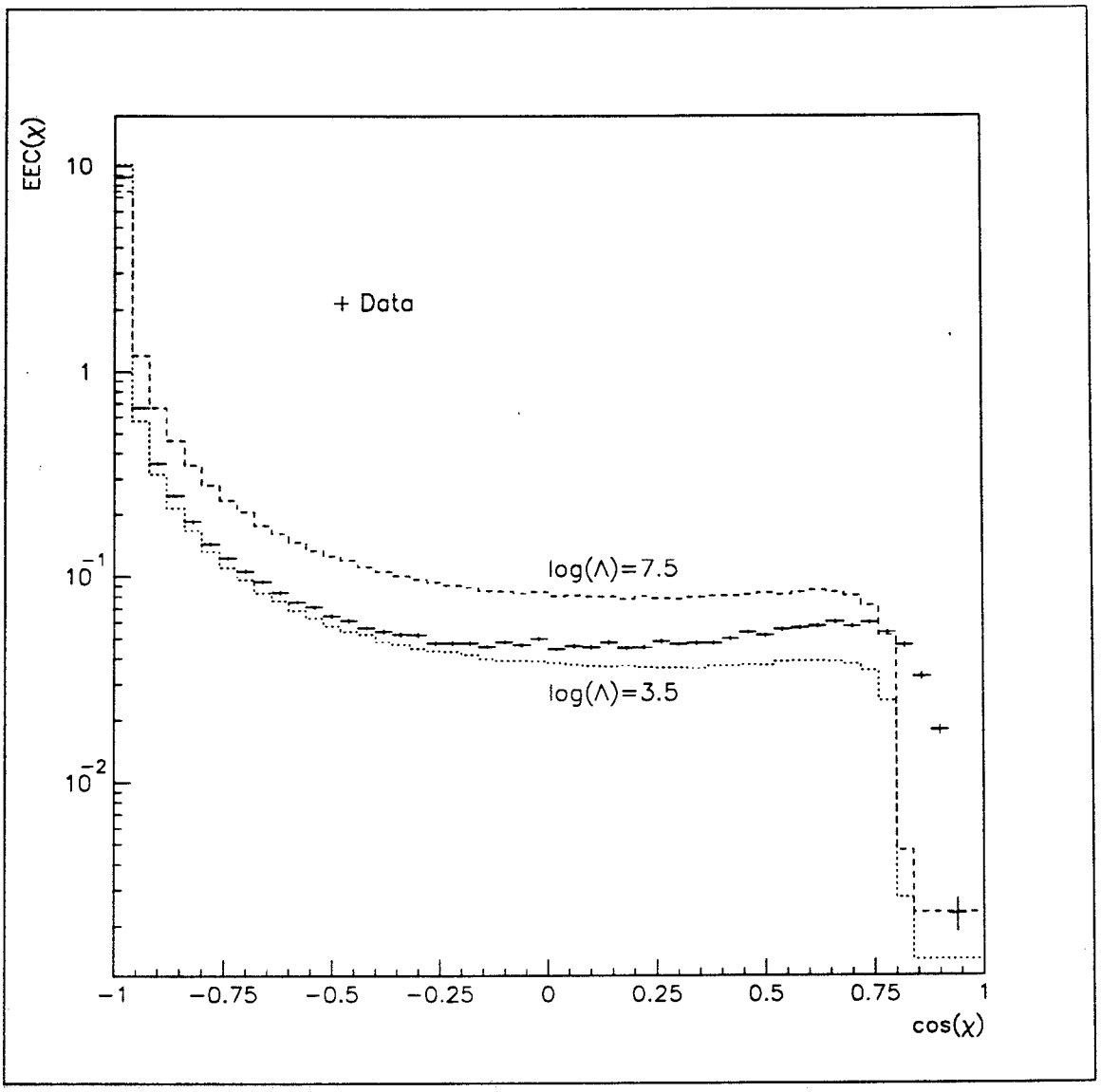

Figure 4.10: Range of clustered $EEC(\chi)$ graphs used to check the quality of the fit of the Monte Carlo samples to the data. All graphs were obtained using PTCLUS at Y_{lim}=0.025.

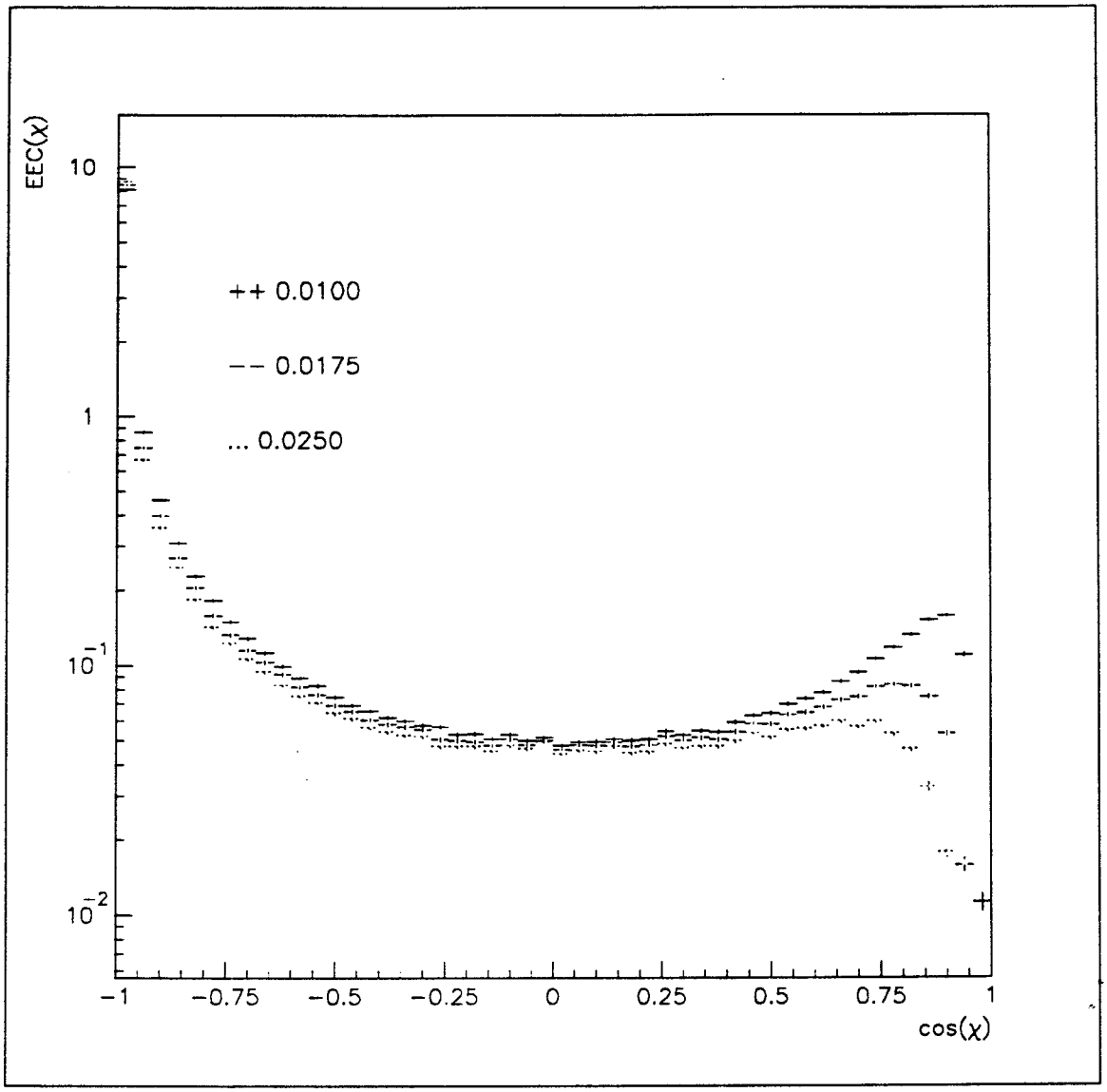

Figure 4.11: The $EEC(\chi)$ graph obtained for particle clusters at three different values of Y_{lim}.

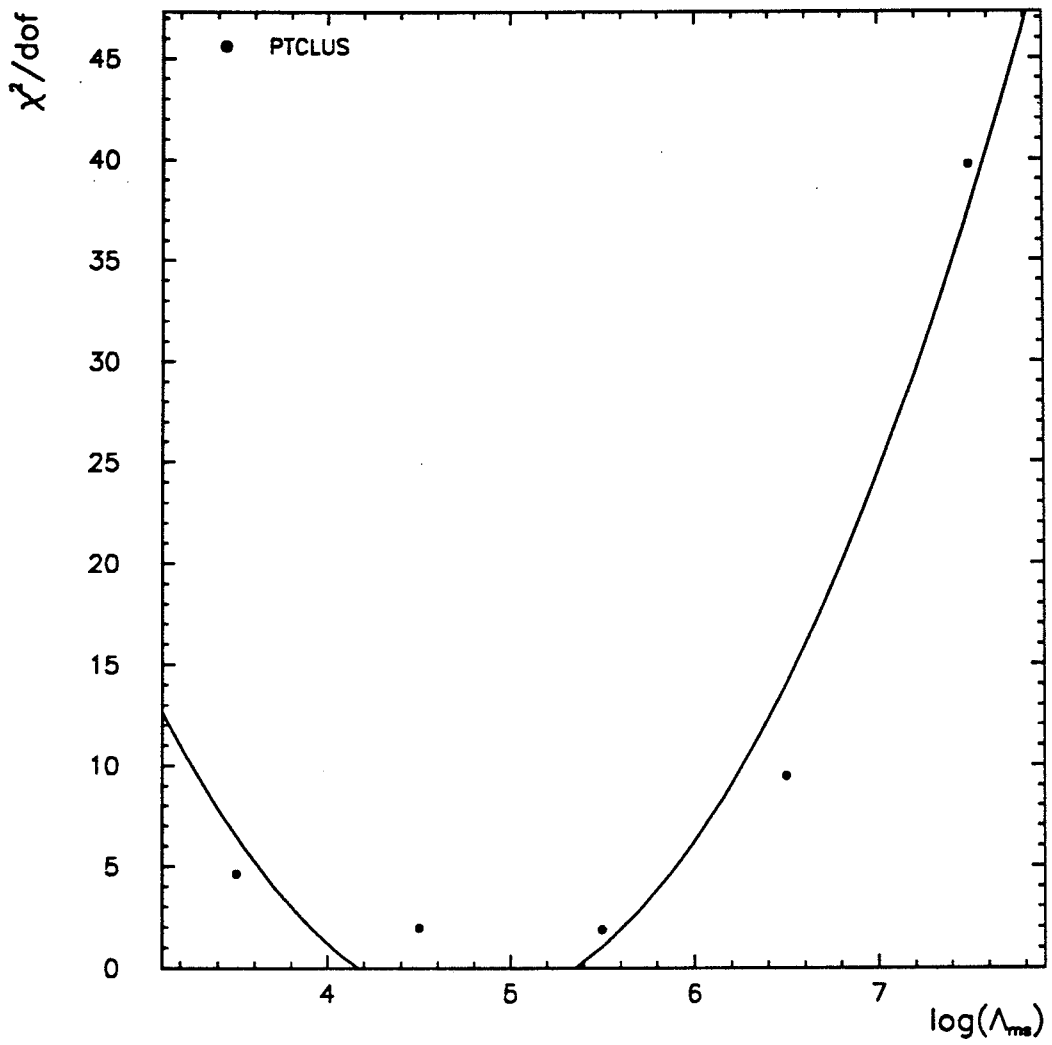

Figure 4.12: χ^2/dof between the data and Monte Carlo samples at different values of $\log \Lambda_{\overline{ms}}$ for the clustered $EEC(\chi)$ from PTCLUS at Y_{lim}=0.175.

4.4 Coherence and the $EEC(\chi)$ function.

If confinement is assumed to apply only to large ranges (> 1 fm) then the initial stages of the parton cascade from $q\bar{q}$ production may be calculated using perturbative QCD. If the non-perturbative kinematics of the hadronisation process do not upset the shower structure too much then the kinematics of the parton shower may be largely preserved in the resulting hadronic spectra. This is the concept of *Local Parton-Hadron Duality* (LPHD) [43]. It is thus to be hoped that many QCD phenomena will survive the hadronisation process and so will be observable in the final state. The $EEC(\chi)$ function has been suggested as a suitable metric to study in searching for manifestations of LPHD [29, p443-445].

4.4.1 Coherence and quark mass effects.

Gluon emission from quarks is believed to be a coherent process and so destructive interference between gluons may occur. The formation time for the gluon is given by [44]

$$t_{form} \simeq \frac{\lambda_\perp}{\theta_g} \tag{4.13}$$

where $\lambda_\perp$ is the transverse wavelength of the gluon and θ_g is the angle between quark and gluon.

In the time taken for the gluon to form, the original $q\bar{q}$ pair diverge and are separated by

$$\rho = \theta_q \cdot t_{form} \qquad \Rightarrow \quad \lambda_\perp \cdot \frac{\theta_q}{\theta_g} \tag{4.14}$$

For real gluon emission, ρ must be greater than the transverse wavelength, and so $\theta_q > \theta_g$. Thus as a quark radiates gluons in the parton shower, the opening angle is successively reduced and subsequent gluons come off at smaller and smaller angles. This is known as *angular ordering* and contributes to the resultant hadron jet being collimated.

In most perturbative calculations, the quarks are assumed to be massless. This is a reasonable approximation in the case of u, d, s or even c at LEP energies where the energy scale of the interaction is much greater than the mass of the quarks. For the b, however, the quark mass is an appreciable fraction of its energy. In this case, it is then worthwhile to extend the calculation to take account of the quark mass and the effect it has on the kinematics.

One such effect is that the phase-space for gluon emission is suppressed by the requirement that the opening angle between the quark and gluon be greater than a minimum, with $\cos\theta_{min} \simeq v_q$ where v_q is the velocity of the quark [45]. For a b of mass 4.5 GeV/c^2 and energy 45 GeV, this leads to $\theta_{min} = 6°$.

Taking the effect of angular ordering together with the suppression of gluon emission at low angles means that the angular region close to the quark will be depleted of gluon radiation and, at the parton level at least, the resulting jet will have a screened area in the jet core where the gluon density will be lower.

However, hadronisation has still to take place and so it is to be expected that the hadronisation and decay of the central b-quark will produce a number of final state particles close to the jet axis. This may tend to re-populate the depleted core of the jet and thus obscure the effect [46].

Nevertheless, observation of the 'screened-cone' would tend to support the concept of LPHD as well as providing evidence of coherence.

4.4.2 Experimental investigation.

Any effect which modifies the shape of a jet will also modify the $EEC(\chi)$ function. Consider a $b\bar{b}$-event where no hard gluons are emitted; two back-to-back jets with depleted cores will be produced. In the $EEC(\chi)$ function, contributions will appear in the 180^o region from inter-jet correlations and at the region below around 30^o from correlations within jets. However, there will tend to be a deficit of contributions in the very low angle region (corresponding to $< 6^o$) since most particles within a jet are at an angle to each other which is greater than this. Therefore the peak of the $EEC(\chi)$ function at low angles will now appear at $\chi \sim 6^o$ instead of 0^o.

The Monte Carlo event generator, HERWIG 4.1, incorporates angular ordering and screened-cone emission as its basis for heavy quark fragmentation [31]. To demonstrate the effect described above, two samples of 20,000 $q\bar{q}$ events were generated. One sample consisted only of $b\bar{b}$ events while the other consisted only of $d\bar{d}$ events. The $d\bar{d}$ sample was intended to represent hadronic events which were later compared to the b-enriched sample in the data. All other physical parameters in the Monte Carlo were the same for both samples.

The $EEC(\chi)$ function was studied for each sample. Since only the correlations *within* a jet were of interest in this study, only the low-angle correlations were calculated. In effect, therefore, the $EEC(\chi)$ graph was built up from *jets* rather than events. Also, binning was by degrees (rather than $\cos\chi$) and the final histogram was normalised to unity since only the shape of the histogram was of importance. The two graphs are shown in Figure 4.13. As a signal for the effect, the quantity S was defined as

$$S = \sum_{i=1}^{6}(c_i^d - c_i^b) + \sum_{i=7}^{45}(c_i^b - c_j^d) \tag{4.15}$$

where c_i^b is the ith bin entry in the $EEC(\chi)$ histogram of the $b\bar{b}$ sample and c_i^d that of the $d\bar{d}$ sample. For the graphs shown in Figure 4.13, $S = 0.313$.

To test for such an effect in the data, the following procedure was adopted:

1. A b-enriched event sample was selected based on a single-sided lepton tag. The event was required to contain at least one identified lepton with an absolute momentum of $\geq$ 5.0 GeV/c and a transverse momentum relative to the nearest jet axis of $\geq$ 0.5 GeV/c. Such a lepton was believed to originate from the prompt decay of a b-quark in, for example, the decay

$$\begin{array}{lcl} b & \rightarrow & c \quad W^- \\ & & \hookrightarrow \quad \mu^- \quad \nu_\mu \end{array}$$

   A sample consisting of 13,249 events was selected using this technique, with a purity of 73%, estimated from simulations [47].

2. Since the effect being investigated was expected to be present only in quark jets, gluon jets would act as a source of noise. For this reason, only two-jet events (as defined by PTCLUS with Y_{lim}=0.0175) were considered. This reduced the sample to 4,803 events.

   It was clear that the presence of a lepton with a high transverse momentum to its jet axis (as required by the b-event tagging) would lead to significant entries in bins which were several degrees away from zero. Such an effect would certainly bias the analysis and perhaps produce a false signal. Consequently, two $EEC(\chi)$ graphs were produced: one consisting of the correlations from the full sample of jets ('all jets') and another consisting only of correlations from jets which did *not* contain a tagged lepton ('no lepton'). The 'all jets' graph thus consisted of the correlations from 9,606 jets while 3,792 jets contributed to the 'no lepton' graph.

3. For comparison, two-jet events were selected from the full data sample using the same jet-finder and Y_{lim}. From 186,835 hadronic events, 65,887 two-jet events were selected. From this sample, only an 'all jets' $EEC(\chi)$ graph was composed.

   It should be noted that no attempt was made to exclude suspected b-events or tagged lepton jets from this sample. This was for the simple reason that the b-tagging routine can detect only semi-leptonic b-decay and so while the sample thus produced may be around 73% pure, the selection technique is only about 20% efficient. Thus, the majority of b-events remained in the data sample. Also, no attempt was made to correct either graph for the effects of detector acceptance or initial state radiation. Since both samples were data subsets, it was assumed that these effects would affect both the the b-sample and the full sample in the same way. Only the statistical error as defined in Equation 4.7 was considered.

   The 'no lepton' graph obtained from the b-enriched sample and the 'all jets' graph from the full data sample are shown and compared in Figure 4.15.

4. As has been stated, the b-enriched sample had been estimated to be some 73% pure. The main source of contamination was from $c\bar{c}$ events. Therefore, in order to simulate the b-enriched sample, a Monte Carlo sample consisting of 20,000 $b\bar{b}$ events and 7,300 $c\bar{c}$ events was produced. Two-jet events were selected from it to give a sample of 11,337 events. As before, an 'all jets' and a 'no lepton' $EEC(\chi)$ graph was composed for this sample.

   A second Monte Carlo sample of 80,000 mixed-quark events (u, d, s, c or b) was produced which yielded 33,404 two-jet events. This sample thus became the Monte Carlo representation of the full hadronic data sample and an $EEC(\chi)$ graph for 'all jets' was composed.

   The 'all jets' graph from the mixed-quark sample and the 'no lepton' graph from the $b\bar{b}$-rich sample are shown in Figure 4.14. These graphs yielded a value of $S = 0.191$ from the Monte Carlo simulation.

4.4.3 Results.

The following results were obtained as measurements of the screened-cone effect visibility parameter, S.

- Signal from Monte Carlo comparison of a pure $b\bar{b}$ sample with a pure $d\bar{d}$ sample (see Figure 4.13).

$$S_{MC} = 0.313.$$

- Signal from Monte Carlo comparison of a sample consisting of 75% $b\bar{b}$ and 25% $c\bar{c}$ with a mixed-quark sample (see Figure 4.14).

$$S_{MC} = 0.191.$$

- Observed signal in data. A comparison of the $EEC(\chi)$ graph from jets in the b-enriched sample but without a tagged lepton with the $EEC(\chi)$ graph from all two-jets events (see Figure 4.15).

$$S_{data} = 0.156 \pm 0.004_{stat}$$

From the Monte Carlo study, it can be seen that the strength of the signal is reduced to about 60% when hypothetical pure samples ($b\bar{b}$ versus $d\bar{d}$) are replaced by more realistic samples ($b\bar{b}$ contaminated with $c\bar{c}$ versus mixed-quark).

The corresponding signal observed in the data is at a level of about 80% of the prediction. Note that no attempt has been made in this analysis to *quantify* the systematic error. However, the analysis did seek to reduce the effects of the systematics by considering only those jets in suspected $b\bar{b}$ events which did not have a high-P_t lepton. Systematic effects in the detector should

not be important since the comparison is between subsets of data and these effects should be the same for both[2]. The same argument can be applied to hadronisation. Any residual systematic effects must therefore be small and, while they might change the size of the observed signal, it is difficult to believe they could be responsible for it entirely.

In conclusion then, a signal consistent with the screened-cone effect in heavy-quark fragmentation has been observed at a level of around 80% of that predicted by Monte Carlo simulation.

[2]If b-quark jets do have a different topology from lighter quarks jets, it could be argued that the detector response would be different. However, given that any difference is very small (as evidenced by the difficulty with which $b\bar{b}$ events are identified) it should not be expected that the systematic effects would be very different.

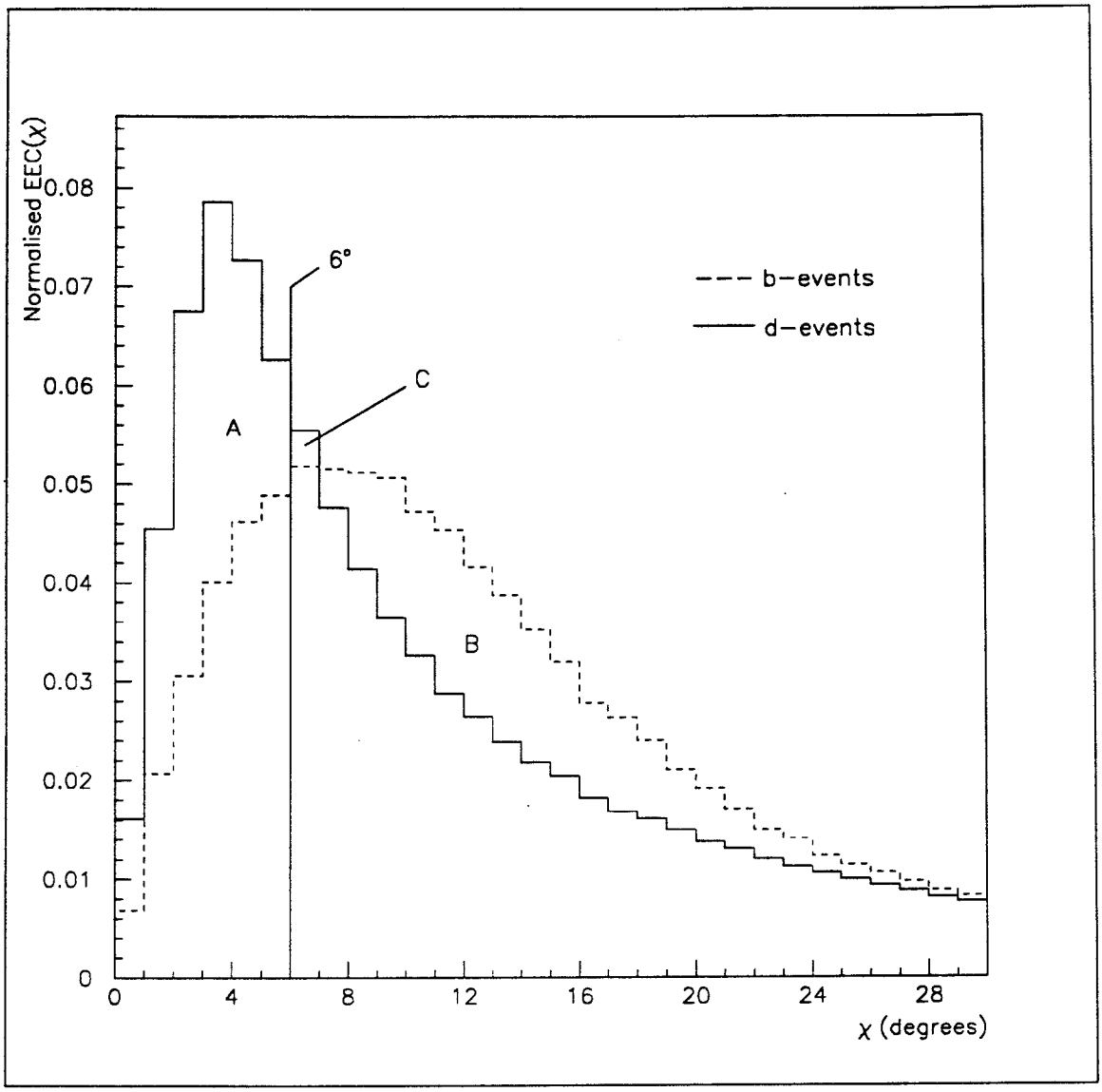

Figure 4.13: Comparison of $EEC(\chi)$ graphs for a pure $b\bar{b}$ and pure $d\bar{d}$ sample from Monte Carlo simulation. The signal for the screened-cone effect is given by the quantity S which is equivalent to the areas $A + B + C$. Because the graphs cross-over beyond the 6° marker, the area C is negative.

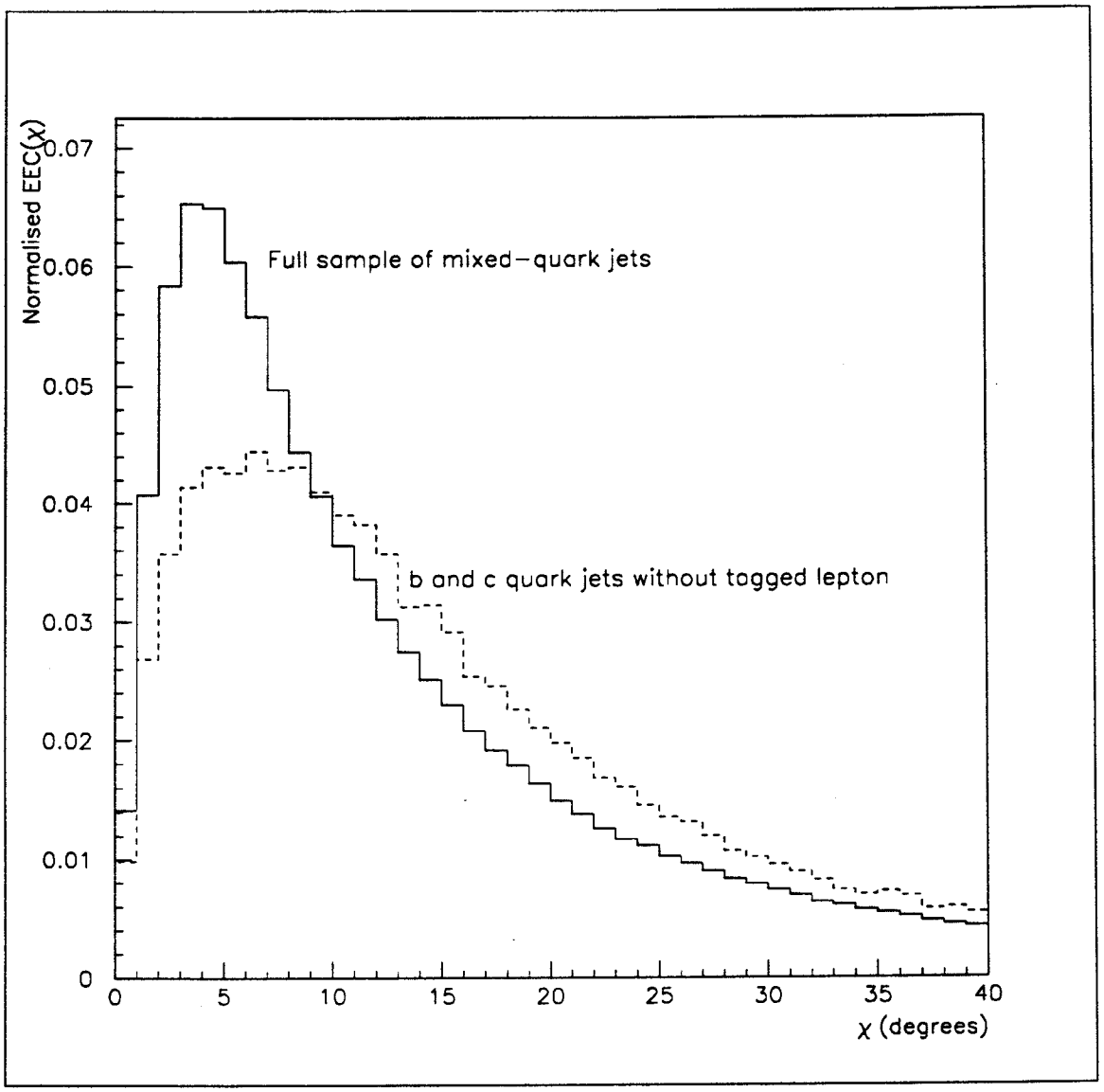

Figure 4.14: Realistic Monte-Carlo simulation of the screened-cone effect. The 'no lepton' graph from a sample consisting of $b\bar{b}$ and $c\bar{c}$ events in a 3:1 ratio is compared with the $EEC(\chi)$ graph from a sample of mixed-quark events.

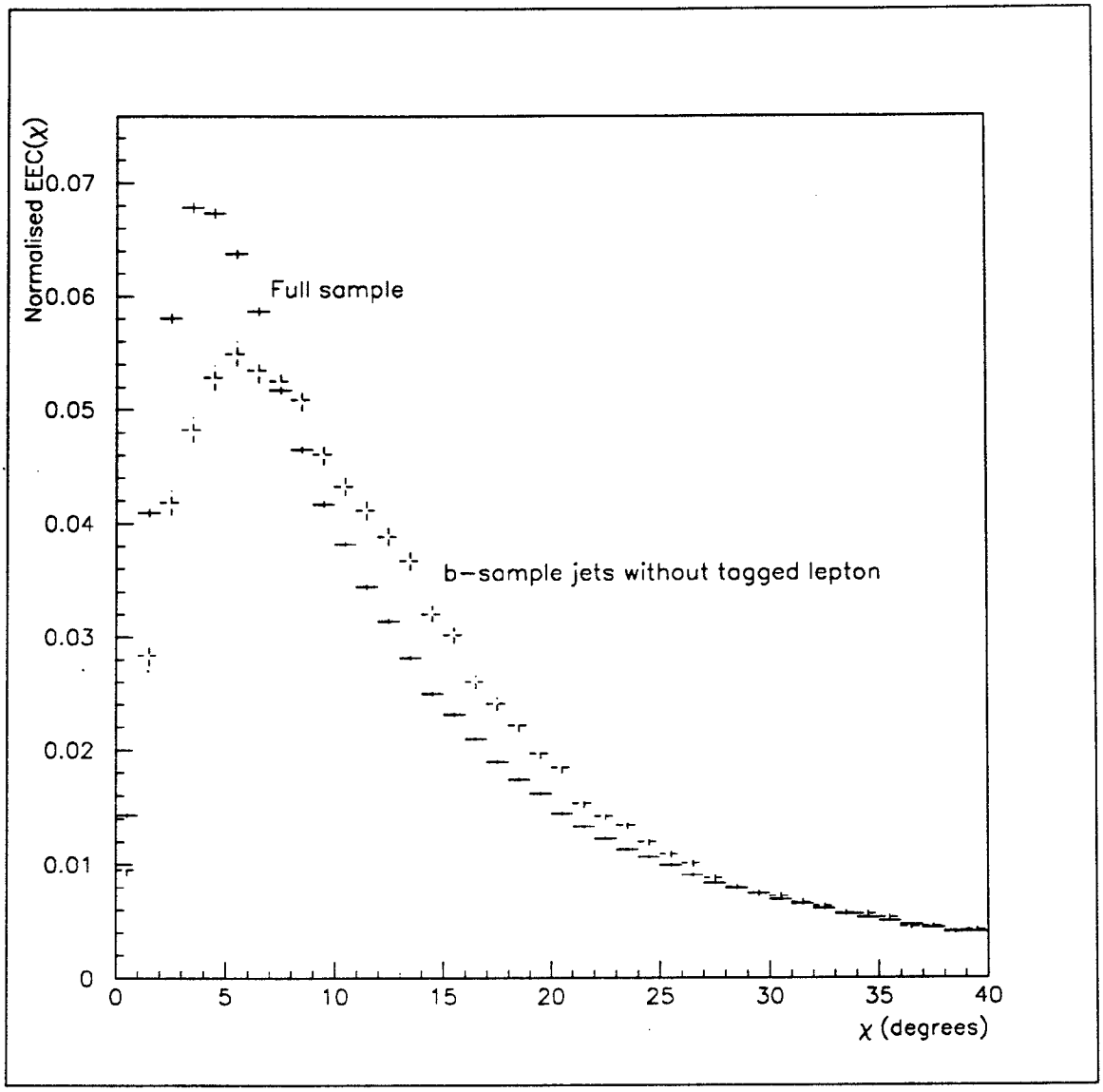

Figure 4.15: Screened-cone effect in the data. A b-enriched sample is compared with the full data sample. All jets containing tagged leptons have been removed from the b-enriched sample before calculating the $EEC(\chi)$ graphs.

4.5 The $EEC(\chi)$ function of quark and gluon jets.

One final application of the $EEC(\chi)$ function which has been considered in this work is that of discriminating between a sample of jets which have been produced by the fragmentation of quarks (quark jets) and a sample initiated by gluons (gluon jets). Distinguishing quark and gluon jets is an important task in QCD. For example, testing the non-Abelian nature of the QCD gauge through the observation of the triple gluon vertex and measuring α_s from azimuthal asymmetries could be carried out more precisely if gluon jets and quark jets could be differentiated.

4.5.1 Differences between quark and gluon jets.

One of the first differences to be anticipated between quark and gluon jets was suggested in 1969 by Feynman. He realised that the quark jet was likely to retain its parent quark flavour [49].

Another expected difference is one of multiplicity. Since the gluon carries a larger colour charge than the quark, it is expected to radiate soft *bremsstrahlung* gluons more liberally thus leading to more particles in the final state [50] and with a softer energy spectrum [51]. Also, since the gluon is a spin 1 boson, it has been suggested that the fragmentation products of a gluon would populate preferentially the phase-space in the plane of the event. This would be observable as *oblate* jets [51].

Presently, the most successful fragmentation model for describing hadronic decays of the Z^o is the string fragmentation model [53]. In this model, the primary $q\bar{q}$-pair are considered to be connected by a stretched colour flux tube or 'string'. Radiation of a gluon from one of the quarks is interpreted as a 'kink' developing in the string. As the partons diverge, the potential energy in the string increases until enough energy is present to allow the string to fragment into hadrons. One obvious distinction between quarks and gluons in this model is that a gluon is connected to *two* strings while a quark is connected to only one. The prediction that the inter-jet regions between a gluon and a quark will have an excess of particles compared to the region between two quarks is known as the *string effect*. Evidence in support of this has been found [52] and it is therefore to be expected that the P_t spectrum (with respect to the jet axis) of a gluon jet will be broader than that of a quark jet of the same energy.

Many approaches have been suggested to look for such effects with the eventual aim of developing an efficient gluon jet selection procedure. Since this analysis is concerned primarily with the performance of the $EEC(\chi)$ function in this regard, only one other technique, namely that of Fodor [54], is tested and compared with the $EEC(\chi)$ function.

Fodor has defined moments for each jet thus

$$M_{nm}(E_{jet}) = \sum \left(\frac{P_t}{E_{jet}} \right)^n \cdot \eta^m \tag{4.16}$$

where n and m are integers which define the moment, E_{jet} is the charged energy of the jet, the sum is over all the charged particles in the jet, P_t is the transverse momentum of a particle and η is its pseudorapidity with respect to the jet axis. The pseudorapidity is defined as

$$\eta = \frac{1}{2} \ln \left(\frac{1 + \cos\theta}{1 - \cos\theta} \right) \tag{4.17}$$

where θ is the angle between the particle track and the jet axis. This quantity is large for a track parallel to the jet axis and tends to zero as θ approaches a right-angle.

After some preliminary work, it was decided to study only the moment, M_{14}. A full study of the characteristics of these moments with regard to quark and gluon fragmentation was not possible in this work. It was anticipated that a quark jet, with a higher pseudorapidity than a gluon jet, would be assigned a higher value of M_{14} than a gluon jet since this quantity is heavily weighted by η.

With regard to the $EEC(\chi)$ function, it was expected that a gluon jet with a higher charged multiplicity and broader profile would lead to smaller (but more numerous) correlations in bins at larger angles than a quark jet of the same energy. This would lead to the $EEC(\chi)$ graph for a sample of gluon jets having a broader, flatter peak and a slower decline towards the high angle region than such a graph from quark jets.

The $EEC(\chi)$ is a distribution which applies to samples rather than individual events or jets. Therefore, it cannot be used to discriminate on a jet by jet basis between gluons and quarks. However, it was hoped it could be used to test the quality of a sample of candidate gluon jets and perhaps enable the purity of the sample to be determined.

4.5.2 Experimental investigation.

In order to establish the sensitivity of M_{14} and the $EEC(\chi)$ to the parton origin of a jet, the metrics must be tested against samples of jets which have been identified as coming from a quark or a gluon by some other independent (and hopefully accurate) technique.

In the case of gluons, such a sample can be found by considering those events which had been identified as originating from $Z^o \rightarrow b\bar{b}$, as described in Section 4.4. The quark jets in these events were tagged by the presence of a high-P_t lepton, indicating the prompt decay of a b-quark. Unambiguous gluon jets were selected from this sample in the following way

- Three-jet events were selected using PTCLUS with Y_{lim}=0.015. This value of Y_{lim} was chosen to maximise the three-jet rate.
- From this subset, events were selected with exactly two tagged jets.
- The third jet was then assumed to be a gluon jet.

From the initial sample of 13,249 $b\bar{b}$ candidate events, 6,145 three-jet events were selected. It was required, as usual, that no jet axis was within 35° of the beam axis; this cut reduced the sample to 4,238 good three-jet events. Furthermore, it was required that each jet had at least two charged tracks, removing 179 events from the sample. The final cut, that there should be exactly two tagged jets, removed a further 3,924 events. Thus a sample of 135 gluon jet candidates was obtained.

As for obtaining a sample of quark jets, it was clear that any two-jet event, selected at low Y_{lim}, would consist of only quark jets. However, the metrics studied, particularly the $EEC(\chi)$, were very sensitive to energy and so in order to ensure that the analysis was not biased, candidate gluon and quark jets had to be compared *at the same energy.*

In decays of the Z^o at the pole, the energy present in charged tracks is about 55 GeV. Thus in a collinear, two-jet event, each jet has a charged energy of some 27.5 GeV. A gluon jet, which obviously is only found in a three-jet event, seldom has a charged energy above around 15 GeV. However, unambiguous low-energy quark jets are produced occasionally when one quark emits a hard photon prior to fragmentation. Provided that this photon does not convert before leaving the tracking detectors, no charged tracks are produced in its direction. The resulting event then consists of two quark jets with their axes distinctly acollinear. More importantly, the loss of energy to the photon means that the mean quark jet energy is reduced and a sample of quark jets is obtained which have energies comparable to those of the gluon jets from the $b\bar{b}$ sample.

Hadronic events with a hard photon are, of course, important from the point of view of electroweak studies and indeed these have been studied by the ALEPH collaboration. A data-set of 1,738 such events is available and this sample of events was used to provide the unambiguous quark jet sample. Events consisting of exactly two jets were selected and after applying the cuts noted above regarding the number of charged tracks and the jet axis angle, 503 events were obtained, leading to a sample of 1,006 jets.

4.5.3 Results.

Despite the above efforts to obtain a quark sample at a similar energy to the gluon sample, large differences in the mean charged energy, charged multiplicity, P_t and pseudorapidity between the two samples were found. To enhance

the yield of low-energy quark jets, each of the above quantities was calculated separately for the two quark jets in each sample and sorted as 'higher energy jet' (jet 1) and 'lower energy jet' (jet 2). The values obtained for each of these quantities are shown in Table 4.5.

Table 4.5: Values obtained for various kinematic quantities in quark and gluon jets from ALEPH data.

Quantity	Quark Jet 1	Quark Jet 2	Gluon Jet
Charged Energy (GeV)	30.4 ± 0.3	17.1 ± 0.4	7.1 ± 0.5
Charged Multiplicity	8.08 ± 0.13	6.94 ± 0.13	4.88 ± 0.21
P_t (MeV)	379 ± 4	380 ± 5	372 ± 11
Pseudorapidity	2.59 ± 0.02	2.24 ± 0.02	1.86 ± 0.03

In addition to the study of the ALEPH data described previously, two separate Monte Carlo studies were carried out. In one case, JETSET 7.3 which incorporates the Lund string hadronisation model was employed. In the other, HERWIG 4.1, the cluster hadronisation model was used. In both simulations, final state hadronic events including initial state radiation, hadronisation and decay were subjected to the same selection procedures as the data in order to obtain samples of quark and gluon jets. The yields differed slightly from those obtained from data since particle identities are available in a Monte Carlo simulation.

For the HERWIG study, 75,000 $b\bar{b}$-events were generated from which 1,192 gluon jets were obtained and 3,434 low-energy quark jets were obtained from an initial sample of 80,000 mixed quark events. For JETSET, 17,466 gluon jets were selected from 100,000 $b\bar{b}$-events and 4,610 quark jets were obtained from 100,000 mixed quark events. The very high yield of gluon jets in the case of JETSET (17%) is somewhat anomalous since the respective figures from HERWIG and the data are 1.6% and 1.1%. It would appear that high-P_t lepton production is overly copious in this model. Due to constraints of time, no investigation of this was possible. However, the results obtained from the JETSET gluon jet sample were found to correlate well with those from HERWIG.

For each sample, M_{14} was calculated for each jet and stored as a function of energy. The moment was then averaged in bins of 5 GeV. Figure 4.16 shows the variation of M_{14} with jet energy for quark and gluon jets from the two Monte Carlo simulations. Very little discrimination is apparent at low energies although the two graphs do begin to diverge as E increases. Unfortunately, the mean gluon jet energy is so low that the statistical error in the gluon graph becomes large before a clear trend can be observed. Figures 4.17 and 4.18 show

the variation of M_{14} with energy for the quark jets and for gluon jets respectively. Also shown are the predictions from JETSET and HERWIG. The data are represented reasonably well by either Monte Carlo, although the quark fragmentation does appear to be slightly harder at low energies than the simulations predict. Figure 4.19 shows a comparison of M_{14} versus energy for quark and gluon jets in the data. The graph for quark jets is systematically above that for gluon jets, indicating that the quark fragmentation is harder than that of the gluons.

To investigate the $EEC(\chi)$ function three intra-jet $EEC(\chi)$ graphs were composed depending on the energy of each jet. The energy ranges were; 0–10 GeV, 10–25 GeV and > 25 GeV. It was found that sufficient statistics from both quarks and gluons occurred only in the central range of 10–25 GeV. Figure 4.20 shows the $EEC(\chi)$ in this energy range for quark and gluon samples from JETSET and HERWIG. A systematic shift in the gluon graph towards higher values of χ is indicative of softer fragmentation in those jets. In Figure 4.21 the $EEC(\chi)$ graph for quarks and for gluons are compared with the Monte Carlo predictions. Notwithstanding the low statistics in the gluon sample, the predictions appear to fit the data reasonably well. In the case of the quark sample, however, a large discrepancy is evident. This is due to a substantial mismatch between the distributions of jet energy in the data and in the Monte Carlo. This is despite the use of a limited energy range. Preselection of Monte Carlo events to reflect the energy distribution in the data would correct this effect but would perhaps bias the analysis. In Figure 4.22, the $EEC(\chi)$ graphs from the quark and gluon jet samples in the data are shown. The statistics are poor, particularly in the gluon jet case, however there does appear to be a distinction between the two graphs with the gluon $EEC(\chi)$ tending to peak at a large angle and to fall off more slowly towards large χ. While this is consistent with softer fragmentation in the gluon jet sample, unfortunately, the energy distribution among the quark and gluon jets is not the same — even in the limited 10–25 GeV range. The quark jets in this range have a mean energy of around 20 GeV while the gluon jets have a mean energy of only 14 GeV. This is shown in Figure 4.23, which shows the jet energy distributions for quark and gluon jets in the 10—25 GeV range.

The $EEC(\chi)$ function is very sensitive to such energy differences and so in the absence of a detailed study of systematic effects, it cannot be claimed that the distinction observed is due to a difference in fragmentation between quarks and gluons.

This analysis has been essentially qualitative, intended as a preliminary investigation to explore the feasibility of using the $EEC(\chi)$ function to discriminate between samples of quark and gluon jets. Consequently, no attempt was made to define any particular quantity which might be calculated as a signature for the expected effect. By corollary, no effort was made to determine the extent

of the systematic error.

In conclusion, some evidence for softer fragmentation gluon jets was observed using the M_{14} moment. In the case of the $EEC(\chi)$ a consistent effect was observed but due to a significant mismatch between the mean energies of the quark and gluon jets and large statistical errors brought about by the low sample size, no definite claim could be made.

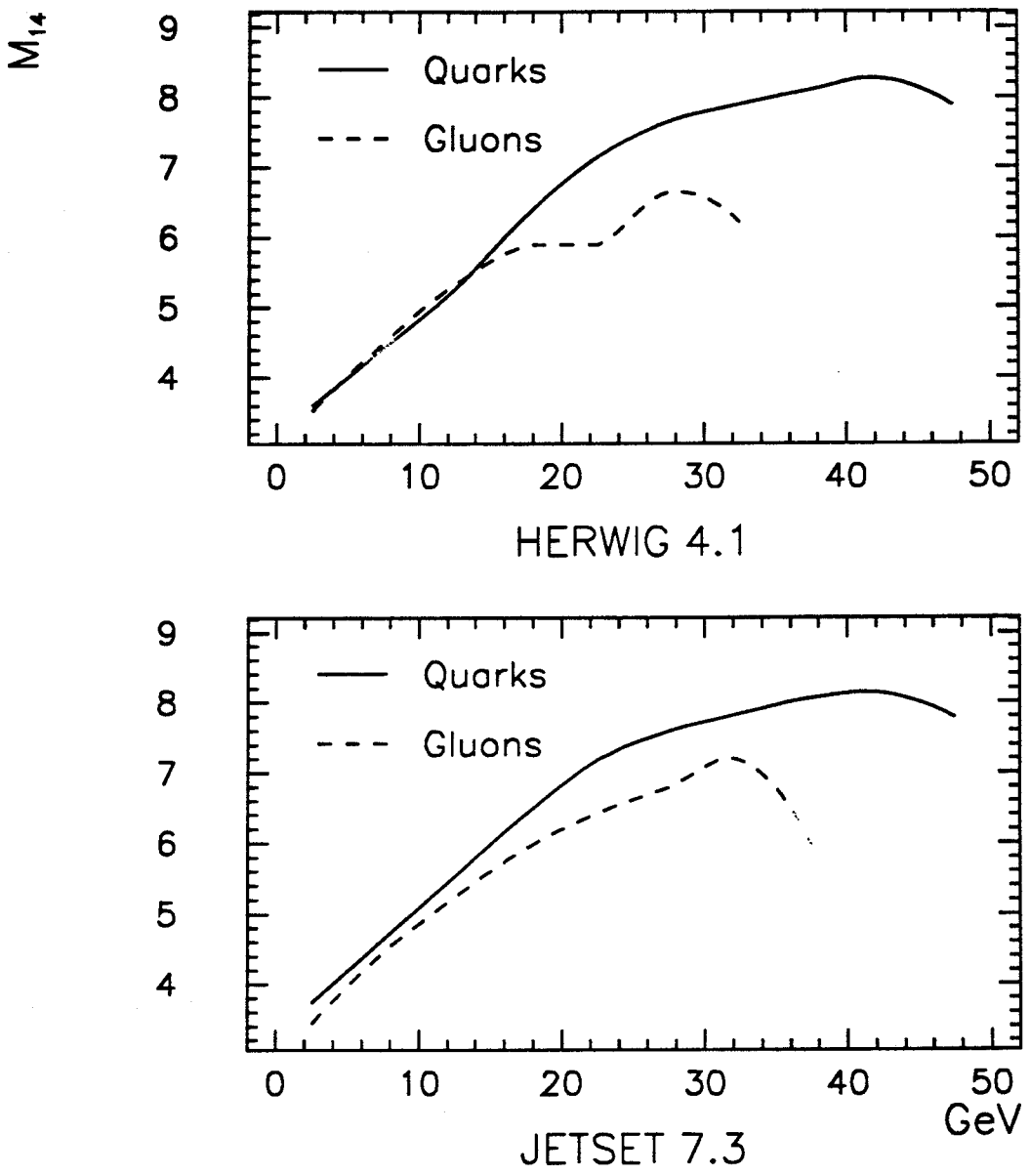

Figure 4.16: Moment M_{14} as a function of jet charged energy for quark and gluon jets in two Monte Carlo simulations. The fluctuations at higher energy are statistical and not significant.

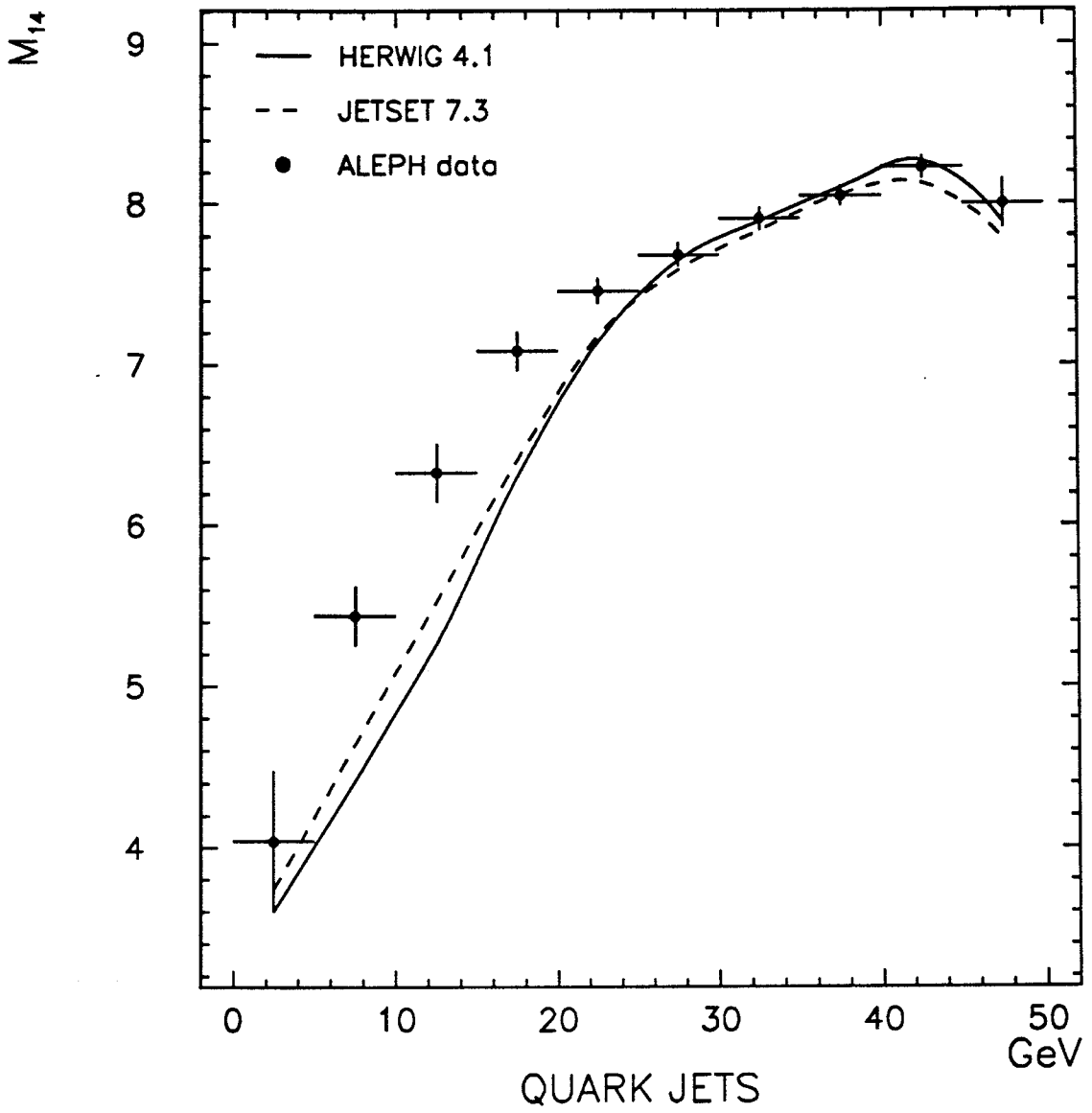

Figure 4.17: M_{14} vs. jet charged energy for quark jets. The ALEPH data are compared with JETSET 7.3 and HERWIG 4.1.

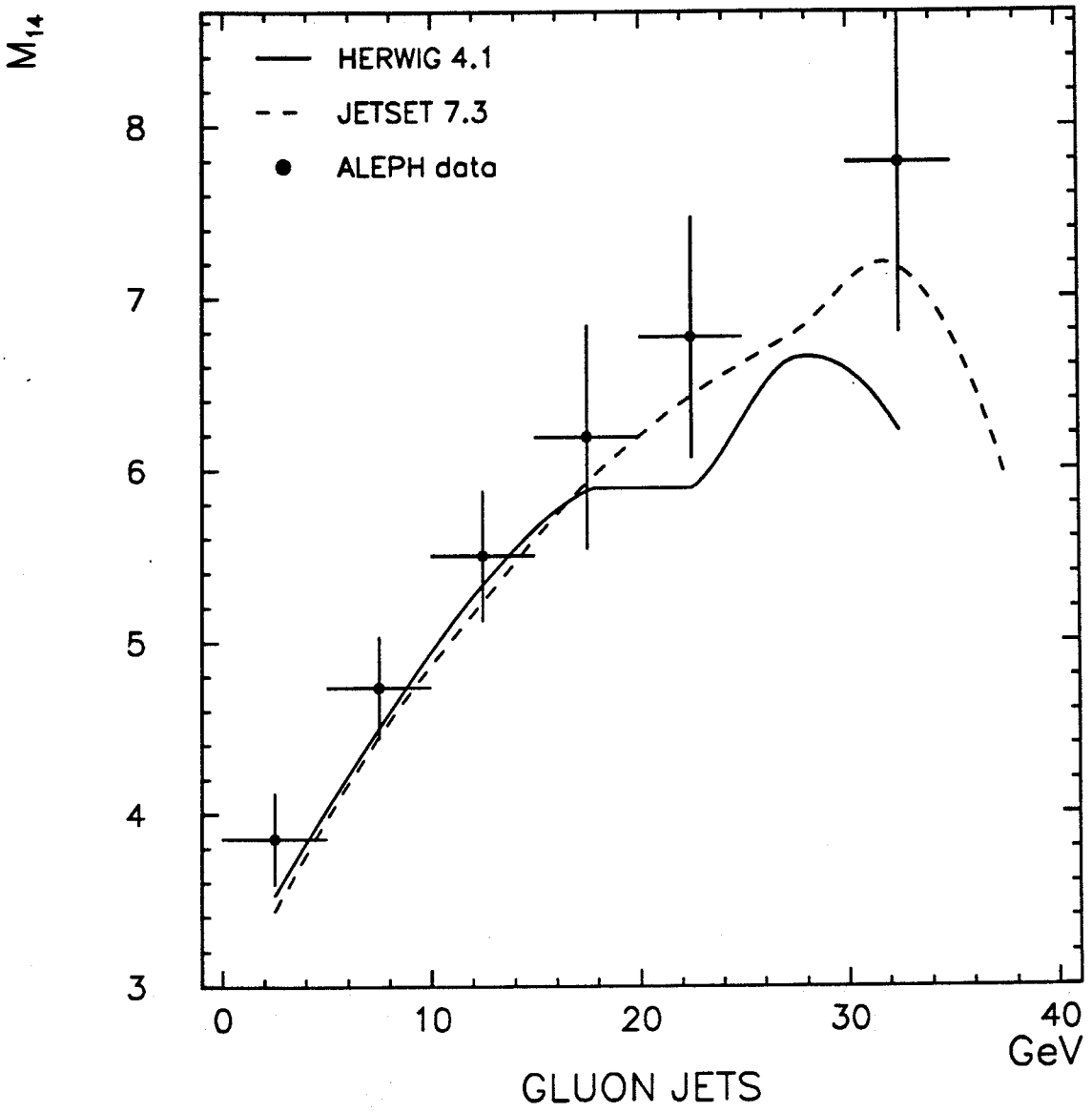

Figure 4.18: M_{14} vs. jet charged energy for gluon jets. The ALEPH data are compared with JETSET 7.3 and HERWIG 4.1.

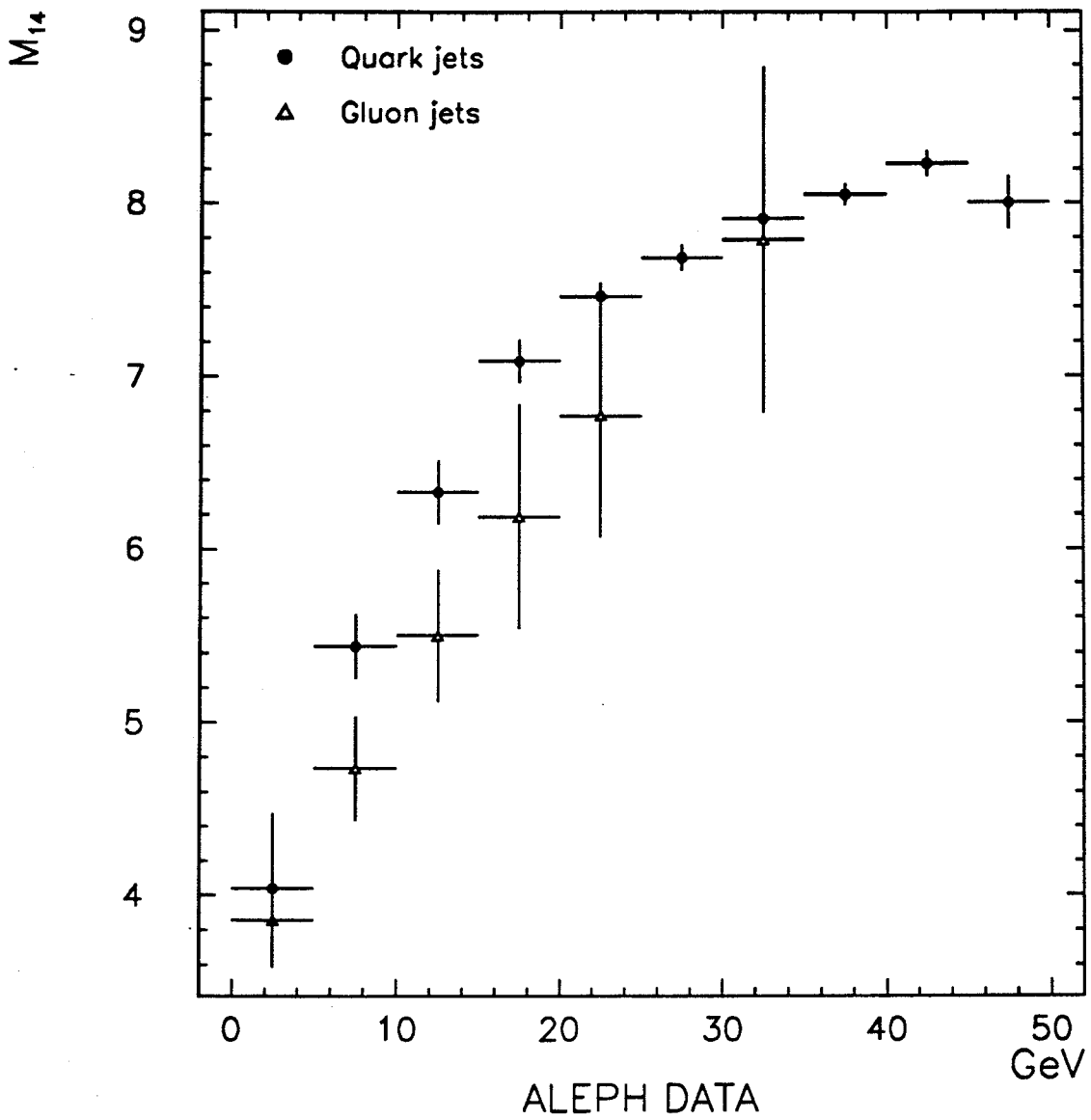

Figure 4.19: M_{14} for quark and gluon jets from ALEPH data compared. Statistical errors are large but some difference is evident.

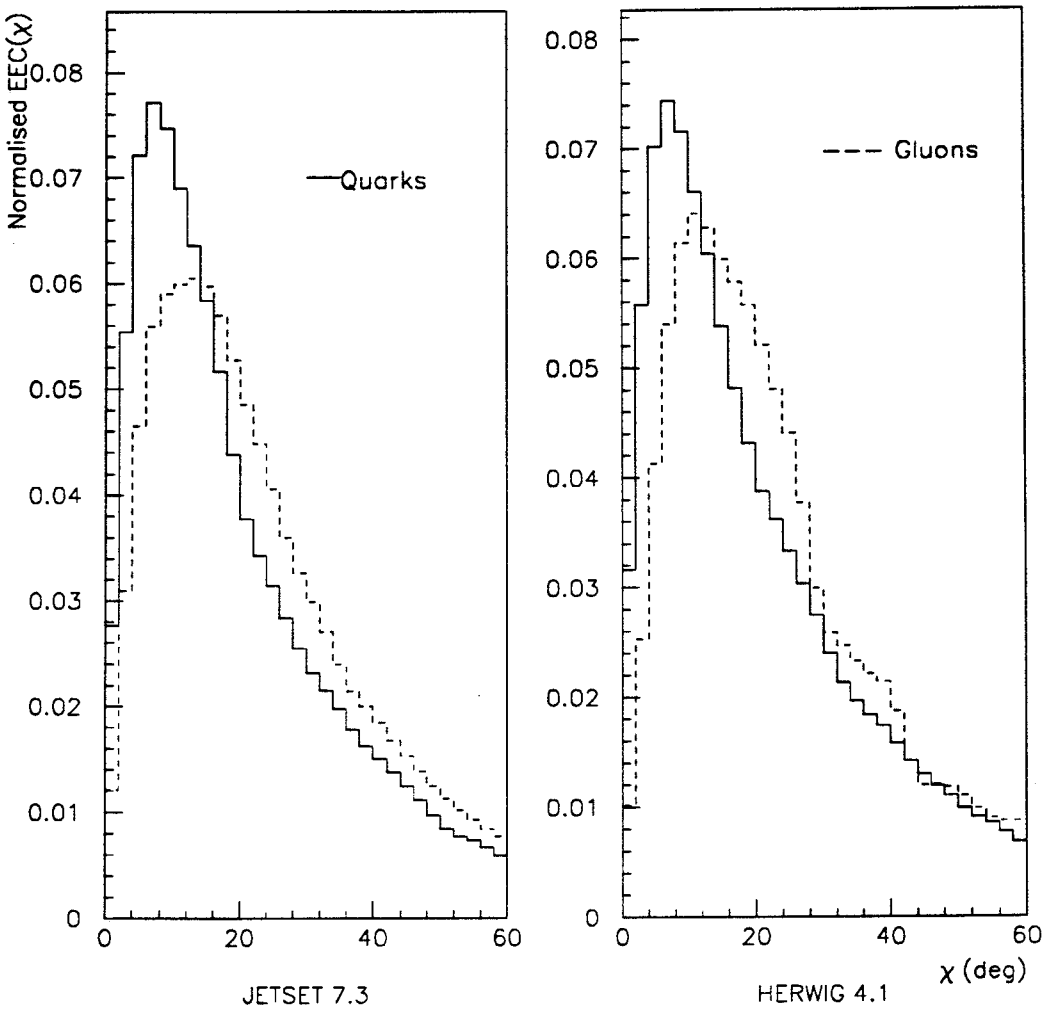

Figure 4.20: $EEC(\chi)$ for quark and gluon jets in two Monte Carlo simulations.

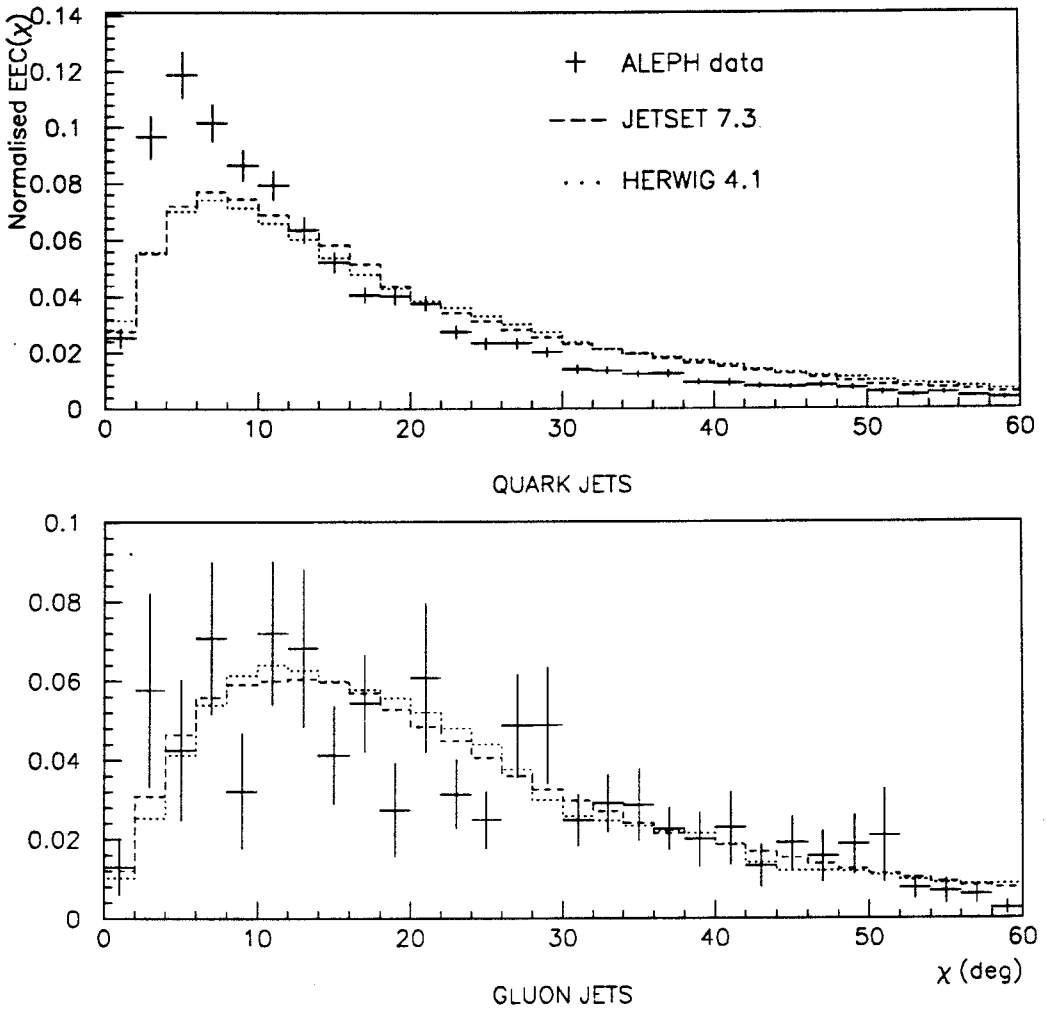

Figure 4.21: $EEC(\chi)$ for quark jets and gluon jets from ALEPH data compared with two Monte Carlo simulations.

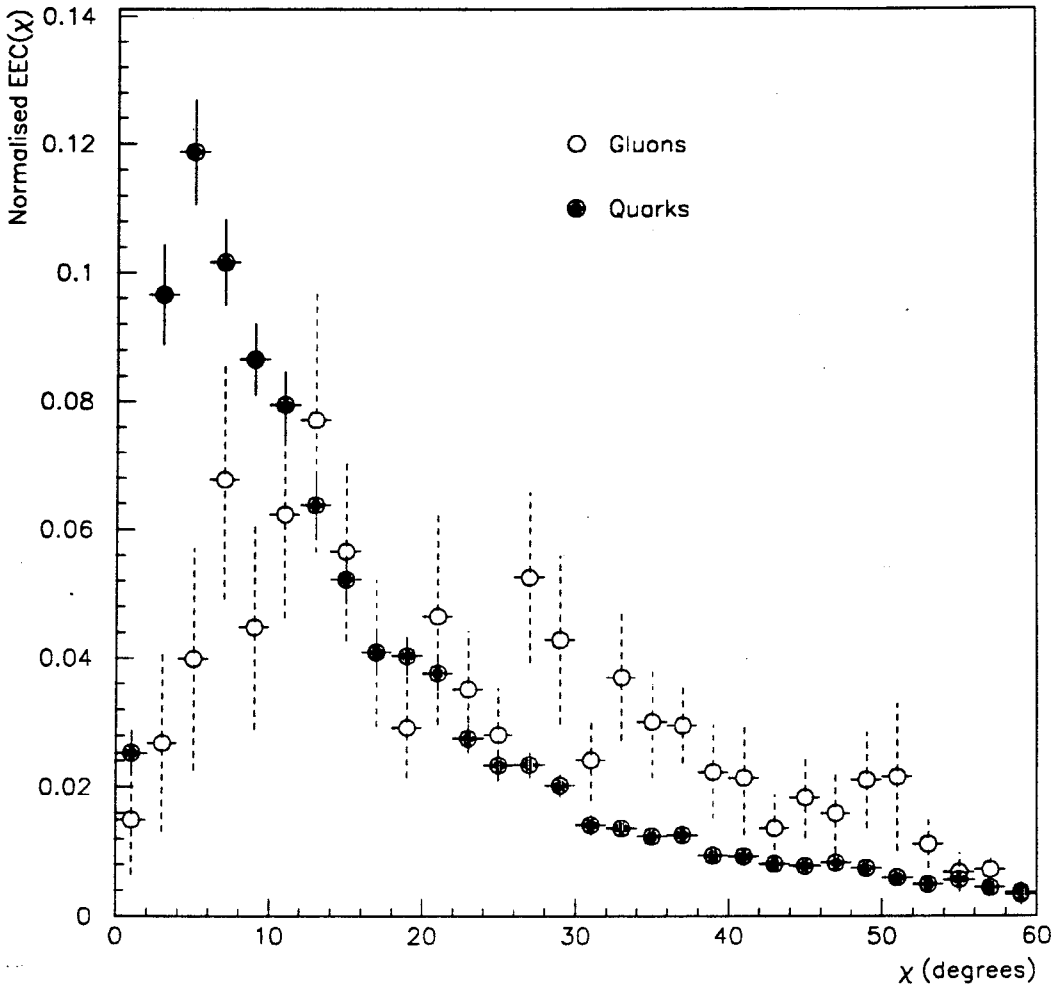

Figure 4.22: $EEC(\chi)$ for quark and gluon jets from ALEPH data. All jets used were in the energy range 10–25 GeV, although the gluon jets had a lower average energy than the quark jets.

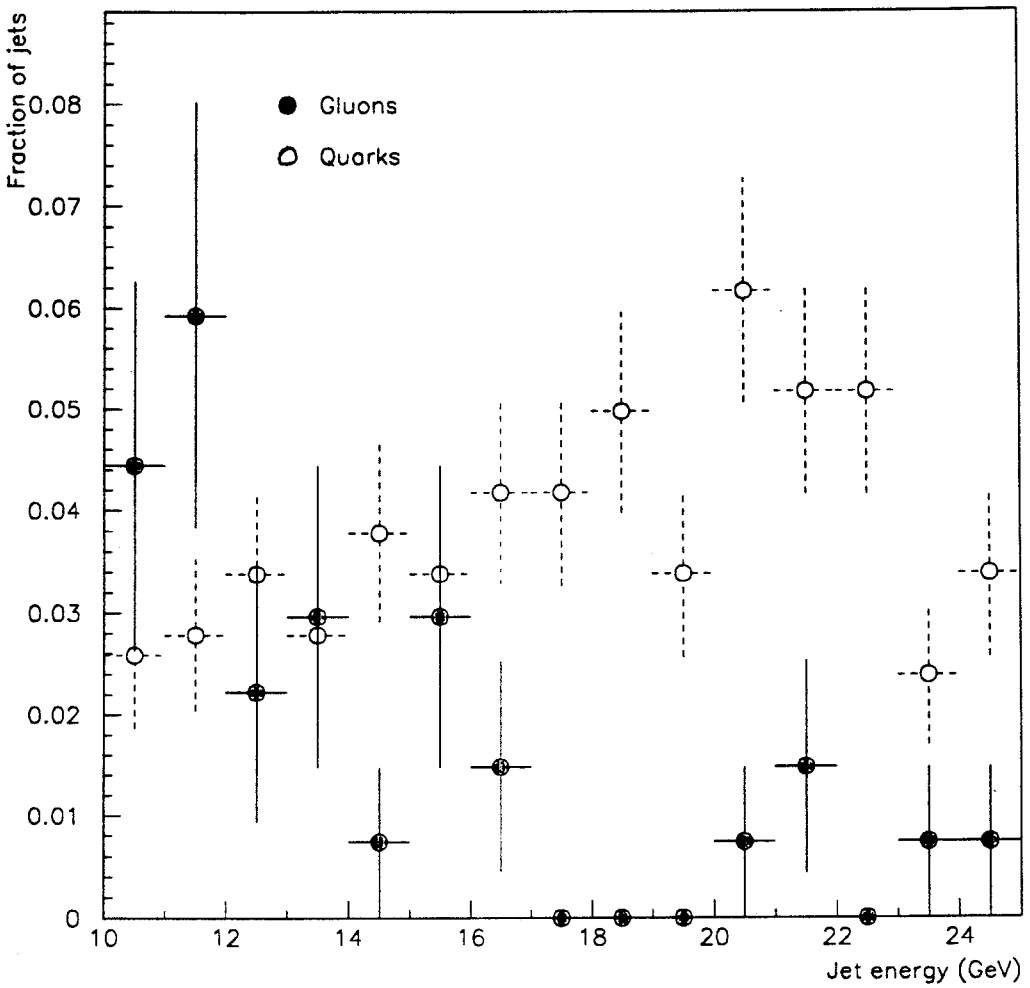

Figure 4.23: Jet charged energy distributions for quark and gluon jets in the range 10—25 GeV. Even in this limited range the quark jets have, on average, a higher energy than the gluon jets.

Chapter 5

Conclusions.

The work reported in this thesis has consisted of an analysis of the energy-energy correlations in hadronic events at the ALEPH detector at an energy of around 91.2 GeV. Energy-energy correlations have been used to determine the strong coupling constant, α_s, to demonstrate coherence effects in the fragmentation of heavy quarks and to search for differences between quark and gluon jets.

The results and method of analysis are presented and described in Chapter 4. In this Chapter, the results are summarised and compared with the results of other experimental groups working in this field. Comments on this analysis and how it compares with other work are given and recommendations for further study are presented.

5.1 Summary of results and comparison with other work.

5.1.1 α_s from $EEC(\chi)$ and $AEEC(\chi)$.

Hadronic events were selected from data collected by the ALEPH detector at energies around the Z^o-pole of 91.2 GeV. Some 186,000 events were selected from data collected during 1989 and 1990. The selection efficiency, estimated from Monte Carlo simulation, was 94.5%. Contamination from $\tau^+\tau^-$ events was estimated at 0.34%, at which level it was regarded as completely negligible. Contamination from $\gamma\gamma$ events was estimated to be nearly zero and so also negligible.

In one experiment, α_s was measured by comparing the $EEC(\chi)$ graph obtained for the data with an analytical form calculated to $\mathcal{O}(\alpha_s^2)$. Four separate theoretical prescriptions, employing different methods of summing the second-order contributions, were used for the analytical form. By measuring the χ^2/dof between the $EEC(\chi)$ in the data and the prediction and by minimising the

χ^2/dof with respect to α_s, a best-fit value of α_s was obtained. This was done for each of four prescriptions and also for the asymmetry in the $EEC(\chi)$.

The data were corrected for the effects of hadronisation, detector systematics and initial-state radiation by Monte Carlo simulation. Errors resulting from residual systematic effects (after correction), statistical fluctuation, energy uncertainty and theoretical uncertainty in the value of the QCD scale to be used in the $\mathcal{O}(\alpha_s^2)$ calculation of the prediction were estimated.

The results of the fit to the four predictions for the $EEC(\chi)$ and the $AEEC(\chi)$ were combined to give a single value of α_s for each metric. The results obtained from this work were compared with other recent results from LEP and are shown in Table 5.1.

Table 5.1: $\alpha_s(M_z^2)$ from $EEC(\chi)$ and $AEEC(\chi)$ from various experimental groups.

Experiment	$EEC(\chi)$	$AEEC(\chi)$
This work	$0.133 \pm 0.006^{+0.012}_{-0.009}$	$0.109 \pm 0.007^{+0.011}_{-0.007}$
L3 [55]	$0.121^{+0.012}_{-0.010}$	$0.115^{+0.009}_{-0.008}$
OPAL [56]	0.131 ± 0.009	0.117 ± 0.009
DELPHI [57]	$0.106^{+0.005}_{-0.004}$	—

The results obtained from this analysis are consistent with those obtained by other groups working in this field. Note that the other groups quoted used different techniques to extract a value of α_s from their determination of the $EEC(\chi)$. OPAL and L3 used essentially the same technique as was used in this work — that is fitting the $EEC(\chi)$ in the data to theoretical predictions. It is not, therefore, surprising that their results agree most closely with this analysis. DELPHI compared the $EEC(\chi)$ in the data with that obtained from Monte Carlo samples generated at different α_s. They used JETSET 7.2 with $\mathcal{O}(\alpha_s^2)$ matrix element calculations to predict the parton system followed by string fragmentation. This model has been shown [53] to reflect the characteristics of the data less well than, for example, parton shower models and so perhaps this explains their slightly discrepant result.

One interesting point is the tendency for the $AEEC(\chi)$ to return a lower value for α_s than the $EEC(\chi)$. To see how this might come about, consider

that what is being attempted is to vary a parameter (α_s) in a function until the function fits a set of points (the experimentally obtained $EEC(\chi)$ graph). The fact that the $AEEC(\chi)$ gives a lower answer than the $EEC(\chi)$ means that, as α_s is increased, the function attains the correct *shape* before it reaches the correct *height*. One possible explanation for this can be visualised by considering the $EEC(\chi)$ function for a sample of purely two-jet events. The $EEC(\chi)$ graph would have no central portion and there would be no asymmetry. This would correspond to a situation where α_s was close to zero. If 'typical' (ie. with one hard gluon jet at a reasonably large angle) three-jet events were added to the sample, then this would correspond to α_s increasing. The central portion of the $EEC(\chi)$ graph would rise and an asymmetry would develop. What appears to happen is that the asymmetry reaches the level seen in the data with fewer 'added' three-jet events (lower α_s) than the $EEC(\chi)$. The conclusion is that the $AEEC(\chi)$ is *more* sensitive to hard gluon radiation than the $EEC(\chi)$ and the difference between the values of α_s found for each is due to each probing a different region of phase-space.

5.1.2 α_s from clustered $EEC(\chi)$.

One of the problems associated with modelling the process $e^+e^- \rightarrow$ *hadrons* is that perturbative QCD calculations become invalid at low energy scales (close to Λ_{QCD}). This is the region where the coloured partons become confined to form colourless hadrons. Thus hadronisation can only be modelled by phenomenological methods and no theoretical understanding of the process exists at present. In addition, prior to hadronisation, there occur many higher order perturbative processes which by their multiplicity defy analysis.

One possible solution to this problem is to compare the structure of parton systems, as calculated to $\mathcal{O}(\alpha_s^2)$ with the structure of events consisting of jets of particles, where the jets have been classified in such a way as to produce comparable numbers of jets and partons.

This approach was attempted in Section 4.3, where the $EEC(\chi)$ function for clusters of particles was compared with samples of simulated parton events generated using the exact $\mathcal{O}(\alpha_s^2)$ matrix element formula implemented in JETSET 7.3. The data were fitted to the Monte Carlo and a value of $\Lambda_{\overline{ms}}$ was extracted. From this α_s was calculated using the two-loop expression of Equation 3.14. The value of α_s obtained was found to depend on Y_{lim}, the jet-finder resolution parameter. The result, quoted at Y_{lim}=0.02 is shown in Table 5.2 where it is compared with a result obtained from an ALEPH study of clustered $EEC(\chi)$ (but in which the data were compared with an analytical form for the clustered $EEC(\chi)$) and with values of α_s extracted by DELPHI and L3 from studies of jet rates. The result obtained in this study is consistent with other results which have similar systematics.

Table 5.2: $\alpha_s(M_z^2)$ from clustered $EEC(\chi)$ compared with similar experiments.

Experiment	$\alpha_s(M_z^2)$
This work	$0.111\ ^{+0.016}_{-0.013}$
ALEPH [42]	0.118 ± 0.008
DELPHI (jet rates) [58]	0.114 ± 0.013
L3 (jet rates) [59]	$0.115 \pm 0.005\ ^{+0.012}_{-0.010}$

5.1.3 Coherence effects in b-quark fragmentation.

The screened-cone effect, described in Section 4.4, was investigated using the $EEC(\chi)$ function. An effect was observed at the level of 80% of that expected from Monte Carlo simulation. This indicated that the suppression of collinear gluon radiation from heavy quarks, required by the interference of coherent gluons, led to a parton structure which was still visible in the final state hadronic system. Therefore, the hadronisation process did not entirely obscure the detailed structure of the parton system. The implication of this is that the *blanching* process, by which coloured quarks and gluons become colourless hadrons, is a local process in which each parton communicates with only its closest neighbours and there is no long-range communication across the pre-confinement 'femto-universe'.

This result is in agreement with a study carried out by the OPAL collaboration [48], which found that the inclusive momentum distribution of charged particles in hadronic Z^o decays could best be described by a model based on coherent gluon emission from quarks.

Systematic effects were not studied. The possibility of the $b\bar{b}$-event selection procedure producing a sample which was biased kinematically towards producing a screened cone effect in the $EEC(\chi)$ should be investigated more thoroughly than was possible here. However, the use only of jets *opposite* those tagged with high-P_t leptons should have limited this systematic.

5.1.4 Quark and gluon jets.

As described in Section 4.5, many models predict that the fragmentation of a gluon will be softer than that of a quark at the same energy. This should lead

to more particles in the final state, a wider P_t distribution across the jet and a lower mean rapidity. Such effects should also lead to differences in the low-angle region of the $EEC(\chi)$ function between quark and gluon jets. The moment, M_{14}, was investigated in addition to the $EEC(\chi)$.

Gluon jets were obtained from three-jet events in a sample of b-enriched events where both quark jets had been tagged with a high-P_t lepton. Quark jets were obtained from two-jet events containing a hard isolated photon. Loss of energy to the photon reduced the energy available to the quark jets thus bringing them closer in energy to the gluon jets.

Evidence for softer fragmentation in gluon jets was observed in the variation of M_{14} with energy. The form of the $EEC(\chi)$ graphs for quarks and gluons was also consistent with this effect, but due to a large difference in jet energy distribution between the quark and gluon jet samples and large statistical fluctuations, particularly in the gluon sample, it cannot be claimed that fragmentation differences are responsible.

The inclusive fractional momentum distributions of quark and gluon jets were studied by the TASSO collaboration [60]. They compared a sample of three-jet events at $\sqrt{S}$ = 35 GeV (gluon-enriched) with a sample of two-jet events at $\sqrt{S}$ = 22 GeV (quark-only) but found no significant difference in the distributions between the two samples. They recomended that higher energies and larger statistics would be required to observe any distinction.

More recently, the OPAL collaboration [52] has studied the angular distribution of energy and momentum in the plane of three-jet events. Gluon jets were identified by eliminating the highest energy jet (assumed to be a quark jet) and searching for high-P_t leptons in one of the lower energy jets. This technique is similar to that presented in this thesis. They found evidence of a softer particle energy spectrum in the core of the gluon jets and of a broader jet profile. In addition, they found that the data were best described by a model incorporating string hadronisation rather than one based on independent hadronisation.

The observations in this thesis appear to be in agreement with the OPAL result.

An increase in statistics would enable narrower bands of jet energy to be used in this analysis and so reduce the effect of the energy mismatch. A deeper understanding of the systematic effects would be required before any quantitative studies could be undertaken. In particular, the correlation between the untagged jet (assumed to be from a gluon) and the underlying gluon in three-jet $b\bar{b}$-events should be investigated by a Monte Carlo study.

Bibliography

[1] S. Myers and E. Picasso *The design, construction and commissioning of LEP* (to be published in *Contemporary Physics*) (1990).

[2] *The ALEPH Handbook* (ed. W.Blum) ALEPH note 89-77 (1989).

[3] D. Decamp et al, *Nucl. Inst. and Methods* A294 (1990) 121.

[4] W.B. Atwood et al, *CERN preprint* PPE/91-24 (1991).

[5] D. Decamp et al, *Phys. Lett. B* 231 (1989) 519.

[6] V. Blobel, *DESY report* R1-88-01 (1988).

[7] Sir I. Newton, *Philosophiae Naturalis Principia Mathematica* Streater (1687).

[8] P. Lorrain and D. Corson, *Electromagnetic Fields and Waves* Freeman (1970).

[9] P.A.M. Dirac, *The Principles of Quantum Mechanics,* Oxford University Press (1947).

[10] W. Pauli, *Handbuch der Physik* 24 (1933) 1233.

[11] E. Fermi, *Z. Physik* 88 (1934) 161.

[12] H. Yukawa, *Proc. Phys. Math. Soc. Japan* 17 (1935) 48.

[13] C.M. Lattes et al, *Nature* 159 (1947) 694.

[14] M. Gell-Mann and Y. Ne'eman, *The eightfold way* Benjamin (1964).

[15] V. Barnes et al, *Phys. Rev. Lett.* 12 (1964) 204.

[16] F. Halzen and A.D. Martin, *Quarks and Leptons* John Wiley and Sons (1984).

[17] J.E. Augustin et al, *Phys. Rev. Lett.* 33 (1974) 1406.

[18] S.W. Herb et al, *Phys. Rev. Lett.* 39 (1977) 252.

[19] C.D. Anderson, *American Journal of Physics* 29 (1961) 825.

[20] M.L. Perl et al, *Phys. Rev. Lett.* 35 (1975) 1489.

[21] G. Danby et al, *Phys. Rev. Lett.* 9 (1962) 36.

[22] S. Weinberg, *Rev. Mod. Phys.* 46 (1974) 255.

[23] F. Bergsma et al, *Phys. Lett. B* 147 (1984) 481.

[24] G. Arnison et al, *Phys. Lett. B* 122 (1983) 103.

[25] D. Decamp et al, *Z. Physik* C 48 (1990) 365.

[26] A. Blondel, *CERN preprint* EP/90-10 (1990).

[27] D.H. Perkins, *Introduction to High Energy Physics* Addison-Wesley (1986).

[28] J. Stirling, *Perturbative QCD: Proceedings of the CERN Summer School 1990*, CERN (1990).

[29] Z. Kunszt and P. Nason, *CERN* 89-08 Volume 1 (1989).

[30] T. Sjostrand, *Int. Journal of Mod. Phys.* A3 (1988) 751.

[31] G. Marchesini and B.R. Webber, *Nucl. Phys.* B310 (1988) 461.

[32] D. Decamp et al, *Phys. Lett. B* 255 (1991) 623.

[33] C. Basham, L. Brown, S. Ellis and S. Love, *Phys. Rev.* D17 (1978) 2298; *Phys. Rev. Lett.* 41 (1978) 1585; *Phys. Rev. D* 24 (1981) 2383.

[34] A. Ali and F. Barreiro, *Phys. Lett. B* 118 (1982) 155.

[35] D.G. Richards, W.J. Stirling and S.D. Ellis, *Phys. Lett. B* 119 (1982) 193.

[36] N.K. Falck and G. Kramer, *Z. Physik* C 42 (1989) 459.

[37] D.H. Menzel, *Fundamental formulas of Physics,* Dover (1960).

[38] R.K. Ellis, D.A. Ross and A.E. Terrano, *Nucl. Phys.* B178 (1981) 421.

[39] W. Bartel et al, *Z. Physik* C 33 (1986) 23.

[40] M.S. Scarr and I. ten Have, *ALEPH note* 89-150 (1990).

[41] F. Steeg, *ALEPH note* 91-84 (1991).

[42] D. Decamp et al, *Phys. Lett. B* 257 (1991) 479.

[43] Y.I. Asimov et al, *Z. Physik* C 27 (1985) 65.

[44] Y.L. Dokshitzer et al, *Rev. Mod. Phys.* 60 (1988) 373.

[45] B.R. Webber, *Cavendish preprint* HEP-88/6 (1988); Y.L. Dokshitzer et al, *Proceedings of Workshop on Jet studies at LEP and HERA*, Durham University DTP-91/04 (1990) C41.

[46] I.G. Knowles, private communication.

[47] D. Decamp et al, *Phys. Lett. B* 257 (1991) 492.

[48] G. Alexander et al, *Phys. Lett. B* 247 (1990) 617.

[49] R.P. Feynman, *Phys. Rev. Lett.* 23 (1969) 1415.

[50] J. Ellis and I. Karliner, *Nucl. Phys.* B148 (1979) 141.

[51] S.J Brodsky et al, *Phys. Lett. B* 79 (1978) 255.

[52] G. Alexander et al, *Phys. Lett. B* 265 (1991) 462.

[53] D. Decamp et al, *Phys. Lett. B* 234 (1990) 209.

[54] Z. Fodor, *Phys. Rev. D* 41 (1990) 1726.

[55] B. Adeva et al, *Phys. Lett. B* 257 (1990) 469.

[56] M.Z. Akrawy et al, *Phys. Lett. B* 252 (1990) 159.

[57] P. Abreu et al, *Phys. Lett. B* 252 (1990) 159.

[58] P. Abreu et al, *Phys. Lett. B* 247 (1990) 167.

[59] B. Adeva et al, *Phys. Lett. B* 248 (1990) 464.

[60] W. Braunschweig et al, *DESY preprint* 89-032 (1989).